

**Spinel Oxides and Heteroatom-doped  
Carbon Nano-composite as Bi-  
functional Oxygen Electrocatalyst for  
Rechargeable Zinc-Air Battery**

by

Moon Gyu Park

A thesis

presented to the University of Waterloo

in fulfillment of the

thesis requirement for the degree of

Master of Applied Science

in

Chemical Engineering

Waterloo, Ontario, Canada, 2015

© Moon Gyu Park 2015

## **Author's Declaration**

This thesis consists of material all of which I authored or co-authored: see Statement of Contributions included in the thesis. This is a true copy of the thesis, including any required final revisions, as accepted by my examiners.

I understand that my thesis may be made electronically available to the public.

## **Statement of Contributions**

Section 4 has been adapted from the following paper (reference number is 118) where I was the lead author.

## **Abstract**

With continued increase in energy demand for high energy-required devices such as portable electronics and electric vehicles, development of innovative energy conversion and storage systems has attracted tremendous attention. Even though lithium-ion battery technology is currently the most developed energy storage technology and employed for multiple applications, their insufficient energy density and critical problem in intrinsic chemistry limit their further development for fulfilling the ultimate requirements. As an attractive alternative technology, metal-air battery has recently captured the spotlight as promising sustainable energy conversion and storage technology. Metal-air batteries with the open architecture provide many attractive characteristics containing environmental benignity, high power and energy densities. In addition, with a wide range of selection in different metals determines different energy capacity and efficiency. Among a various types of metal-air batteries, zinc-air battery system has especially been considered as the most mature technology due to its abundance, low cost, ease handling, and safe operation as well as high energy efficiency. However, some technological challenges of zinc-air batteries such as insufficient cycling durability, low charge/discharge activity and efficiency, and poor rate capability still must be addressed for future commercialization. These main challenges interrupting the development of electrically rechargeable zinc-air batteries are primarily due to very sluggish oxygen reduction and evolution reactions generated during discharge and charge processes on air electrode. The slow oxygen reactions create large overpotentials during both discharge and charge processes, which significantly decrease energy efficiency of zinc-air battery. Accordingly, the use of electrocatalysts in air electrode has been highly required to facilitate

the reactions and even propel the zinc-air batteries to practical energy applications. Therefore, it is considerably necessary to develop highly active and durable bi-functional electrocatalysts toward both ORR and OER for the sake of successful commercialization of electrically rechargeable zinc-air batteries. In this point of view, design and synthesis of advanced oxygen electrocatalysts at low cost has been favorably considered. Despite extensive efforts made, however, developing air electrode catalysts with the high activity and the long durability at low cost remain a huge challenge because mostly precious metal-based catalysts such as platinum (Pt) and iridium (Ir) show greatly high activities toward ORR and OER, respectively. However, the use of the materials as electrocatalysts for zinc-air battery is highly challengeable in that they are extremely scarce, expensive, and unstable during the oxygen reactions. Therefore, it is significantly important to develop proper materials which are inexpensive, abundant, and stable during the oxygen reactions, where they are called “non-precious catalysts” primarily composed of transition metals or metal oxides, nano-carbons, and their hybrids. The strong objectives make us focus on the design of a class of novel composite architecture for high-performance electrochemical energy storage, electrically rechargeable zinc-air battery.

In this work, the strategy is based on a fast solvation-induced assembly that directly exploits strong hydrophobicity of both cobalt oxide nanocrystals ( $\text{Co}_3\text{O}_4$  NCs) and Nitrogen-doped carbon nanotubes (N-CNTs). A two-phase method is exploited to prepare the nearly mono-dispersed, highly crystalline, nano-sized cobalt oxide. The reaction of the two-phase system happens at the interface between the oil (nonpolar) and water (polar) phases and the interface is an exclusive site for both nucleation and growth. N-CNTs were synthesized by a single step chemical vapor deposition technique using either ferrocene as a catalyst and

ethylenediamine as a carbon source. Simply at first, cobalt oxide NCs and N-CNTs are dispersed in nonpolar solvent (e.g., toluene). Upon addition of polar solvent (e.g., methanol), solvation forces induce the hydrophobic cobalt oxide NCs to assemble around the hydrophobic CNTs, which leads to the formation of cobalt oxide NCs-decorated on the N-CNTs. As an electrochemical catalyst for air electrode,  $\text{Co}_3\text{O}_4$  nanoparticle is a material with little ORR activity by itself. However, when it is decorated on Nitrogen-doped carbon nanotubes, their hybrid shows unexpected, surprisingly high performance in ORR that is further enhanced by nitrogen doping of N-CNTs. The  $\text{Co}_3\text{O}_4$  NC/N-CNT hybrid exhibits comparable ORR catalytic activity but superior stability to a commercial carbon-supported Pt catalyst in alkaline solutions, thus leading to a novel bi-functional catalyst for ORR. The same hybrid is also highly active for OER, making it a high-performance non-precious metal-based bi-functional catalyst for both ORR and OER. The unusual catalytic activity arises from synergetic coupling effects between  $\text{Co}_3\text{O}_4$  and N-CNTs. The full cell electrochemical catalytic activity is evaluated by preparing air electrodes of rechargeable zinc-air batteries utilizing ambient air to emphasize practicality. The galvanodynamic charge and discharge behaviors are superior to Pt/Carbon and N-CNT counterparts particularly at high applied current densities. Electrochemical impedance spectroscopy reveals that  $\text{Co}_3\text{O}_4$  NC/N-CNT hybrid electrode results in significantly less internal, solid-electrolyte interface, and charge transfer resistances which lead to highly efficient electrochemical reactions. Superior rechargeability has also been confirmed where virtually no voltage drops are observed over 200 pulse cycles. The practicality of  $\text{Co}_3\text{O}_4$  NC/N-CNT hybrid is highlighted by demonstrating comparable discharge voltages and greatly outperforming charge voltages with excellent electrochemical stability than commercial Pt/Carbon catalyst.

## **Acknowledgements**

This work reported herein was financially supported by the Natural Sciences and Engineering Research Council of Canada (NSERC), and University of Waterloo.

First of all, I am deeply grateful to my advisor, Professor Dr. Zhongwei Chen, for his continuous support, mentoring, and encouragement throughout my research. I am deeply impressed with their endless enthusiasm and thirst for academic research. Without their genuine guidance, I could have not accomplished the submission of a paper and the creation of this Master thesis. I also want to express my heartfelt appreciations to my thesis committee members, Professor Dr. Bo Cui, and Professor Dr. Zhongchao Tan for the valuable time they shared in providing helpful comments.

I would also like to deeply thank Dr. Hey Woong Park for helping me to adapt myself to a new circumstances and environments in a new life of lab and school and giving me a wide range of knowledge about the research topics from A to Z.

Special thanks go to Dr. Hoon Sub Song, for always giving me courage to resolve difficulties since I was an undergraduate student and for being my mentor with helpful advices.

Many thanks to Dr. Gwang Bok Yi, Associate Professor at the Department of Chemical Engineering Education, Chungnam National University, Daejeon, Korea, for giving me high quality education as well as essential virtues of a good researcher and even offering me valuable office location for me to have deep study in the chemical engineering and strong interest on this research area.

I also wish to thank many of my friends, especially, Hyunki Bae, Dr. Wook Ahn, Dr. Minho Seo, Tae-Jung Kwon, Yun Suk Jun, Ja-Yeon Choi, Sungho Park, Dong Un Lee, and Brian Kihun Kim for their encouragements and companionships in and outside of my school life.

Most of all, my deepest gratitude goes to my parents, Ji-Yang Park and Mi Seob Shin; my beautiful older sister, Mi Ji Park; my lovely two dogs, SSal and Bori for providing a tremendous wealth of unconditional love and sincere support as well as making my life enjoyable and delightful.

## **Dedications**

*To My Greatest Parents, Ji Yang Park and Mi Seob Shin,*

*&*

*In Memory of My Grandmother, Im Soon Kim, 1922 - 2015*

# Table of Contents

Author's Declaration .....	ii
Statement of Contributions .....	iii
Abstract .....	iv
Acknowledgements .....	vii
Dedications.....	ix
Table of Contents .....	x
List of Figures .....	xii
List of Tables.....	xv
List of abbreviations, symbols and nomenclature.....	xvi
Section 1: Introduction.....	1
1.1 Contents of the Thesis.....	3
Section 2: Background and Literature Review .....	5
2.1 Metal-Air Battery.....	5
2.2 Rechargeable Zinc-Air Battery.....	9
2.3 Operation Principle and Components of Zinc-Air Battery.....	11
2.3.1 Anode: Zinc Electrode.....	16
2.3.2 Electrolyte .....	20
2.3.3 Separator .....	22
2.3.4 Cathode: Porous Air Electrode.....	23
2.4 Air Electrocatalyst .....	26
2.4.1 Precious Metal-Based Catalysts.....	27
2.4.2 Non-precious Transition Metal-Based Catalysts .....	28

2.4.3	Bi-functional Catalysts with Heteroatom-doped Nano Carbon Materials .....	32
2.5	Study Goal and Objective .....	34
Section 3: Characterization Techniques .....		36
3.1	Physical Characterization Techniques .....	36
3.1.1	Scanning Electron Microscopy .....	36
3.1.2	Transmission Electron Microscopy.....	38
3.1.3	X-Ray Diffraction .....	39
3.1.4	X-Ray Photoelectron Spectroscopy .....	40
3.1.5	Brunauer-Emmett-Teller Analysis .....	42
3.1.6	Thermogravimetric Analysis.....	43
3.2	Electrochemical Characterization Techniques.....	44
3.2.1	Half-Cell Testing: Cyclic Voltammetry.....	44
3.2.2	Half-Cell Testing: Rotating Disc Electrode .....	46
3.2.3	Zinc-Air Single Cell testing: Fabrication and Performance Evaluations.....	53
Section 4: Bi-functional Electrocatalysts for Rechargeable Air-Electrode.....		58
4.1	Synergistic effect of hybridizing Spinel Cobalt Oxide with Nitrogen-doped Carbon Nanotubes .....	58
4.1.1	Introduction and Motivation .....	58
4.1.2	Experimental Methods .....	62
4.1.3	Results and Discussion.....	65
4.1.4	Conclusions and Remarks .....	91
Section 5: Directions for Future Researches .....		93
References .....		95

## List of Figures

Figure 1. Theoretical and practical energy densities of various types of rechargeable battery. Reprinted with permission. <sup>10</sup> Copyright 2011, Wiley-VCH. ....	5
Figure 2. Schematic principle of operation for zinc–air batteries. Reprinted with permission. <sup>13</sup> Copyright 2014, The Royal Society of Chemistry.....	11
Figure 3. Schematic polarization curves of zinc-air cell. The equilibrium potential of the zinc-air cell (black line) is 1.65 V, but the practical voltage (red line) in discharge is lower than 1.65 V due to the sluggish ORR. A large potential is needed to charge zinc-air battery, higher than the equilibrium potential (blue line). Reprinted with permission. <sup>10</sup> Copyright 2011, Wiley-VCH.....	14
Figure 4. Various morphology of zinc metal. a) zinc powder, b) zinc dendrite and c) zinc fiber. <sup>51, 52</sup> .....	17
Figure 5. General structure of air electrode in zinc air battery.....	24
Figure 6. Volcano plot of platinum alloys showing theoretical ORR current density as a function of calculated oxygen adsorption energy. Reprinted with permission. <sup>81</sup> Copyright 2009, Macmillan Publishers Limited. ....	28
Figure 7. Polarization curves of different electrodes in KOH aqueous electrolyte: (a) carbon-supported LaMnO <sub>3</sub> , (b) LaMnO <sub>3</sub> /LaNiO <sub>3</sub> (10 wt% LaMnO <sub>3</sub> ), (c) LaMnO <sub>3</sub> /LaNiO <sub>3</sub> (30 wt% LaMnO <sub>3</sub> ), (d) neat LaNiO <sub>3</sub> . The anodic and cathodic polarization corresponds to the electrocatalytic OER and ORR process, respectively. Reprinted with permission. <sup>94</sup> Copyright 2011, The Electrochemical Society.....	31
Figure 8. Cyclic voltammogram of a reversible diffusion-controlled process. Reprinted with permission. <sup>23</sup> Copyright 2001, McGraw Hill. ....	45
Figure 9. Typical setup of three-electrode half-cell testing equipment .....	48
Figure 10. Typical ORR polarization curve in KOH electrolyte .....	50
Figure 11. Linear fitting of K-L plots ( $j - 1$ vs. $\omega^{0.5}$ ) based on the Koutecky-Levich equation at various voltages (vs. SCE). Reprinted with permission. <sup>46</sup> Copyright 2015, Wiley-VCH.....	52
Figure 12. Schematic diagram of rechargeable zinc air prototype.....	54

**Figure 13. (a) Schematic illustration of the charge and discharge processes of zinc air battery at  $\text{Co}_3\text{O}_4$  NC/N-CNT coated GDL for bi-functional electrocatalysis for ORR and OER, (b) Diagram of processes of synthesis for cobalt oxide nanocrystals decorated nitrogen-doped CNT hybrid material by hydrophobic power. .... 61**

**Figure 14. (a) TEM image and (b) XRD pattern of  $\text{Co}_3\text{O}_4$  NCs, and (c) SEM and (d) TEM images of N-CNTs. .... 66**

**Figure 15. (a) SEM, (b) TEM, (c) STEM images of  $\text{Co}_3\text{O}_4$  NC/N-CNT and (d) cobalt and (e) carbon color mapping images obtained from EDX of  $\text{Co}_3\text{O}_4$  NC/N-CNT ..... 67**

**Figure 16. TEM and SEM images of  $\text{Co}_3\text{O}_4$  NC/VC composite..... 70**

**Figure 17. TGA data profiles of  $\text{Co}_3\text{O}_4$  NC/N-CNT ..... 70**

**Figure 18. (a) The XPS survey and (b) high-resolution N 1s spectrum of  $\text{Co}_3\text{O}_4$  NC/N-CNT composite: the grey and black lines are the raw and fitted spectra; the red, olive, blue and wine lines are pyridinic-N (398.5 eV, 42.21 %), pyrrolic-N (400.7 eV, 23.67 %), quatanary-N (401.65 eV, 15.37 %) and pyrrolidone-N (404.7 eV, 18.75 %), respectively. .... 71**

**Figure 19. De-convoluted high-resolution Co 2p spectrum for  $\text{Co}_3\text{O}_4$  NC/N-CNT hybrid catalyst. It revealed two spin-orbit of  $2p^{1/2}$  and  $2p^{3/2}$  configurations each consisting of  $\text{Co}^{3+}$  and  $\text{Co}^{2+}$  cations doublet.<sup>133</sup> The bi-functional catalytic activity of  $\text{Co}_3\text{O}_4$  NC/N-CNT toward both ORR and OER are attributed to synergistic influences from combination between  $\text{Co}_3\text{O}_4$  NC and N-CNT: not only N-CNT provides high electrical conductivity and helps electron transfers, but also cobalt cations support the electron transfer by offering donor-acceptor chemisorption sites for the both reversible oxygen adsorption and desorption from the mixed-valencies of the Co cations coexisting in the same cubic spinel.<sup>133</sup> By this synergistic effect,  $\text{Co}_3\text{O}_4$  NC/N-CNT hybrid catalyst has better electrocatalytic activities and stability than those of N-CNT itself toward both oxygen reactions. Furthermore, the electron transfer occurs by hopping processes between the cations of different valencies which has relatively low activation energy, resulting in  $\text{Co}_3\text{O}_4$  having relatively high electrical conductivity. These excellent electronic properties of cubic spinel  $\text{Co}_3\text{O}_4$  help the hybrid catalyst to**

have synergistic effect and also make it an excellent candidate as a highly efficient catalyst for rechargeable zinc-air battery applications. .... 73

**Figure 20. (a) ORR and (b) OER polarization curves of  $\text{Co}_3\text{O}_4$  NC/N-CNT compared to  $\text{Co}_3\text{O}_4$  NC/VC and N-CNT obtained at rotation speed of 900 rpm, (c) ORR polarization curves of  $\text{Co}_3\text{O}_4$  NC/N-CNT obtained at various rotating speeds (400, 900, 1600 and 2500 rpm), (d) K-L plot of  $\text{Co}_3\text{O}_4$  NC/N-CNT hybrid obtained at 0.65, 0.70, 0.75, and 0.80 V. ORR and OER experiments are conducted in  $\text{O}_2$ - and  $\text{N}_2$ -saturated 0.1M KOH, respectively. .... 74**

**Figure 21. (a) ORR and (b) OER polarization curves for hybrid and Pt/C+Ir/C as the precious metal-based reference sample (900 rpm). ORR and OER experiments are conducted in  $\text{O}_2$ - and  $\text{N}_2$ -saturated 0.1 M KOH, respectively. Scan rate:  $10\text{mV s}^{-1}$  and electrolyte: 0.1 M KOH. Onset potential is measured at -0.01 mA and limiting current is measured at -0.8 V (vs. SCE). .... 78**

**Figure 22. The 1<sup>st</sup> and 1000<sup>th</sup> CV cycle in the OER region obtained with (a)  $\text{Co}_3\text{O}_4$  NC/N-CNT, (b)  $\text{Co}_3\text{O}_4$  NC/VC, (c) N-CNT (300<sup>th</sup>) and (d) Pt/C+Ir/C. .... 80**

**Figure 23. (a, and c) Galvanodynamic charge and discharge behaviors, and (b, and d) Nyquist plots obtained by EIS of  $\text{Co}_3\text{O}_4$  NC/N-CNT (red circle),  $\text{Co}_3\text{O}_4$  NC/VC (wine hexagon), N-CNT (blue triangle), and Pt/C+Ir/C (black half circle). (b, and d insets) High frequency range of the Nyquist plot, and the equivalent circuit. .... 82**

**Figure 24. Galvanostatic charge and discharge (C-D) cycling obtained at  $20\text{ mA cm}^{-2}$  of (a)  $\text{Co}_3\text{O}_4$  NC/N-CNT, (b)  $\text{Co}_3\text{O}_4$  NC/VC, (c) N-CNT, and (d) Pt/C+Ir/C. Insets: The initial 4 cycles of each catalyst. .... 86**

**Figure 25. Long term galvanostatic charge and discharge (C-D) cycling obtained at  $20\text{mA cm}^{-2}$  of  $\text{Co}_3\text{O}_4$  NC/N-CNT. Each charge and discharge state was 2 hours (4 hours per cycle). .... 87**

**Figure 26. (a, and c) Galvanodynamic battery behaviors, and (b, and d) Nyquist plots obtained by EIS after durability cycling test of  $\text{Co}_3\text{O}_4$  NC/N-CNT (red circle),  $\text{Co}_3\text{O}_4$  NC/VC (wine hexagon), N-CNT (blue triangle), and Pt/C+Ir/C (black half circle). (b, and d insets: High frequency range of the Nyquist plot, and the equivalent circuit.) ... 88**

## List of Tables

<b>Table 1. Characteristic data of metal-air batteries.<sup>13,31</sup></b> .....	7
<b>Table 2. Different strategies to improve the performance of the zinc negative electrode. Reprinted with permission.<sup>13</sup> Copyright 2014, The Royal Society of Chemistry.</b> .....	19
<b>Table 3. Summary of half-cell results: onset potential, half-wave potential, maximum current density from ORR polarization curves and cell potential at 20 mA cm<sup>-2</sup> and durability of the catalyst performance, respectively. Onset potential was measured at -0.01 mA cm<sup>-2</sup></b> .....	76
<b>Table 4. The values of the equivalent circuit elements based on the EIS analysis of Co<sub>3</sub>O<sub>4</sub> NC/N-CNT, Co<sub>3</sub>O<sub>4</sub> NC/VC, N-CNT and mix of Pt/C and Ir/C.</b> .....	84
<b>Table 5. Battery voltage obtained at 50 mA cm<sup>-2</sup> during galvanodynamic discharge and charge before galvanostatic C-D cycling test</b> .....	90
<b>Table 6. Battery voltage obtained at 50 mA cm<sup>-2</sup> during galvanodynamic discharge and charge after galvanostatic C-D cycling test</b> .....	90

## List of abbreviations, symbols and nomenclature

AFC	Alkaline Fuel Cell
BET	Brunauer Emmett and Teller
CAL	Catalytic Active Layer
CNT	Carbon Nanotube
CV	Cyclic Voltammetry
CVD	Chemical Vapor Deposition
EDA	Ethylenediamine
EDS	Energy Dispersive X-ray Spectroscopy
EIS	Electrochemical Impedance Spectroscopy
GDE	Gas Diffusion Electrode
GDL	Gas Diffusion Layer
GO	Graphene Oxide
HR-TEM	High Resolution TEM
HR-XPS	High Resolution XPS
Ir/C	Carbon supported Iridium
K-L	Koutecky-Levich
LAB	Lithium Air Battery
LIB	Lithium Ion Battery
LSV	Linear Scan Voltammetry
MAB	Metal Air Battery
MWCNT	Multi-Walled Carbon Nanotube
NCM	Nitrogen-doped Carbon Material

N-CNT	Nitrogen-doped Carbon Nanotube
NPMC	Non-Precious Metal-based Catalyst
N-rGO	Nitrogen-doped Reduced Graphene Oxide
NTMO	Non-Precious Transition Metal Oxide
OCV	Open circuit voltage
OER	Oxygen Evolution Reaction
ORR	Oxygen Reduction Reaction
PEMFC	Polymer Electrolyte Membrane Fuel Cell
Pt/C	Carbon supported Platinum
PTFE	Polytetrafluoroethylene
RDE	Rotating Disk Electrode
r-GO	Reduced Graphene Oxide
RHE	Reversible Hydrogen Electrode
SAED	Selected Area Electron Diffraction
SCE	Saturated Calomel Electrode
SEM	Scanning Electron Microscopy
TEM	Transmission Electron Microscopy
TGA	Thermogravimetric Analysis
VC	Vulcan Carbon
XPS	X-ray Photoelectron Spectroscopy
XRD	X-ray Diffraction
ZAB	Zinc Air Battery

## **Section 1: Introduction**

In our world-wide modern society, most of energy generation and consumption technologies are depending on natural resources such as fossil fuels including coal, oil, and natural gas. This high dependence on the fossil fuels has recently produced significant increase of petroleum price and even a variety of environmental issues associated with global warming. The natural energy resources in the old-fashioned energy technology cannot be utilized eternally and sustainably due to its limited reserves on Earth. They would eventually face depletion even faster than the expectation of world due to today's extremely high demand for energy sources. In addition to this issue, burning the unsustainable energy sources from the nature (e.g. combustion engines in automotive vehicles) has triggered severe air pollution, destruction of ozone layer and dramatic build-up of green-house gases in atmosphere, leading to an unnecessary and tremendous spending for recovering environmental damages. These issues being not welcomed have let world require alternative energy conversion and storage systems from renewable sources as the next generation energy technology so as to avoid the problems mentioned above.<sup>1, 2</sup> New type of energy harvesting, conversion and storage including batteries, super-capacitors and fuel cells, has attracted considerable attentions, presenting an attractive solution for meeting the rapidly expanding demand for energy usage over the modern society and offering low or zero carbon emission, high-efficiency, and excellent energy sustainability.<sup>2, 3</sup> Among the various electrical storage technologies, batteries, particularly, are one of the most efficient, simplest

and reliable systems which not only have long been recognized for their capacity to efficiently convert and store electrical energy, but also currently are utilized in human life the most frequently. In addition, compared to other electrochemical devices, the batteries exhibit high specific energy and power comparable to super-capacitors and fuel cells, respectively.<sup>3-5</sup> Batteries consist of closed system which has two different electrodes with charge transfer media and generate electricity by electrochemical oxidation-reduction reactions. Advantages of batteries contain high operation flexibility in a wide range of conditions, such as pressure and temperature, simple design and configuration, and the good capability to deliver high current pulses.<sup>6, 7</sup> The unique features of batteries enable one to choose the best battery chemistry for specific purpose and applications allowing them to obtain great success over other electrochemical energy conversion and storage systems. Of a various types of battery systems, lithium ion batteries (LIBs) are known to be the most advanced technology and well-commercialized in market with the highest demand. Their typical usages are composed of multiple applications containing portable electronic devices, grid-scale energy storages, and electric vehicles owing to their attractive long cycle life and high energy efficiency compared to traditional battery systems such as nickel-cadmium (Ni-Cd), nickel-metal hydride (Ni-MH), and lead acid batteries.<sup>5, 8-12</sup> In spite of the various and excellent advantages, not only the energy and power densities are not sufficient, but also the cost is too high to meet the high energy requirement for use in electric vehicle (EV) applications.<sup>9, 13</sup> Lithium ion battery pack alone would rate over \$30,000 for a 240 miles range passenger vehicle and this price would be equal to the cost of an entire gasoline-

powered vehicle.<sup>13</sup> Furthermore, LIBs undergo intercalation/de-intercalation chemistry between the negative and positive electrodes and even utilization of irreversible and non-sustainable intercalation compound in the positive electrode considerably decreases the energy density and significantly increases cost of batteries.<sup>14-17</sup> In these points of view, it is very hard for LIBs to encounter the requirements for usage in dramatically energy intensive applications such as electric vehicles (EVs). Consequently, with requirements of an innovation in battery science and technology, a novel type of battery which can satisfy the high requirements for the highly energy intensive electric applications are currently necessary in our modern society.

## **1.1 Contents of the Thesis**

In Section 1, Introduction and contents of the thesis are announced.

In Section 2, relevant background information and literature review with respect to bi-functional electrocatalysts for rechargeable zinc-air batteries are provided including the structure, operation principles, and basic components of rechargeable zinc-air batteries, and the types of nanostructured air electrocatalysts containing precious metal, non-precious metal, functionalized carbon, and their bi-functional catalysts. The study goal and objectives are included at the last section of this chapter.

Section 3 discusses physical, chemical and electrochemical characterization techniques employed for this thesis with a brief theoretical operation principles and purpose of each technique.

Section 4 introduces novel synthesis of highly active and durable bi-functional catalysts hybridizing single spinel-type oxide with nitrogen-doped carbon nanotube with positive synergistic impacts which are beneficial to the better oxygen catalytic performances for electrically rechargeable zinc-air battery.

Section 5 outlines the direction of future research plans, which include the design and synthesis of unique and novel nanostructured bi-functional catalysts which are made up of non-precious transition metal oxide with various supporting materials by facile, unique, and cost effective techniques.

## Section 2: Background and Literature Review

### 2.1 Metal-Air Battery

As one of the proposed alternative to lithium-ion batteries (LIBs), metal-air batteries have recently received a wide range of international interest due to their extremely high energy density compared to that of other types of batteries<sup>8, 10, 13, 18-22</sup>, as shown in **Figure 1**.

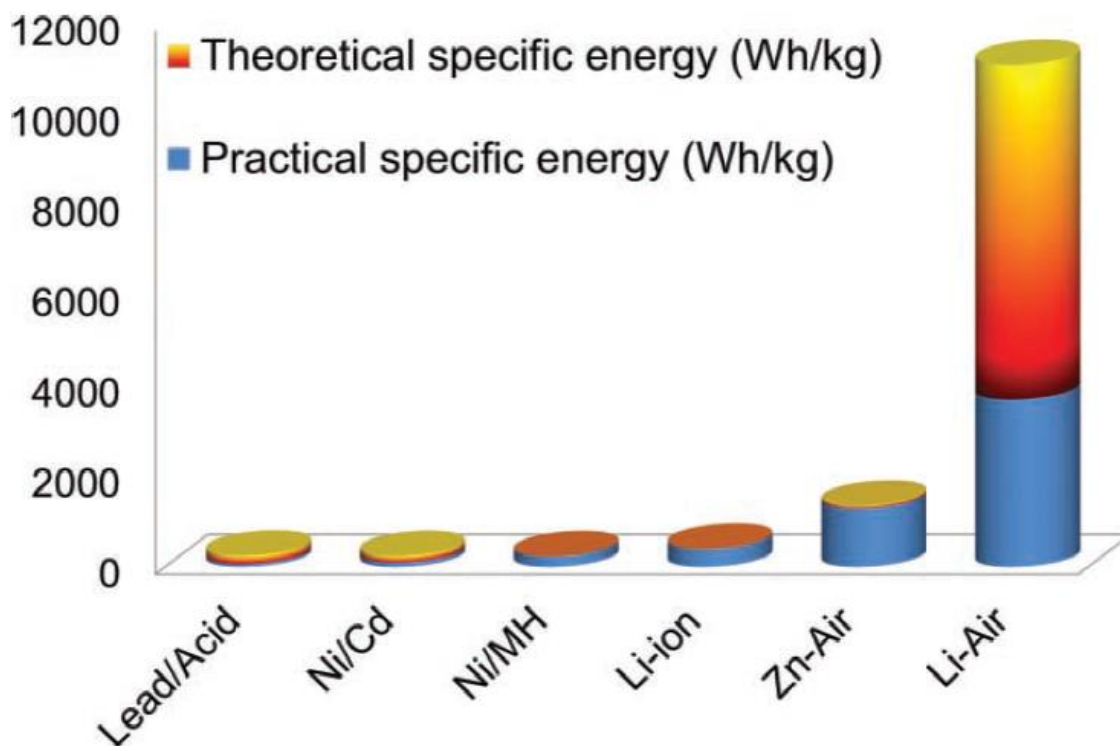


**Figure 1.** Theoretical and practical energy densities of various types of rechargeable battery. Reprinted with permission.<sup>10</sup> Copyright 2011, Wiley-VCH.

The notable characteristics of this technology contain open cell structures with high energy efficiency which are composed of an electrochemical coupling of metal anode and air-breathing cathode with suitable electrolytes.<sup>23</sup> The concept of the metal-air batteries is between traditional batteries and fuel cells. The configuration has two respective design features from both traditional batteries and conventional fuel cells. The utilization of metal as an anode is from the concept of batteries and the usage of porous air-electrode as a cathode is from the feature of fuel cells in that it is necessary for their porous electrode design to use an everlasting oxygen stream from the surrounding air as a reactant. The oxygen utilized as the positive electrode active material is not stored in the system, making possible extremely high theoretical energy densities; about 2-10 times higher than those of lithium-ion batteries.<sup>23</sup> Furthermore, the metal-air batteries present a flat discharge voltage, long cycle life, environment friendly, low cost, and independence of capacitance on load cycle and temperature.<sup>8, 10, 24-30</sup>

A choice of different metals leads to different values such as theoretical energy densities and working potential, and a name of metal-air battery literally depends on their metal anode; zinc-air battery employs zinc metal and lithium-air battery uses lithium metal as its negative electrode, where the two batteries have been the most famous among the several types of metal-air batteries in scientific researches.<sup>8, 18</sup> In addition to the zinc-air and lithium-air batteries, a few more types of metal-air batteries including iron-air, aluminum-air, magnesium-air, sodium-air and potassium-air batteries have been considered. They are

generally classified into two groups by employing aqueous electrolyte or non-aqueous electrolyte.<sup>13</sup>

**Table 1. Characteristic data of metal-air batteries.**<sup>13, 31</sup>

<b>Battery Systems</b>	<b>Electrochemical equivalent of metal (Ah kg<sup>-1</sup>)</b>	<b>Theoretical energy density (Wh kg<sup>-1</sup>)</b>	<b>Theoretical cell voltage with O<sub>2</sub> electrode (V)</b>	<b>Practical operating voltage (V)</b>	<b>Primary or electrically rechargeable</b>
Fe-air	960	763	1.28	1.0	Rechargeable
Zn-air	820	1086	1.65	1.0 - 1.2	Rechargeable
Al-air	2980	2796	2.71	1.1 - 1.4	Primary
Mg-air	2205	2840	3.09	1.2 - 1.4	Primary
Na-air	1166	1106	2.27	2.1	Rechargeable
K-air	686	935	2.48	2.4	Rechargeable
Li-air	3861	11680	2.96	2.6	Rechargeable

One group using aqueous electrolyte consists of zinc-air, iron-air, aluminum-air, and magnesium-air batteries; such systems are not sensitive to moisture, whereas the other group using non-aqueous electrolyte is composed of lithium-air, sodium-air, and potassium-air batteries; they are water-sensitive system using electrolytes with aprotic solvents, as listed at **Table 1**. Among the aqueous group, iron-air has been relatively well-commercialized as an electrically rechargeable battery. Realistic iron-air batteries operate a long cycle life more than 1000 cycles, but their energy density is too low, typically in the range of 60–80 Wh kg<sup>-1</sup>,

to be practically utilized in EV applications.<sup>32</sup> Even though aluminum-air and magnesium-air batteries have high theoretical energy densities and working potentials, practically achievable values are much lower due to the parasitic corrosion reaction such as hydrogen evolution reaction (HER) at the surface of metal anode.<sup>33, 34</sup> Moreover, aluminum-air and magnesium-air are not electrically rechargeable due to thermodynamically impossible electrodeposition of metals for charge process in aqueous electrolyte. Thus, their applications have been directed toward mechanically rechargeable designs and they are candidates for ocean power supplies and underwater vehicle propulsion using oxygen existing in the ocean.<sup>23</sup> Yet few products have been commercialized in the alternative power markets. On the other hand, a non-aqueous group of the metal-air batteries was introduced to the public more recently with gaining rapidly increasing attention.<sup>9, 35-40</sup> Among the non-aqueous systems, lithium-air battery, especially, has been highly attractive due to its very high theoretical energy density and high working potential, 11680 Wh kg<sup>-1</sup> and 2.96 V, respectively.<sup>10, 13</sup> However, its operation electrochemistry in aprotic solvents occurs at a still slower speed than in aqueous electrolytes, and thus this leads to the formation of insoluble metal peroxide or superoxide particles, not only interrupting oxygen diffusion, but also gradually shutting off battery reactions due to an accumulation of undesirable materials at the air electrode.<sup>8, 9, 39, 40</sup> In addition, metal availability, high price, and safety concerns of the lithium-air batteries hinder their development and commercialization. The sodium-air and potassium-air batteries have the similar problems with those from lithium-air batteries keeping them from being developed and commercialized. Although the non-aqueous metal-

air batteries have tremendous potential without doubt, they, unfortunately, are tormented by intrinsic performance limitations containing low power capability and poor cycleability.

## **2.2 Rechargeable Zinc-Air Battery**

Among these several types of metal–air batteries, zinc-air battery in particular is an exceptionally mature technology and the most promising as the next generation energy conversion and storage applications. Unlike other metal-air batteries, zinc metal has various advantages including its high abundance, low cost, and low equilibrium potential. Furthermore, its single cell presents easy and safe operation, environmental benignity, flat discharge voltage, and long cycle-life in alkaline media.<sup>23, 25, 29, 41</sup> Zinc–air batteries have a high theoretical energy density of 1086 Wh kg<sup>-1</sup> (including oxygen), about five times higher than that of the current lithium-ion batteries.<sup>8, 10, 13</sup> Therefore, they have frequently been encouraged as the most feasible alternative, both technically and economically, to substitute lithium-ion batteries for future EV applications. However, commercialization of the battery has been realized only for the primary zinc-air batteries, invented in the late nineteenth century, and they have been utilized in hearing-aid and medical devices.<sup>23</sup>

With the growing concerns in both high-energy required human life and sustainability of the energy conversion and storage systems, electrically rechargeable zinc-air batteries, in particular, have received a wide of attentions.<sup>18, 42-46</sup> Thus, a lot of researches have rigorously been carried out so as to make the system have a better rechargeability and longer

cycleability and the results also have indicated that the electrically rechargeable zinc-air battery is the most promising energy conversion and storage system which can be commercialized for multiple markets containing electric vehicles (EVs).<sup>13</sup>

In spite of their great potential for the next generation energy technology, the development of electrically rechargeable zinc-air batteries has been interrupted by technical problems in between the metal anode and air cathode. Among the technical problems disturbing further development of the electrically rechargeable zinc-air battery, the lack of satisfactory bi-functional electrocatalysts has been the most critical problem. First of all, in order to understand necessity of the “bi-functional” catalyst, simple zinc-air battery electrochemical mechanism is required. During discharge process, oxygen goes into the open-structured cathode and it is reduced into hydroxide ions ( $\text{OH}^-$ ), which is called oxygen reduction reaction (ORR). Zinc metal simultaneously is oxidized into zinc ion ( $\text{Zn}^{2+}$ ) and finally makes zincate ion (further zinc oxide) by a reaction with hydroxide ions ( $\text{OH}^-$ ) which is migrated from the cathode *via* ORR. A charge process happens *via* reversed discharge reactions with creating oxygen at the positive electrode, called oxygen evolution reaction (OER). As already shown in the above **Table 1**, the practical discharge voltage is about 1.2 V, while the empirical charge potential is usually higher than 2 V, where the charge potential is considerably harsh for air electrocatalysts during battery charging.<sup>13, 23, 42, 44, 47</sup> Furthermore, ORR-based electrocatalysts typically have insufficient activity toward OER whereas OER-based electrocatalysts have unsatisfactory activity toward ORR. In this context, the “bi-functional” means that an electrocatalyst has high catalytic activity toward

both ORR and OER. Accordingly, the bi-functional air catalyst must be successfully developed in order to realize a wide range of utilizations of electrically rechargeable zinc-air batteries in human life.

### 2.3 Operation Principle and Components of Zinc-Air Battery

The structure of a zinc-air battery is schematically presented in **Figure 2**, which consists of a zinc anode, alkaline electrolyte, a porous air electrode, and a membrane separator soaked in the electrolyte.

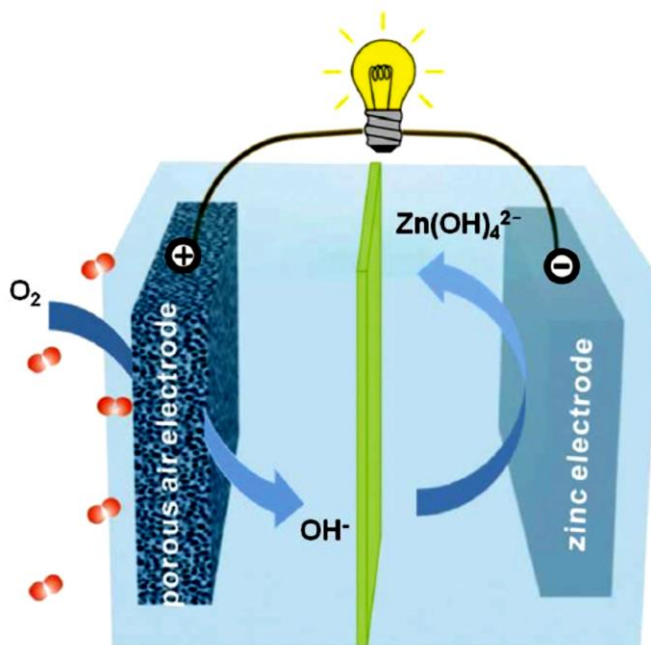
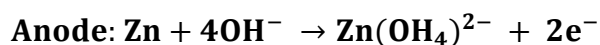
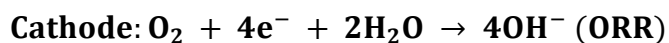


**Figure 2.** Schematic principle of operation for zinc–air batteries. Reprinted with permission.<sup>13</sup> Copyright 2014, The Royal Society of Chemistry.

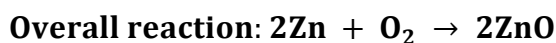
Upon a battery discharge process, oxidation of the zinc anode occurs and zinc metal ions are first generated, where they directly change into soluble zincate ion ( $Zn(OH_4)^{2-}$ ), releasing electrons to the external circuit. This process usually continues until the zincate ions are saturated in the electrolyte and then they decompose to insoluble zinc oxide by a high concentrated electrolyte solution. In the air cathode, at the same time, oxygen, which is the primary reactant for the air cathode, from the surrounding air goes into the porous cathode and reacts with water molecules and electrons on the surface of the electrocatalyst which are from the electrolyte and the anode reactions via external circuit, respectively. In this reaction, oxygen molecules get reduced into hydroxide ions ( $OH^-$ ), which is called oxygen reduction reaction (ORR), and then they migrate into the zinc anode past the separator in order to react with the zinc ions to form the zinc oxide, thereby completing the battery reactions. By combining the anode and cathode reactions, the overall theoretical battery voltage, typically called “open circuit voltage (OCV)”, of the zinc-air battery is 1.65 V, where  $E_{battery}^0 = E_{cathode}^0 - E_{anode}^0$ .<sup>13</sup> The all of the mentioned reaction processes are shown by the equations below.



$$(E_{anode}^0 = -1.25 \text{ V (vs. NHE)})$$



$$(E_{cathode}^0 = 0.4 \text{ V (vs. NHE)})$$



$$(E_{battery}^0 = 1.6 \text{ V (vs. NHE)})$$



For the zinc-air battery to be rechargeable, a charge process is obtained by reversing the discharge process with zinc metal plating on the surface of the zinc anode and oxygen evolving at the air cathode, which is called oxygen evolution reaction (OER). Although the theoretical equilibrium potential of the rechargeable zinc-air battery is 1.65 V, the practical battery working voltage is less than the theoretical equilibrium potential during the discharge process.<sup>13</sup> During the charge process, on the other hand, the practical battery potential is higher than the theoretical potential. This is called “overpotential” stemming from some influential problems such as the internal loss of cell activation, and ohmic and concentration losses.<sup>10</sup>

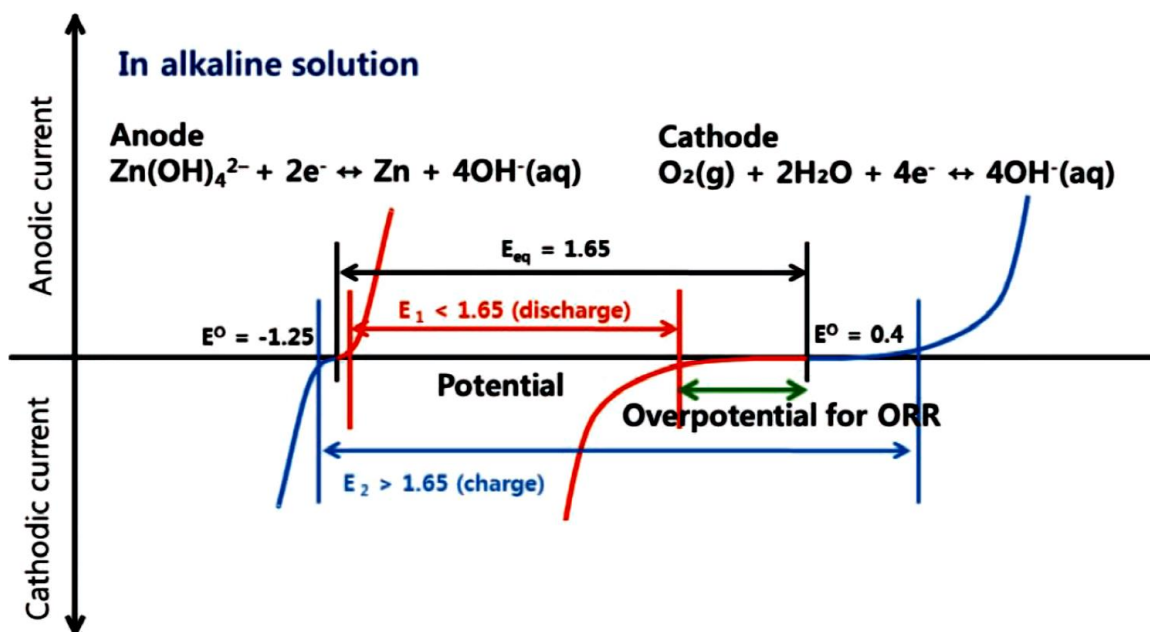


**Figure 3.** Schematic polarization curves of zinc-air cell. The equilibrium potential of the zinc-air cell (black line) is 1.65 V, but the practical voltage (red line) in discharge is lower than 1.65 V due to the sluggish ORR. A large potential is needed to charge zinc-air battery, higher than the equilibrium potential (blue line). Reprinted with permission.<sup>10</sup> Copyright 2011, Wiley-VCH.

Schematic polarization curves of zinc-air battery are shown in **Figure 3** so as to efficiently understand the major origin of the overpotential in zinc-air battery. Basically, the theoretical equilibrium potential of the zinc-air battery is 1.65 V and it is highlighted in black lines. The cathodic current occurs at the air electrode (cathode at the right) and the anodic current occurs at the zinc electrode (anode at the left), where the red lines and the blue lines are exhibiting current profiles during discharge process and charge process, respectively. At the air electrode, in particular, the big overpotential (green line) is shown during the battery discharging, where it is necessary to generate hydroxide ions by oxygen reduction reaction

(ORR). During the battery charging, on the other hand, oxygen evolution reaction happens and oxygen is created while the large overpotential is required.

As a positive part of the use of oxygen, it is possible for the zinc-air battery to have high energy density due to its open cell structure by needlessness of oxygen active material in the cathode, but very sluggish oxygen reactions, as a negative part, make considerable voltage loss and as a result the large overpotential is one of the critical problems in operation of zinc-air battery. This is mainly why the practical working potential of the zinc-air battery is much lower or higher than 1.65 V (theoretical OCV of zinc-air battery) during discharge and charge processes, respectively.<sup>10, 13</sup> In order to reduce the large voltage loss during the battery discharge and charge, which are correspond to the overpotential by ORR and OER, respectively, a variety of studies have deeply focused on the development of bi-functional electrocatalysts and the optimization of air electrode design.<sup>42, 44-46, 48, 49</sup> Of course, it is also presented that overpotential at the zinc electrode, which is far less than that at the cathode, and it also must be decreased by scientific efforts. The use of zinc electrode in primary zinc-air battery typically does not cause problems due to the fact that the utilized zinc metal can be either removed or replaced to fresh zinc metal, called mechanically rechargeable zinc-air battery. For being used in electrically rechargeable zinc-air battery, however, the anode should be repeatedly recharged via OER and a big obstacle comes from the anode part in the zinc-air battery.<sup>50</sup> In addition to the above several drawbacks, some other problems could be obstacles in developing an electrically rechargeable zinc-air battery. Further discussions will be provided in the following sections, where each component of zinc-air battery is

introduced and simultaneously technical challenges from each component are also discussed with possible solutions.

### **2.3.1 Anode: Zinc Electrode**

Zinc metal has long been recognized as a negative electrode (anode) material in a variety of primary battery systems including zinc-manganese dioxide, zinc-nickel, and zinc-air batteries.<sup>23</sup> Zinc has a series of advantages such as low equivalent weight, high specific energy density, abundance and low cost, environmental benignity, and high reversibility and stability in alkaline electrolyte without severe corrosion.<sup>23, 29, 50</sup> In the zinc-air battery, zinc is utilized as the fundamental anode reactant. During a battery discharge process, zinc metal is oxidized creating both electrons and zincate ions into external circuit and adjacent electrolyte, respectively. When the zincate ions are fully-saturated in the alkaline electrolyte, they start to decompose and form insoluble zinc oxide which acts as an insulator, where it typically restricts energy efficiency and durability of the zinc-air battery. During charging the battery, the above steps are reversely performed in which some of zinc oxide reacts with water and hydroxide ions generating zincate ions and zincate ions in the electrolyte are also transformed into zinc ions, and eventually re-plate the zinc electrode.<sup>13</sup> In this context, not only highly efficient utilization of zinc during the battery discharge, but also fairly proficient return of zinc source by re-plating the zinc electrode is greatly important for the development of electrically rechargeable zinc-air battery.



**Figure 4.** Various morphology of zinc metal. a) zinc powder, b) zinc dendrite and c) zinc fiber.<sup>51, 52</sup>

As a high surface area of zinc is generally considered as the most important way to improve the electrochemical performance at the zinc anode side, a number of researches have been directed toward increasing the surface area of zinc anode and they have been implemented especially by controlling morphology of zinc metals. As a result, high surface structured zinc metals including zinc powders, spheres, flakes, ribbons, dendrites, fibers, and foams have been presented in the literature (**Figure 4**).<sup>51-55</sup> Among the various types of zinc anode, fibrous zinc anode, in particular, exhibits highly advantageous performance in zinc-air battery owing to its high porosity and effective surface area, good electrical conductivity, and mechanical stability.<sup>52</sup> However, increasing the zinc electrode surface area also considerably promotes the self-corrosion rate of the zinc electrode via hydrogen evolution reaction (HER).<sup>50</sup> This side reaction significantly limits the battery energy density and decreases the battery lifetime by lowering efficient utilization of the zinc anode and evaporating electrolyte, respectively. In addition to HER which can occur mainly during

battery discharge process, shape change and dendritic growth which can happen during repeated charge-discharge cycling process is also one of the detrimental problems for the electrically rechargeable zinc-air battery.<sup>13</sup> It is primarily induced by zinc electrode's non-uniform dissolution and deposition during battery cycling, and also by decreased efficiency of zinc plating during charge process.<sup>10</sup> This negative event makes unexpected zinc growth, gradually consumes available zinc sources, and as a result significantly diminishes the battery cycle-life. Therefore, many different efforts have been carried out in order to overcome these severe problems interrupting the way to development of the electrically rechargeable zinc-air battery. They could be simply categorized as the following three ways; (1) alloying zinc with other metals, (2) introducing chemical additives to zinc electrode, (3) coating the zinc metal with other materials, as classified in **Table 2**.<sup>13</sup>

**Table 2. Different strategies to improve the performance of the zinc negative electrode. Reprinted with permission.<sup>13</sup> Copyright 2014, The Royal Society of Chemistry.**

<b>Modifications to the zinc electrode</b>	<b>Effects</b>
Alloys with Pb, Cd, Bi, Sn, In, Mg, Al or Ni	Suppress H <sub>2</sub> generation, reduce dendrite formation, improve cycling reversibility
Surface coating with Al <sub>2</sub> O <sub>3</sub> or lithium boron oxide	Suppress H <sub>2</sub> generation and self-discharge
Inorganic additives: Ca(OH) <sub>2</sub> , Bi <sub>2</sub> O <sub>3</sub> , Ti <sub>2</sub> O <sub>3</sub> , Ga <sub>2</sub> O <sub>3</sub> , In <sub>2</sub> O <sub>3</sub> , In(OH) <sub>3</sub> , HgO, PbO, CdO or silicates	Suppress H <sub>2</sub> evolution, reduce dendrite formation, improve discharge performance and cycling reversibility
Polymer additives: ionomers, PEG, PMMA, polypyrrole, polyaniline, poly(vinyl acetate) or polycarbonate	Restrict the dissolution of discharge product, reduce dendrite formation and shape change
Surfactant additives: perfluorosurfactants, CTAB, TBABr, tetra-alkyl ammonium hydroxides, triethanolamine or lignosulfonate	Suppress H <sub>2</sub> generation and electrode corrosion, reduce dendrite formation

As an example of the first way, alloying zinc with mercury (Hg) has been introduced in order to slow down or suppress the rate of the side reaction, where it induces the amalgamation of the zinc at the beginning of HER and the corrosion rate of the zinc is much slowed down.<sup>56, 57</sup> However, the utilization of mercury is restricted due to their high toxicity and negative environmental effects. As alternative solutions, alloying zinc with other metals such as Pb, Cd, Bi, and In has been introduced and it makes the zinc anode more stable.<sup>58-60</sup> As an example of the second method, calcium hydroxide coating on the zinc electrode has been presented so as to reduce the solubility of the zinc discharge products and further achieve the better cycleability, where it makes an insoluble zincate compound close to zinc

electrode, allow the reciprocal transformation between zinc ion and zinc metal at a high speed, and makes a distribution of zinc more uniform during the battery cycling.<sup>61-63</sup> As an example of the third manner, surface coating with aluminum oxide has been exhibited so as to improve the comprehensive zinc anode property, where it minimizes self-corrosion rate and decreases hydrogen evolution reaction (HER).<sup>64, 65</sup> As seen at the above, a number of efforts have been carried out by trying to solve the problems generated at the zinc anode during the battery cycling, but it is still necessary to deeply understand the chemistry and behavior of the zinc in alkaline media so as to make successfully operative electrically rechargeable zinc-air battery.

### **2.3.2 Electrolyte**

Alkaline solutions are typically utilized for zinc-air battery operation due to the fact that metallic zinc has good reversibility and stability in the alkaline condition, and thus potassium hydroxide (KOH) and sodium hydroxide (NaOH) are mainly used for the electrolyte in the zinc-air battery. The use of KOH is relatively more favored than the use of NaOH because KOH has the lower viscosity, higher oxygen diffusion coefficients, and better ionic conductivity, K<sup>+</sup> ( $73.50 \Omega^{-1}\text{cm}^2$ ) and Na<sup>+</sup> ( $50.11 \Omega^{-1}\text{cm}^2$ ). Typically, highly concentrated alkaline solution (6 M) is adopted so as to reduce the resistance of the electrolyte and obtain the higher electric conductivity.<sup>66</sup>

During the battery cycling, however, carbonate precipitation is generated between hydroxide ions and atmospheric carbon dioxide in the high concentrated alkaline solution and it is one

of the serious challenges for the rechargeable zinc-air battery.<sup>13</sup> Normally, these products decrease the concentration of hydroxide ions in the electrolyte, where they are necessary for the zinc-air battery to be discharged, and it eventually triggers the reduction of cell capacity. Furthermore, the carbon precipitations can block the pores of air electrode and significantly reduce the battery lifetime. For example, a reaction between KOH and atmospheric CO<sub>2</sub> produces either K<sub>2</sub>CO<sub>3</sub> or KHCO<sub>3</sub>, and they have higher solubilities than the reaction products between NaOH and CO<sub>2</sub>, while presenting the advantage of utilization of KOH as the zinc-air battery electrolyte.

Since the zinc-air battery is the open structured design, evaporation of the liquid electrolytes also can be a great challenge during the battery cycling. Due to some influential problems such as the aforementioned HER and carbonated precipitations, the liquid electrolyte is dehydrated and it increases the viscosity and the concentration of detrimental materials including insoluble zinc oxides in the electrolyte, and eventually accelerate their vicious circle resulting in considerable decrease of energy efficiency, battery capacity, and battery lifetime. Therefore, many studies has been rigorously tried to develop a new type of electrolyte and it is found that gelled electrolyte can help reduce the liquid loss, and improve the battery performance and cycleability.<sup>25, 67-69</sup> It also can help to get higher flexibility in battery design and thus enlarge the number of available applications with alleviated worries of electrolyte leakage. On the other hand, the gelled electrolyte has high viscosity, low electric and ionic conductivity, and high resistance of electrolyte resulting in severe battery performance loss. It is still necessary to improve the critical disadvantages with continuous

studies in gel-type electrolytes.

### **2.3.3 Separator**

The separator in the zinc-air battery has a simple role in physically setting the zinc anode apart from the air cathode, but migration of hydroxide ions through the separator between the anode and cathode is essential for the completion of the battery chemistry.<sup>10</sup>

Although the separator relatively is not critical for obtaining higher performance of the zinc-air battery among the components of the battery such as zinc anode, air cathode, electrolyte, and separator, a several features are necessary for the separator to be utilized in the zinc-air battery. The electrically inactive element must have a high electric resistance and ionic affinity, and a good chemical stability against corrosive electrolyte. Furthermore, a robust mechanical structure is also highly important so as to tolerate a possible penetration of irregularly grown zinc dendrites which can be generated by operation of rechargeable, and thereby the separator contributes to a longer lifetime of the battery.<sup>13</sup>

Typically, separators are composed of polymer-based materials such as polyethylene (PE), polypropylene (PP), polyvinyl alcohol (PVA), and polyamide, and their fibrous structure produces a high porosity, which is necessary for a high absorption capability of electrolyte and a high ionic affinity. For example, Celgard 5550 is one of the nonwoven polymeric separators generally used in the commercial zinc-air batteries, where it is a layered structure with three polymer layers (PP/PE/PP).<sup>70-73</sup> As one disadvantage, however, the high porosity of the polymer separator provides easy migration of soluble zincate ions from the zinc anode as well as the movement of hydroxide ions from the air cathode, where it gives rise to the

insoluble zinc oxide in the electrolyte of cathode part and damages the air electrode, and eventually decreases the battery cycling efficiency. As a solution for the drawback, anion-exchange membranes in which only hydroxide ions, OH<sup>-</sup>, pass through have been developed and employed.<sup>74</sup> In spite of the advantage, their inadequate stability in a high pH electrolyte such as 6M KOH interrupts their utilization as a separator in the zinc-air battery.<sup>75</sup> More time and efforts are still required to reach to a successful development of the anion-exchange membranes for the electrically rechargeable zinc-air battery.

### **2.3.4 Cathode: Porous Air Electrode**

Unlike the conventional battery electrode where the active material is necessarily inside of the electrode and even it is majority of the electrode, the air electrode of zinc-air battery does not have to possess active material due to the fact that oxygen in the surrounding air is the active material of zinc-air battery and it is supplied into the air electrode eternally, which is as one of the advantages of zinc-air system.<sup>8, 13</sup> Therefore, diffusion of oxygen is highly important for oxygen reduction reaction (ORR) and oxygen evolution reaction (OER), which are the basic reactions in electrically rechargeable zinc-air battery system, during discharging and charging the battery, respectively. However, oxygen is gas phase and it is typically difficult to be diffused into the air electrode and even encounter the liquid electrolyte for the completion of oxygen reactions. Thus, an ability to diffuse oxygen from the air is one of the necessary requirements. In addition to the diffusion effect, the air

electrode also needs a catalyst which can alleviate the activation energy of the oxygen reactions meaning that a catalyst can decrease overpotentials during ORR and OER.

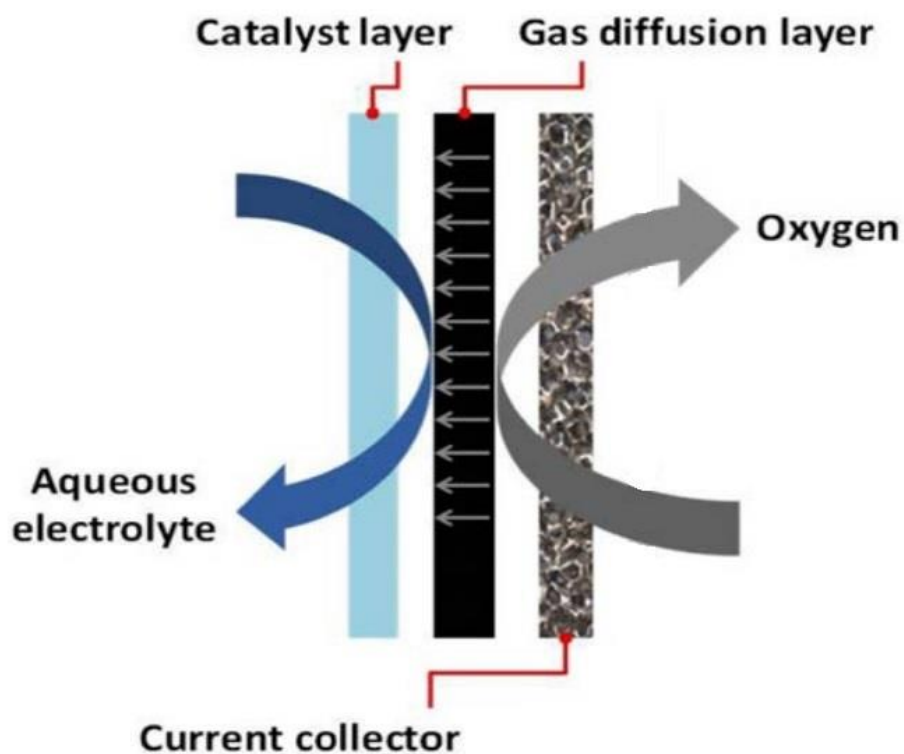


**Figure 5. General structure of air electrode in zinc air battery**

The common structure for the air electrode, which is presented in the **Figure 5**, is composed of two main layers, where one is the catalytic active layer (CAL) and the other one is the gas diffusion layer (GDL). Additionally, there should be a current collecting layer to connect the cathode to the zinc anode, where the current collecting layer should have a high conductivity

and a strong resistance to corrosion by oxygen. Thus, highly conductive stainless steel and nickel metal mesh are primarily utilized as the current collector.

Since the GDL is between the liquid electrolyte and oxygen atmosphere, it is relatively hard for the two elements to encounter each other. Therefore, both hydrophilicity and hydrophobicity are highly significant in the air electrode design. The one side of GDL should have hydrophobic property for the sake of a gas affinity, where diffusion of oxygen is easily carried out into the pores in the GDL. Furthermore, the hydrophobic layer acts as a barrier for avoiding electrolyte penetration. The other side of GDL, on the other hand, should be hydrophilic so as to get a better contact with liquid electrolyte decreasing the interfacial resistance between GDL and electrolyte. Moreover, the GDL is typically porous structure so as to readily receive oxygen from the outside and to provide high surface area for more active oxygen reactions. In this context, GDL is mostly composed of carbon materials and polytetrafluoroethylene (PTFE) in order to obtain high porosity and help the carbon powders assemble together as well as gain hydrophobicity on the one side.<sup>13</sup>

As the last part among the three layers in GDL, prepared electrochemical catalysts are laminated on the catalytic active layer by various methods such as spray coating, brush painting, and slurry covering.<sup>10, 42, 44, 76, 77</sup> Before deposition of the catalyst layer onto the hydrophilic side of GDL, catalyst needs to be prepared into an ink phase by mixing with binder solutions such as PTFE and Nafion as well as aqueous solvents such as ethanol, isopropanol, and water. A variety of electrocatalysts for oxygen reduction reaction (ORR)

and oxygen evolution reaction (OER) have been introduced with an ultimate goal for accomplishing the better battery performance such as high activity and stability during the battery cycling.

## **2.4 Air Electrocatalyst**

In order to decrease overpotentials during the cathodic reactions such as oxygen reduction reaction (ORR) and oxygen evolution reaction (OER), the electrocatalysts require an ability to relieve the high activation energy of the oxygen reactions and accelerate speed of the oxygen reactions, which are intrinsically very sluggish, resulting in improved charge-discharge efficiency of the zinc-air battery. Accordingly, a variety of air electrocatalysts have been rigorously investigated due to the fact that it is highly critical for improving the zinc-air battery performance such as power and energy densities, cycling capability, and overall energy conversion efficiency. A wide range of the electrocatalysts has been employed and they can be roughly categorized into the following three classifications: (1) precious metal-based materials; (2) non-precious transition metal-based materials; lastly (3) bi-functional catalyst with heteroatom-doped nano carbon materials.

In this work, a development of bi-functional catalysts has been studied by using the above catalysts via novel methods, resulting in unexpected and outstanding synergistic effects for improving the performance of the zinc-air battery. In the following sections, not only the each electrocatalysts classified above will be introduced and briefly discussed, but also the

bi-functional catalysts, at the last section, will be dealt with by introducing some efficient synthesis and utilization for the electrically rechargeable zinc-air battery.

### 2.4.1 Precious Metal-Based Catalysts

As one of the highly precious metal, platinum (Pt) is the most effective electrocatalyst for ORR due to its extremely superior electrocatalytic ORR activity. Thus, Pt is often decided as a benchmark ORR catalyst in most of current studies. In addition to platinum, palladium and iridium are also precious metals which are highly active toward ORR and OER, respectively.<sup>8, 13, 44, 46, 48, 78</sup> However, they all have crucial problems including very severe scarcity and significantly high prices as well as insufficient stability during the oxygen reactions.<sup>44, 46, 48, 79, 80</sup> These critical problems make the precious metals not suitable for electrically rechargeable zinc-air battery. Furthermore, they have only uni-functional performances showing either ORR or OER. Accordingly, effective bi-functional catalysts based on the precious metals have usually been accomplished recently by alloying the different precious metals, as shown in volcano plots in **Figure 6**. For example, an air electrode which is composed of palladium catalyzed porous nickel has been presented to demonstrate acceptable bi-functional performance, even though it shows poor cycle stability lasting only 50 cycles due to dissolution of palladium. Moreover, precious metal oxides including IrO<sub>2</sub> and RhO<sub>2</sub>, and their mixed oxides such as NiIrO<sub>3</sub> and CoIrO<sub>3</sub> have been reported so as to exhibit high bi-functional activity and reasonable stability, however, their

high prices owing to the scarcity of these precious metals hinders extensive utilization and commercialization.<sup>31</sup>

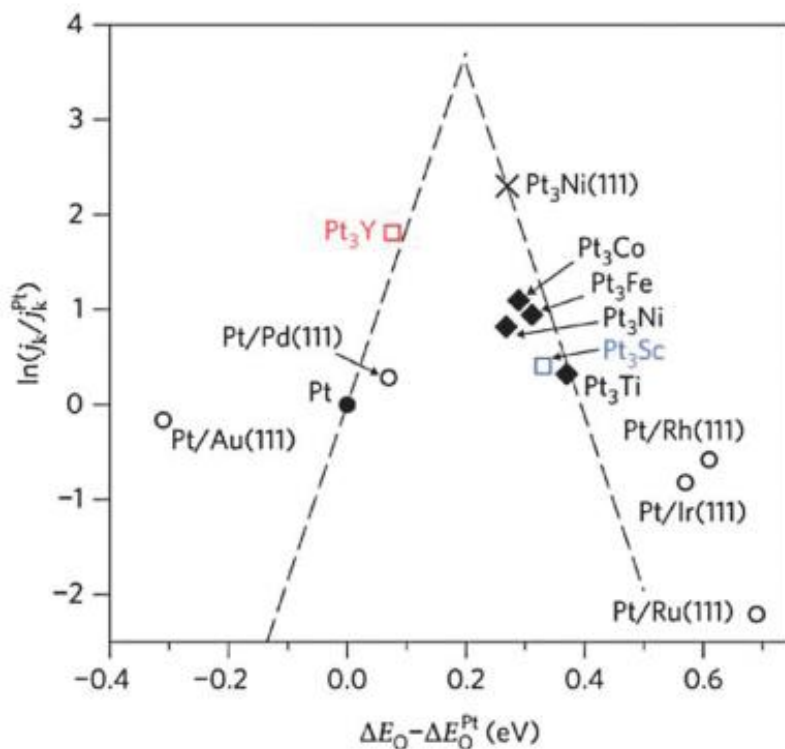


**Figure 6.** Volcano plot of platinum alloys showing theoretical ORR current density as a function of calculated oxygen adsorption energy. Reprinted with permission.<sup>81</sup> Copyright 2009, Macmillan Publishers Limited.

## 2.4.2 Non-precious Transition Metal-Based Catalysts

In order to alternate the precious metal-based electrocatalysts in alkaline electrolytes, non-precious transition metal-based (*e.g.*, Mn, Fe, Co and Ni, *etc*) catalysts can be employed with their prominent advantages such as high abundance, low cost, easy preparation, and

environmental friendliness. With a variety of configurations such as single metal oxides and mixed metal oxides, these types of catalysts, in general, have relatively high current rate capabilities and great electrochemical stabilities.

In general, the ORR and OER are surface-structure sensitive reactions onto electrodes and the reactions occur at active sites on the oxide surface.<sup>8, 13, 18</sup> Thus, the chemical composition, morphology, oxidation state, crystalline structure, and texture of transition metal oxides have been extensively investigated so as to obtain a desired electronic structure resulting in good electrochemical properties and high activities. Typically, the transition metal oxides are categorized into the three following classifications based on their unit-cell architectures: (1) spinel-type oxides ( $\text{Co}_3\text{O}_4$ ,  $\text{NiCo}_2\text{O}_4$ , etc); (2) perovskite-type oxides ( $\text{LaNiO}_3$ ,  $\text{LaMnO}_3$ , etc); (3) pyrochlore-type oxides ( $\text{Pb}_2\text{Ru}_2\text{O}_{7-x}$ ,  $\text{Pb}_2\text{Ir}_2\text{O}_{7-y}$ , etc).<sup>18</sup> The spinel has a formula  $\text{AB}_2\text{O}_4$ , where A is a divalent metal ion containing Fe, Co, Ni, or Mn and B is a trivalent metal ion including Al, Fe, Co, Cu, or Mn. In the spinel structure,  $\text{A}^{2+}$  and  $\text{B}^{3+}$  occupy of the tetrahedral and octahedral sites, respectively, and the component of the  $\text{A}^{2+}$  or  $\text{B}^{3+}$  can be varied so as to modify and optimize the electrocatalytic performance. With the mixed-valences, they present electrical conductivity or semi-conductivity, and the electron transfers occur *via* relatively low activation energies, giving rise to low electrical resistance of the spinel oxides. Transition metal oxides with the spinel structure exhibit high catalytic activities toward oxygen reduction and evolution in alkaline solutions.<sup>82-86</sup> For example, spinel type cobalt oxide ( $\text{Co}_3\text{O}_4$ ) is a promising candidate of non-precious metal-based electrocatalyst with showing bi-functional ORR and OER performances due to its high

electrocatalytic activity and durability so as to minimize the cost and weight of electrically rechargeable zinc-air battery.<sup>45, 87, 88</sup> In the  $\text{Co}_3\text{O}_4$  crystal structure, two valences of  $\text{Co}^{2+}$  and  $\text{Co}^{3+}$  ions are contained together and these play a crucial role in bi-functional performance where they behave as donor–acceptor chemisorption sites for reversible oxygen adsorption.

The perovskite has a general formula  $\text{ABO}_3$ , which has been rigorously researched due to its bi-functional catalytic activity in alkaline electrolytes. Typically, A-site cation mainly affects the ability of adsorbed oxygen, while B-site cation influences the activity of the adsorbed oxygen.<sup>89, 90</sup> Moreover, the properties such as electrocatalytic activity can be alternated by replacing A and B site cations with other metal ions, where A is mainly a rare-earth or alkaline-earth metal and B primarily is a transition metal. The activity of the transition metal oxide catalysts can correlate with the ability of the B site cations to adopt different valency states, especially when the A and B site cations form redox couples at the potentials of ORR and OER. Therefore, different perovskite type oxides with various replacements have been studied as bi-functional catalysts, suggesting their hopeful utilization in electrically rechargeable zinc-air battery.<sup>91-93</sup> For instance, a recent study introduced an air electrode which is composed of two different perovskite-type oxides,  $\text{LaNiO}_3$  and  $\text{LaMnO}_3$ , and their harmony exhibited highly bi-functional oxygen reaction activities as shown in **Figure 7**.<sup>94</sup>

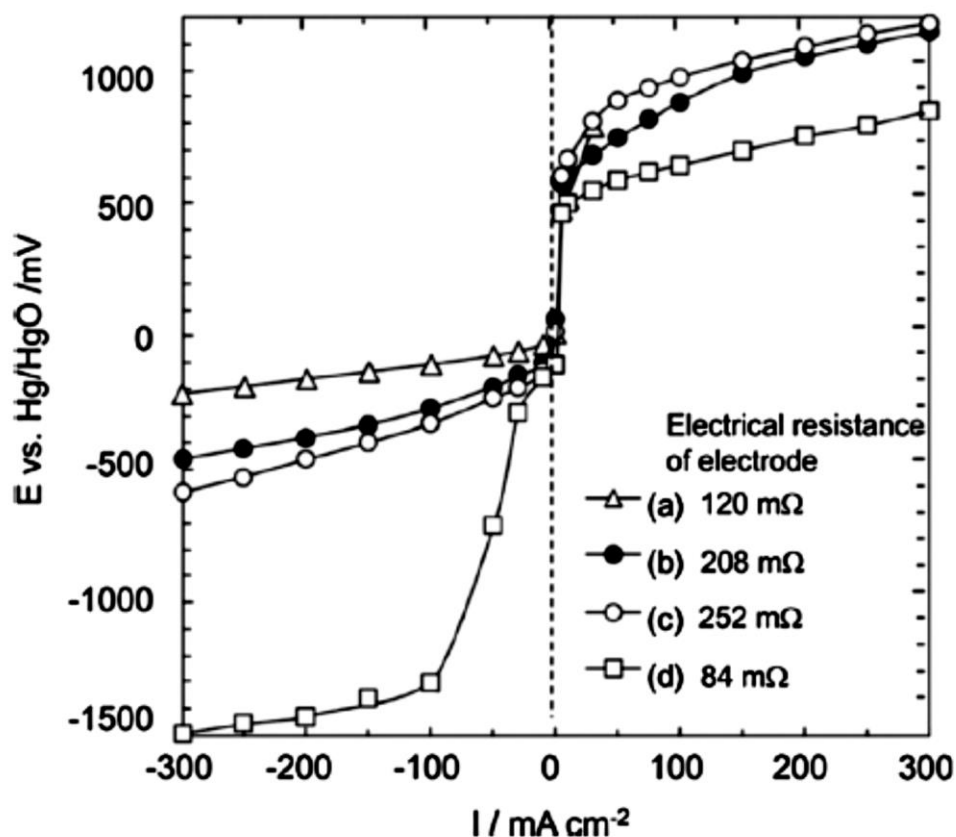


**Figure 7. Polarization curves of different electrodes in KOH aqueous electrolyte: (a) carbon-supported  $\text{LaMnO}_3$ , (b)  $\text{LaMnO}_3/\text{LaNiO}_3$  (10 wt%  $\text{LaMnO}_3$ ), (c)  $\text{LaMnO}_3/\text{LaNiO}_3$  (30 wt%  $\text{LaMnO}_3$ ), (d) neat  $\text{LaNiO}_3$ . The anodic and cathodic polarization corresponds to the electrocatalytic OER and ORR process, respectively. Reprinted with permission.<sup>94</sup> Copyright 2011, The Electrochemical Society.**

However, transition metal oxides have intrinsically low electrochemical conductivity owing to their semiconducting property compared to those of metal and carbon-based materials, resulting in impeding transfer of charges and triggering high electrical resistances during the oxygen reactions. Furthermore, transition metal oxides have limited active area on their surface where it decreases the number of available oxygen reaction sites, even though they

have special crystalline structures such as spinel and perovskite which are highly active toward both ORR and OER. Accordingly, it has been highly necessary to make hybrid catalysts where the transition metal oxides are firmly combined with a greatly conductive substrate such as functionalized nano-carbon materials containing graphene and carbon nanotube (CNT). From this kind of combination, un-expected synergistic effects have been reported in recent studies, where the harmonious combination realizes better bi-functional electrochemical catalysis than the case in which a single component is utilized to make an electrocatalyst.<sup>8, 18, 44, 46, 77, 95</sup> Further discussions will be more deeply handled in the following section about bi-functional electrocatalysts.

### **2.4.3 Bi-functional Catalysts with Heteroatom-doped Nano Carbon Materials**

In order to make zinc-air battery properly electrically rechargeable, oxygen reduction reaction (ORR) and oxygen evolution reaction (OER), which are fundamental air electrode reactions that govern the overall battery operation, must be catalytically activated by a bi-functional oxygen electrocatalyst. Therefore, developing highly active, durable and cost-effective bi-functional electrocatalysts for air electrodes is critical for future implementation of this technology. To date, noble metal-based catalysts such as platinum and iridium on carbonaceous supporting materials (Pt/C and Ir/C) currently have been known as the best ORR and OER electrocatalyst, respectively, however, their severe scarcity and high prices as well as insufficient electrochemical stability make them not suitable for a wide range of practical applications.

To potentially replace precious metal-based catalysts, non-precious transition metal-based catalyst and functionalized nano carbon materials can be utilized so as to develop highly active and durable bi-functional catalysts.<sup>13, 18, 42, 47-49, 76, 86, 96-102</sup> As mentioned at the above section, metal oxides has inherent low electrical conductivity and even occurrence of severe aggregation phenomena during the battery cycling, where they are the critical downsides which limit their electrocatalytic activity toward ORR and OER. In order to resolve the serious difficulties, using highly conductive materials as substrates for the metal oxides *via* dispersion of the catalyst particles is one of the useful approaches. Among highly conductive substrate materials, functionalized carbon with heteroatom doping such as N, S, P, and B have been mainly utilized for metal oxide catalysts.<sup>103-106</sup> Especially, nitrogen-doped graphene or carbon nanotube (N-CNT) serve as the most conductive carbon materials as well as the most active ORR electrocatalysts in alkaline electrolyte.<sup>48, 79, 107</sup> Moreover, a design of the hybrid materials simultaneously improves electrical conductivity and the number of active sites is increased owing to the ability of the high surface carbon substrate to uniformly disperse the metal oxide particles while enlarging its catalytic active surface area. As a result of the combination, synergistic impacts between the metal oxides and the functionalized nano carbon materials often provide not only the higher electrochemical activity toward ORR and OER, but also the longer stability.

For instance, as an effective hybrid material for oxygen catalysis, combining non-precious transition metal oxides with active carbon nanostructures, Chen et al. have synthesized perovskite oxides supported on two different structures, nitrogen-doped carbon nanotubes

(N-CNTs) and nitrogen-doped reduced graphene oxide (N-rGO), both which have shown high electrochemical activities toward ORR and OER, comparable to state-of-art commercial Pt on carbon (Pt/C) and Ir on carbon (Ir/C), respectively.<sup>47, 48</sup> Muhler and Schuhmann et al. have suggested high-performance bi-functional composites composed of manganese oxide and cobalt oxide nanoparticles combined with nitrogen-doped carbon material. They employed high temperature pyrolysis to obtain the bi-functional electrocatalysts using unique structural and functional properties of precursor materials such as phthalocyanines.<sup>108</sup>

## **2.5 Study Goal and Objective**

Metal-air battery is a board subject and there are multiple aspects requiring improvement before commercialization can be realized. The goal of this study will focus mainly on the development of uniquely nanostructured bi-functional catalyst *via* novel methods which is highly active toward both the ORR and OER as well as greatly durable for the sake of electrically rechargeable zinc-air battery. In particular, hybrid catalysts composed of transition metal oxides and functionalized nano-carbons are greatly valuable as they offer cost competitive, and highly active and durable properties toward both ORR and OER on a single air electrode, while extremely reducing the battery cost, simplifying battery design, and even considerably increasing energy efficiency. As a result, their utilization gives rise to

great possibility of alternating precious metal-based extremely active catalysts for a wide range of commercialization in human life.

The objectives of this thesis are to report the results of a facile preparation of highly active bi-functional catalyst toward both ORR and OER and the practical utilization of the novel materials in prototype zinc-air battery. To achieve these objectives, the novel approach is employed to synthesize the hybrid bi-functional catalyst followed by detailed physical and electrochemical characterizations and performance evaluation will be presented. This work will provide insights regarding the correlation between synergistic effects, which are from the harmonious combinations of hybridizing cobalt oxide nanocrystals ( $\text{Co}_3\text{O}_4$  NCs) and nitrogen-doped carbon nanotubes (N-CNTs), and ORR/OER activities, and conclusively suggest innovative methods so as to synthesize highly active and durable electrocatalysts with bi-functionality toward the both oxygen reactions.

## **Section 3: Characterization Techniques**

This chapter discusses the physical and electrochemical characterization techniques which are utilized for the proposed research. Physical characterizations are mainly used to reveal and understand the morphology, crystal structures, oxidation states, and thermogravimetric properties of the nanomaterials developed in this study, while electrochemical characterizations are used to investigate the electrochemical performance of the developed catalysts *via* both oxygen reduction and evolution reactions necessary for rechargeable zinc-air battery operation.

### **3.1 Physical Characterization Techniques**

#### **3.1.1 Scanning Electron Microscopy**

Scanning electron microscopy (SEM) is an important characterization technique which allows high resolution inspection of the morphological information of a material in the micro and nanoscale.

SEM has been utilized extensively to study the micro- or nano-structure of the developed catalysts in this research. Basically, SEM utilizes an electron beam which is focusing on the surface of sample to elucidate its topology and morphology. Moreover, this technique is particularly useful as the electron source has an extremely small wavelength, which allows production of high resolution images of nanostructured materials. The operation principle of

SEM is based on the interaction of electron with the samples. The primary electron comes from emission source whereby the large potential difference between the emitter and the biased cathode results in the formation of a beam of electron with kinetic energy ranging from 0.2 to 40 kV. The energetic electrons passing through the microscopy column is concentrated by several sets of magnetic coil so as to achieve a spot size of 0.4 nm to 5 nm, making possible strong electron beam.<sup>109</sup> When the prepared electron beam is focused on the surface of samples, several types of electrons are either generated or reflected. The first type is secondary electron generated by the ionization effect between the initial electron beam and the samples which is happened at the very close area to the surface of the samples. The second type is backscattered electron created by the direct inelastic scattering of the incident electron by the atomic nuclei of the sample. As captured by the detector, the secondary electrons carry information related with surface topology and the backscattered electrons transfer information regarding atomic number of the sample. There is one more type of electron generated, which is auger electrons, and it can be utilized to validate the elements and the chemical states present in the sample. As a result, once the electron beam is focused on the sample by a set of electromagnetic lenses, by the interactions of the electron beam with the sample's surface, the re-obtained electron beam containing the secondary and backscattered electrons is scanned over an area in a raster fashion, and the detected electrons are converted into an electric signal and processed by a computer to produce the final image.

### **3.1.2 Transmission Electron Microscopy**

Transmission electron microscopy (TEM) is one of the essential physical characterization techniques, which allows direct visualization of the sample's morphology similar to SEM. TEM also utilizes an electron beam as the source where this technique is especially useful for in collecting lattice and surface structure information due to its high resolution capabilities. TEM has been utilized extensively so as to not only study the morphological and crystal structure with lattice information of the sample, but also perform compositional analysis with selected small areas within the sample by addition of an X-ray detector and analysis software. The operation principle of TEM is based on the interaction between the electron and the sample. The primary electron comes from an emission source whereby the large potential difference between the emitter and the biased cathode results in the formation of an electron beam with kinetic energy ranging from 100 to 400 kV. The highly energetic electrons travelling through the microscopy column is focused by several sets of magnetic coil in order to accomplish a spot size of tens of angstrom.<sup>110</sup> However, unlike in SEM which releases the electron beams on the surface of the sample and detects secondary or backscattered electrons above the sample, the electron beam penetrates the sample in TEM. The sample is usually very thin which is prepared onto a carbon-coated copper grid. As the electron beam is released from the sample, the difference in the energy of the beam provides information required for imaging process. Then, TEM detects the electron beams which are transmitted through a thin sample and then converts it to an electric signal so as to produce the final image. The selected area electron diffraction (SAED) study carried out by TEM has

advantage over the X-ray diffraction technique in that it has shorter wavelength thus able to review more reciprocal lattice point from the Ewald Sphere. Perhaps the most commonly used feature of TEM is the high resolution imaging where the resolution can reach until 0.5 nm. High resolution TEM (HR-TEM) allows the imaging of crystallographic information of the sample and the imaging in HR-TEM is implemented by interrupting the existing wave of the incident electron beams.<sup>110</sup>

### **3.1.3 X-Ray Diffraction**

X-ray diffraction (XRD) is a versatile characterization technique which allows the confirmation of crystal structure. In this study, XRD was mainly employed to research the crystal structures of the developed catalysts.

The X-rays from the source interact with the sample, where X-ray diffraction operates based in the interaction of the X-ray with the electron density of sample atoms. The wavelength of X-ray used is very small, typically in the range of 0.01-50 angstrom which allows the X-rays to interact with the sample atoms to obtain information about their long range orders. The x-ray source is swept over a range of angles and the diffracted x-rays at specific angles are collected and processed by the detector. As the angle between the X-ray and the sample changes, the diffraction event will occur only at certain angles corresponding to specific crystal planes producing the diffraction patterns at the angles. The angle of diffraction is related to the specific crystal orientation of the sample by Bragg's law as shown by Equation

below,<sup>111</sup>

$$2d \sin \theta = n\lambda$$

where  $n$ ,  $\lambda$ ,  $d$ , and  $\theta$  represent the order of the spectrum (any integer), the wavelength of the X-rays, the spacing between diffracting planes, and the incident angle, respectively. The diffraction pattern at specific angles obtained by XRD can be compared to the theoretical diffraction pattern calculated by the crystal planes to help identify the material. Having said this, XRD patterns cannot be produced by amorphous materials as they do not have ordered crystal planes that interact with X-rays to produce diffracted patterns. In this research, XRD is used to identify the developed catalysts and confirm their crystal structures.

### **3.1.4 X-Ray Photoelectron Spectroscopy**

X-ray photoelectron spectroscopy (XPS), also known as electron spectroscopy for chemical analysis (ESCA), is a surface elemental characterization technique allowing investigation of elemental composition, surface bonding configuration, valence and electronic states of a sample. In this study, the XPS was used to identify and quantify the elements in the developed catalysts as well as their electronic states. Especially, among the different elements in the N-CNT analyzed by a high resolution XPS (HR-XPS) spectrum, various nitrogen signals are of special interest. HR-XPS focusing on collecting fine details of the N

1s spectrum was employed to confirm a relationship between the surface nitrogen groups and ORR activity. Deconvolution of the HR-XPS signal allows the identification of different chemical state of N atom on the surface of N-CNT.

XPS technique works by irradiating X-ray on the sample to induce emission of electrons by photoelectric effect. The operating principle of XPS is based on the interaction of incident X-ray photon and the sample electrons in ultrahigh vacuum conditions. In XPS, unlike XRD, the emitted radiation is only from the 1-10 nm of the sample surface making this technique very surface sensitive. As the X-ray interacts with the samples, the energy transfer from X-ray photons to the electron occupying different energy state is showed in the equation below.<sup>112</sup>

$$E_{\text{photon}} = E_{\text{binding}} + E_{\text{kinetic}} + \varphi$$

From the equation,  $E_{\text{photon}}$  represent the energy of incident X-ray;  $E_{\text{binding}}$  represents the binding energy of the electron at different energy state, for example 1s, 2s and 2p;  $E_{\text{kinetic}}$  represent the kinetic energy of the excited electron and  $\varphi$  represent the work function of the spectrometer. By counting the number of electron at different binding energy, an energy spectrum specific to different elements can be precisely produced *via* a pattern with intensity versus binding energy. The specific binding energy of the electron acts as the blue print for identifying the composition of the sample with the intensity corresponding to the quantity of elements. Meanwhile, HR-XPS can be achieved using additional monochromator in the XPS

so as to achieve X-ray source of reduced energy width dispersion and improve chemical state selectivity by narrowing spectral peaks. Additionally, lower spectral background and the elimination of unwanted x-rays from satellites and anode impurities can also be accomplished.<sup>112, 113</sup> The detection limit for the XPS is usually at parts per thousand ranges. However, high resolution can be achieved under extended signal collection time and higher surface concentration of species of interest.

### **3.1.5 Brunauer-Emmett-Teller Analysis**

Brunauer-Emmett-Teller (BET) analysis, which is based on Langmuir isotherm theory for monolayer adsorption, was developed in 1938.<sup>114</sup> BET analysis is useful for obtaining structural information of the catalyst and its support, especially when the material is porous, by utilizing the physical adsorption of gas molecules onto surface of a solid material so as to measure the specific surface area, average pore size, and pore size distribution of the sample. In this study, BET analysis was utilized to measure the specific surface areas and pore size distributions in the developed catalysts.

The theory works based on a number of assumptions which are from the Langmuir isotherm theory; (1) adsorption occurs only on well-defined sites of the sample, (2) there is no interaction between the adsorption layers, (3) the adsorption occurs in a monolayer and each layers is treated as a Langmuir monolayer, and (4) the number of layers tends to go infinity at the saturation pressure. Based on the above assumptions, the resulting BET equation is derived as shown below.<sup>114</sup>

$$\frac{1}{V\left[\left(\frac{P_0}{P}\right) - 1\right]} = \frac{1}{V_m C} + \frac{C - 1}{V_m C} \left(\frac{P_0}{P}\right)$$

In the above equation, V is volume of gas adsorbed (cm<sup>3</sup>), P is gas pressure, P<sub>0</sub> is equilibrium vapor pressure at the test temperature, V<sub>m</sub> is volume of adsorbed gas in monolayer (cm<sup>3</sup>), and C is BET constant. Typically, the V and the P/P<sub>0</sub> are gauged by using nitrogen gas at 77 K. By adjusting the pressure, the equation can be modified and linearly plotted. An intercept and a slope from the plots provides volume of adsorbed gas in monolayer (V<sub>m</sub>), then V<sub>m</sub> is utilized so as to calculate the specific surface area as in the following equation.

$$S = \frac{V_m N_{AV} A_{ab}}{V_i M}$$

In the equation, S is specific surface area (m<sup>2</sup>g<sup>-1</sup>), N<sub>AV</sub> is Avogadro's number (6.02\*10<sup>23</sup> mol<sup>-1</sup>), A<sub>ab</sub> is area of single adsorbate molecule using the cross-sectional area (m<sup>2</sup>), V<sub>i</sub> is volume of one mole of ideal gas (L), and M is mass of sample (g).

### 3.1.6 Thermogravimetric Analysis

Thermogravimetric analysis is used to study the weight change of sample as a function of temperature. In this study, TGA was used to estimate the weight of metal oxides after removing any carbonaceous material via high temperature.

The TGA experiment is performed by heating the sample of known mass in a platinum pan in either N<sub>2</sub> or air environment. The temperature set points, ramp rate and dwell time can be controlled by the software. In a typical experiment, the developed catalysts were heated up to 800 °C in air environment at a ramp rate of 10 °C/min.

## **3.2 Electrochemical Characterization Techniques**

In addition to the above physicochemical analysis, it is also required to verify the functionalities and evaluate the performances of the synthesized catalysts by using electrochemical measurements. The following two sections explain about the electrochemical measurements in detail including half-cell testing via rotating disk electrode (RDE) and practical rechargeable zinc-air battery cycling test.

### **3.2.1 Half-Cell Testing: Cyclic Voltammetry**

Cyclic voltammetry (CV) is potentiodynamic electrochemical measurement technique, where it is utilized so as to investigate reduction and oxidation characteristics of the developed catalysts. During the CV process, a potential of working electrode is linearly swept forward and backward at a certain scan rate within a desired potential range. By sweeping the potential, a current is measured and obtained showing a plot of the current versus the potential, which is called a cyclic voltammogram as presented in **Figure 8**, where

this is a unique redox property of the prepared catalyst. The electrochemical characteristics are elucidated by exploring the correlation between the potential and the recorded current in the cyclic voltammogram.<sup>115</sup>

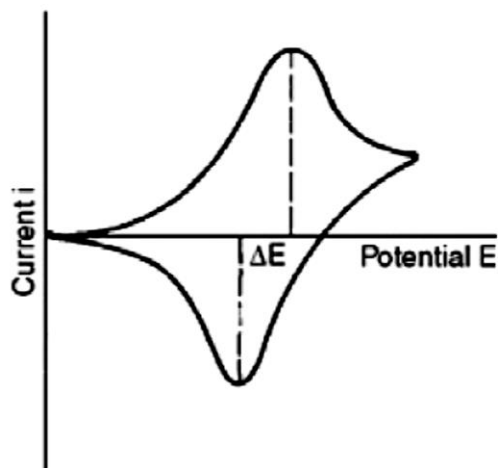


**Figure 8. Cyclic voltammogram of a reversible diffusion-controlled process. Reprinted with permission.<sup>23</sup> Copyright 2001, McGraw Hill.**

In this study, the cyclic voltammetry technique is utilized so as to confirm oxygen reduction reaction (ORR) and oxygen evolution reaction (OER) activities of the developed catalysts in oxygen-saturated and nitrogen-saturated electrolyte, respectively. In addition, CV is also carried out in nitrogen-saturated inert electrolyte for the sake of verification of possible existence of undesired reactions where they are applied to the obtained ORR/OER cyclic voltammograms.

### 3.2.2 Half-Cell Testing: Rotating Disc Electrode

The half-cell electrochemical testing via rotating disk electrode (RDE) measurement is a fundamental but very useful technique which is widely utilized not only for electrochemical analysis of redox reaction mechanisms, but also for rapid evaluations of the developed catalysts.<sup>115</sup>

As one of the three main components of the half-cell testing, the RDE is simply designated as a hydrodynamic working electrode. Typically, RDE is composed of a glassy carbon disk electrode embedded in an insulating Teflon outer layer, where the developed catalysts are solely coated on the smooth surface of glassy carbon. The catalyst is prepared into an ink phase solution where the catalyst is dispersed in a mixture of binder solution such as Nafion and ethanol. The catalyst ink is then coated on the surface of glassy carbon of the RDE with a desired amount of catalyst loading.

In order to be rotated during the half-cell test, the RDE is connected to a vertical rod which makes a rotation at various speeds by a rotation speed controller. The rotation generates a flow of electrolyte, which is triggered by convection, and it allows mass transport of active species such as hydroxide ions. A series of experimental data is obtained *via* a variety of rotating speeds of the RDE which are systemically managed, where they are required for the sake of analyzing electrochemical catalytic reactions at a determined speed and further investigating correlations of the data obtained at the different rotation speeds.

In addition to the RDE serving as a working electrode in the electrochemical half-cell system, the half-cell system contains two more components which are reference electrode

and counter electrode. The reference electrode is utilized to standardize the other conditions of experiment by giving constant potential. Widely used reference electrodes include: standard hydrogen electrode (SHE), saturated calomel electrode (SCE), and silver-silver electrode (Ag/AgCl).<sup>116</sup> As the last component of the half-cell testing, the counter electrode, along with the working electrode, offers a circuit to the cell and the potential of the counter electrode is not measured but adjusted so as to balance the reaction which is occurring at the working electrode. This arrangement allows the potential of the working electrode to be measured against the reference electrode.<sup>116</sup>

**Figure 9** presents a typical setup of half-cell test composed of the three main components. The aforementioned three electrodes are all allocated in the three-neck flask filled by the electrolyte, where it is purged with either oxygen or nitrogen depending on the experimental purpose of the voltammetry.

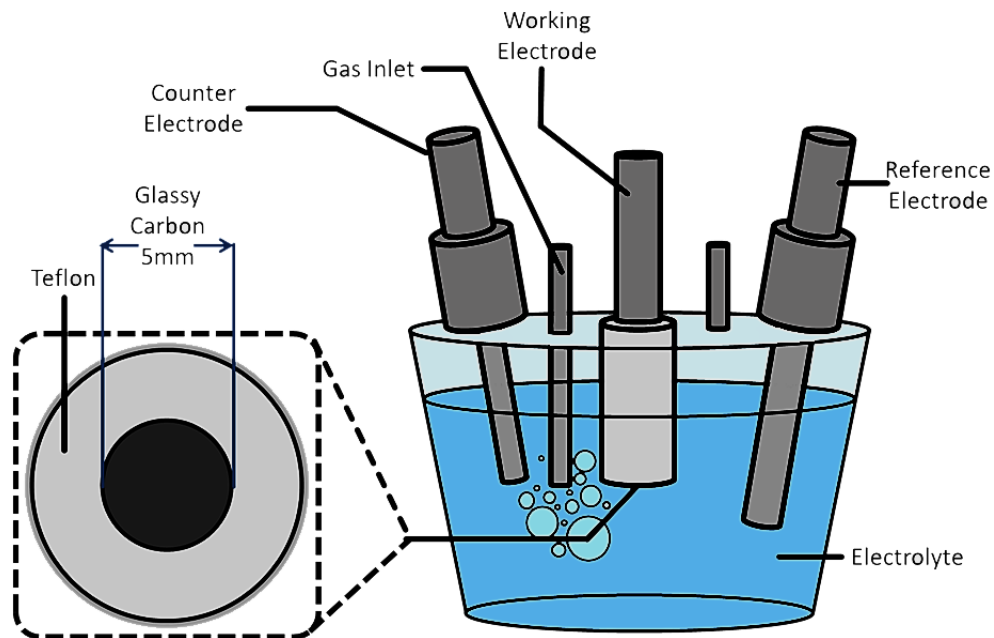


**Figure 9. Typical setup of three-electrode half-cell testing equipment**

In this study, a rotating disc electrode (RDE) half-cell equipment was employed to investigate both oxygen reduction reaction (ORR) and oxygen evolution reaction (OER) catalytic activity of the prepared materials. Conventional three-electrode system consisting of working electrode, counter electrode and reference electrode was used. As described above, the catalyst-coated glassy carbon disk electrode and a platinum wire were used as working and counter electrodes, respectively, while a saturated calomel electrode (SCE) was employed as the reference electrode. 0.1 M KOH solution was used as an aqueous electrolyte. To obtain an oxygen or nitrogen saturated electrolyte, the oxygen or nitrogen gas was purged into the KOH solution for 30 minutes before the evaluations while continuing

bubbling during the tests. In order to prepare a catalyst coated working electrode, glassy carbon electrode (Diameter: 5mm with surface area: 0.196 cm<sup>2</sup>) was employed. It was first polished by using alumina powder (size: 0.3 μm and 0.05 μm), and then the electrode was directly ultra-sonicated in deionized water for a short time then dried with nitrogen gas stream. For preparing sample ink, 4 mg of the catalyst was put into 1 mL of ethanol pre-treated by Nafion solution (0.05 wt. %) and the mixture was ultra-sonicated for 2 hours to obtain a homogenously mixed ink. 20 μL of the as-prepared dispersion was dropped onto the circle-shaped glassy carbon and dried under ambient conditions (catalyst loading: 0.4 mg cm<sup>-2</sup>).

Electrochemical activities of the materials were studied by cyclic voltammetry (CV) for OER and linear sweep voltammetry (LSV) for ORR, which were performed using CHI Electrochemical Station (Model 760D) and rotation speed controller (Pine Instrument Co., AFCBP-1). Catalytic activity toward the ORR was recorded from 0.1 to -1.0 V vs. SCE at a scan rate of 10 mV s<sup>-1</sup> with oxygen saturated electrolyte under a series of rotating electrode speeds (400, 900, 1600 and 2500 rpm). The ORR polarization curves were corrected by subtracting background currents by the same test procedures obtained with nitrogen saturated electrolyte in order to remove capacitive contributions during the tests of ORR activities. The electrochemical performance of the OER was evaluated from 0 to 1 V vs. SCE at a scan rate of 10 mV s<sup>-1</sup> (50 mV s<sup>-1</sup> for the OER cycling as a durability test) with nitrogen saturated electrolyte with 900 rpm in order to remove surface oxygen bubbles generated during the OER test. The precious metal based bi-functional active material

consisting of both platinum carbon (Pt/C, 28.8 wt. % Pt), as one of the best ORR electrocatalyst, and iridium carbon (Ir/C, 20 wt. % Ir), as one of the best OER catalyst, was employed as the reference material.

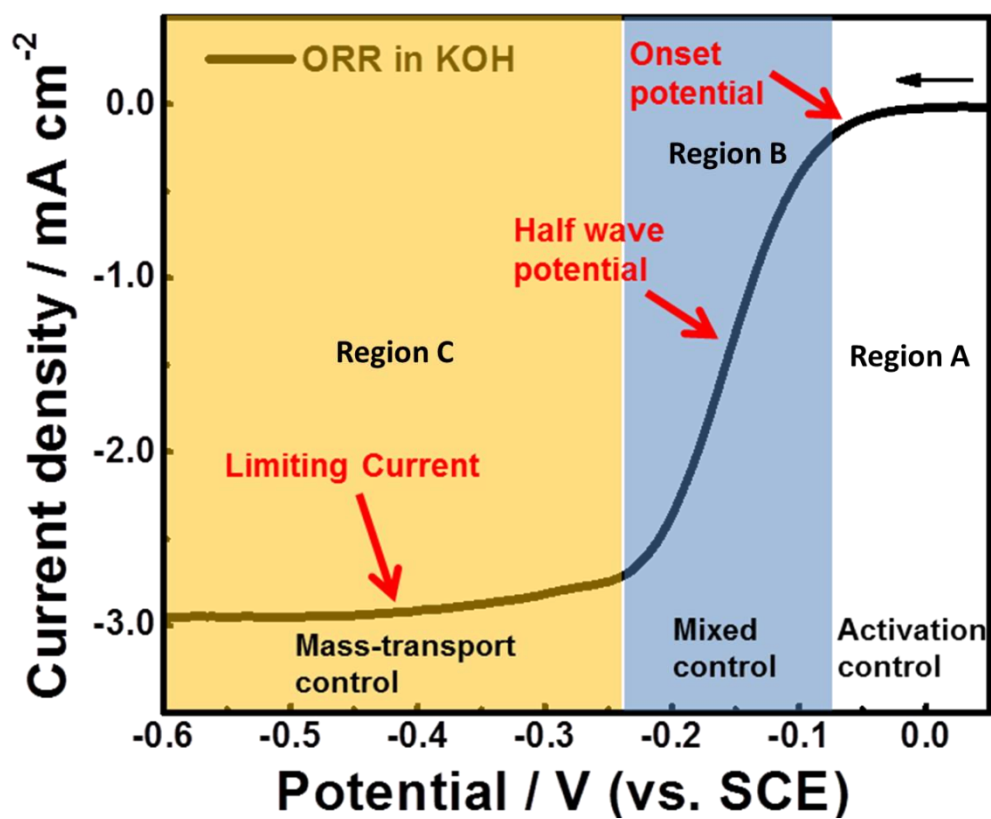


Figure 10. Typical ORR polarization curve in KOH electrolyte

Typical ORR polarization curve is shown in **Figure 10**. Three regions are defined on the polarization curve, Region A corresponds to the initial step of the electrochemical reaction containing the on-set potential which is firstly occurring by a desired reaction, where it is solely managed by the kinetics of the reaction. Better the ORR activity of a catalyst is, the

less the kinetically controlled region is. Region B corresponds to the mixed control region where the kinetic controlled part and a mass transport limiting part are combined and the half-wave potential is included in the mixed region. The slope of the pseudo-linear region would depend on the catalytic reaction rate of the developed catalyst. Region C corresponds to the mass transport limiting region including limiting current where the mass transport of active species is maximized, but the reaction kinetics is much faster than the rate of mass transport. Thus, the reaction is not ideally continued, but has a maximum current limited by the rate of mass transport at a certain rotation speed, where the mass transport limiting current depends on the rotation speed of the catalyst-coated RDE.

From the ORR polarization curves obtained at the different rotation speeds, it is possible to study the reaction kinetics and mechanisms of the developed catalyst via a Koutecky-Levich (K-L) equation which is as following:<sup>117</sup>

$$\frac{1}{j} = \frac{1}{j_K} + \frac{1}{j_{Lev}} = \frac{1}{j_K} + \frac{1}{B\omega^{0.5}}$$

$$j_K = nFkC_{O_2} \text{ (kinetic current)}$$

$$B = 0.62nFD_{O_2}^{2/3} C_{O_2} \nu^{-1/6} \text{ (Mass transport limiting current constant)}$$

In the above equations, the limiting current ( $j$ ) is related to kinetic current ( $j_K$ ) and Levich current ( $j_{Lev}$ ), where  $j$  is the observed current.  $n$  is the number of electrons transferred per  $O_2$  molecule;  $F$  is the Faraday constant ( $96,485 \text{ C mol}^{-1}$ );  $C_{O_2}$  is the saturated concentration

of O<sub>2</sub> in the electrolyte ( $1.1 \times 10^{-6} \text{ mol cm}^{-3}$ );  $D_{O_2}$  is the diffusion coefficient of O<sub>2</sub> ( $1.9 \times 10^{-5} \text{ cm}^2 \text{ s}^{-1}$ );  $\nu$  is the kinematic viscosity of the solution ( $0.01 \text{ cm}^2 \text{ s}^{-1}$ ); and  $\omega$  is the rotation rate of RDE. The linear fitting of K-L plots between  $j^{-1}$  vs.  $\omega^{0.5}$  is based on the Koutecky-Levich equation as shown in **Figure 11**.<sup>97 97 97 97 97 97</sup>

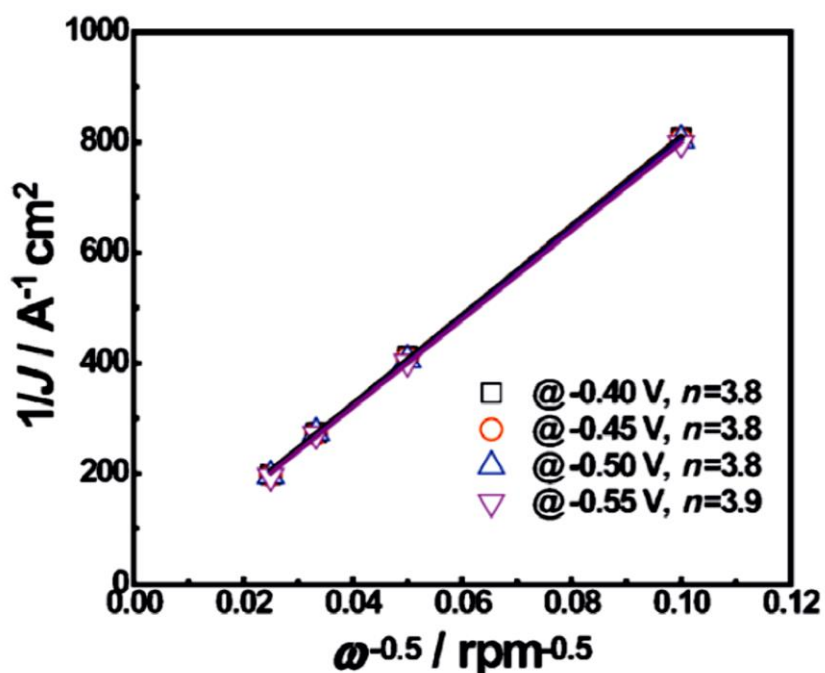


**Figure 11.** Linear fitting of K-L plots ( $j^{-1}$  vs.  $\omega^{0.5}$ ) based on the Koutecky-Levich equation at various voltages (vs. SCE). Reprinted with permission.<sup>46</sup> Copyright 2015, Wiley-VCH.

K-L plots are mainly used to determine the number of electrons transferred at the surface of the catalyst during ORR. By the linear fitting of the K-L plots, the transferred electrons

during ORR can be calculated and an average numbers of the electrons also can be obtained at different working electrode potentials. Furthermore, the Y-intercept of the K-L plot represents the kinetic current ( $j_K$ ) and the slope of the K-L plot directly means the number of electrons transferred. The number of electrons transferred has an ideal number, which is four, where the four electrons transferred during ORR means that ORR is perfectly occurring and only water ( $H_2O$ ) molecules are made during the catalytic reaction without creation of hydrogen peroxide ( $H_2O_2$ ) molecules. Typically, the number of electrons transferred is much less than the four when using non-precious catalysts. Thus, developing highly active non-precious catalysts which have the number of electrons transferred close to four is greatly important for the more efficient reactions.

### **3.2.3 Zinc-Air Single Cell testing: Fabrication and Performance Evaluations**

In order to consolidate the electrochemical results from the above half-cell testing, a practical use of the developed electrochemical catalyst was investigated by using a rechargeable zinc-air battery (ZAB) prototype, which consists of not only air electrode and zinc plate as a cathode and an anode, respectively, but also electrolyte and separator as shown in **Figure 12**.

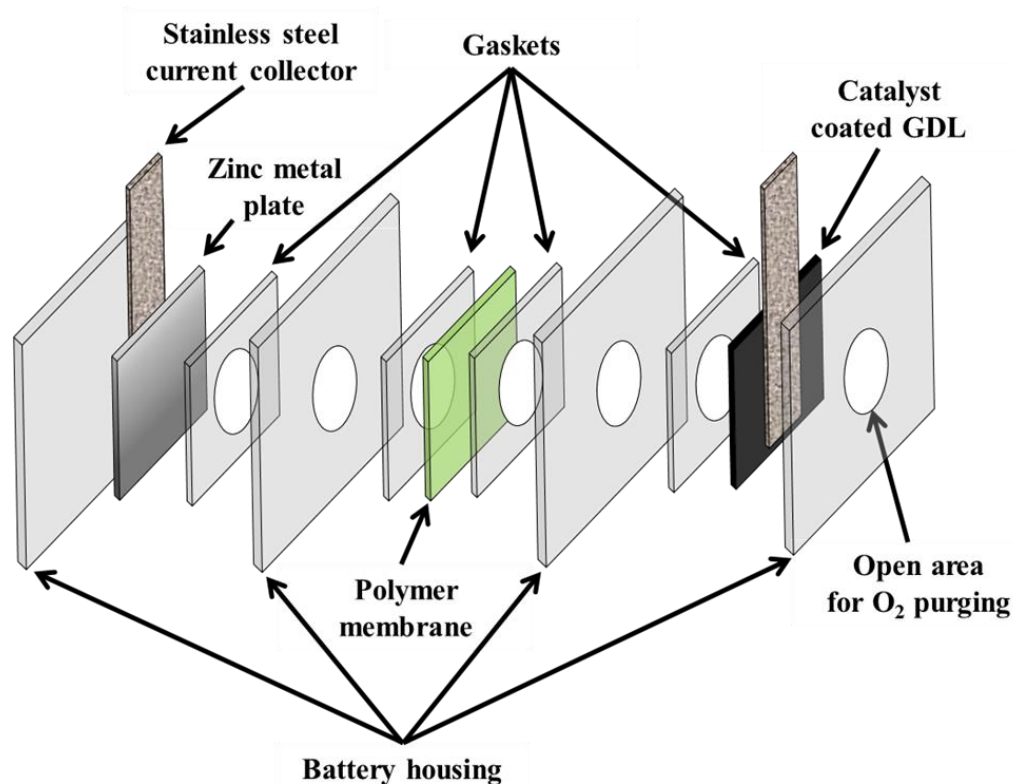


**Figure 12. Schematic diagram of rechargeable zinc air prototype**

The air electrode was first prepared using a gas diffusion electrode (Ion Power Inc., SGL Carbon 10 BB, 2 cm by 2 cm) where catalyst was spray-coated using air brush with an air electrode active area of  $0.785 \text{ cm}^2$ . Briefly, the catalyst materials were dispersed in a Nafion-containing (5 wt. %) isopropanol mixture with a catalyst concentration of  $4 \text{ mg mL}^{-1}$ . This mixture was then ultra-sonicated for 1 hour under ambient temperature so as to obtain a well-dispersed ink solution. Then, it was air brush sprayed onto the gas diffusion electrode (GDE) for subsequent testing (average catalyst/binder loading:  $1 \text{ mg cm}^{-2}$ ). A zinc plate (OnlineMetals, Zinc Sheet EN 988) was polished by a fine sand paper for the sake of clean

surface with better reactivity. A microporous 25  $\mu\text{m}$  polypropylene membrane (Celgard 5550) and 6.0 M KOH with 0.2 M zinc acetate solution were employed as the separator and the electrolyte, respectively.

Galvanodynamic discharge and charge experiments and electrochemical impedance spectroscopy (EIS) tests were carried out with a multichannel potentiostat (Princeton Applied Research, VersaSTAT MC). The galvanodynamic technique, which enables study of discharge and charge behaviours of the catalyst, is conducted with a wide range of current change (current density: 0 ~ 60  $\text{mA cm}^{-2}$ ). During discharge, the applied current decreases from 0 A up to a desired value at a fixed current rate ( $\text{mA/s}$ ), and simultaneously the battery potential decreases from its open circuit voltage (OCV). During charge, on the other hand, the current increases from 0 A up to a desired value at the same current rate and the battery potential increases from the OCV. The polarization curves during the discharge and charge processes are obtained from this useful technique and utilized for verifying overpotentials. The overpotential is related to the catalytic oxygen reactions (ORR and OER) and resistances of the developed catalysts.

Electrochemical impedance spectroscopy (EIS) tests is implemented to investigate the overall battery resistance containing internal resistance, solid-electrolyte interface resistance, and charge transfer resistance during the battery operation. In this study, the EIS tests are carried out by a fixed potential at 0.8 V and the frequency was changed from 100,000 to 0 Hz. The obtained signals are expressed into a Nyquist plot and then the plot is fitted with an

equivalent circuit composed of relevant circuit elements corresponding to the aforementioned resistances during the battery operation.

In addition to these above the two useful techniques, galvanostatic cycling tests is also conducted by a cycling tester (BTSDA). The main purpose of the cycling tests is to scrutinize both activity and durability of the developed catalysts, which are directly associated with overpotential between charge and discharge voltages and the continuous cycle life without severe enlargement of the overpotential, respectively. The battery potential profiles during the cycling tests are obtained by applying repeated discharge/charge processes with a fixed current and a fixed amount of cycle time. The experimental conditions can be adjusted according to their own purpose applying either pulse cycling or extended cycling, where the pulse cycling technique is to evaluate the battery's rechargeability by interchanging the polarity in short intervals and the extended cycling is to measure cycling capabilities of the battery and concurrently estimate the possibility in practical use of the developed catalyst in the zinc-air battery. The activity of the catalyst is determined by the overpotential between the discharge potential and the charge potential, where typically a low overpotential signifies high activity toward oxygen reactions. Also, the durability of the catalyst is determined by the degree of retention of the battery potential over a number of cycles

In this work, the cycling was performed with 10 minutes cycles (5 minutes discharge and 5 minutes charge) and a high current density of  $20 \text{ mA cm}^{-2}$  for the short cycling test. For a

long cycle performance measurements in relatively harsh conditions, long term cycling test was conducted, where one cycle was 4 hours (2 hours each for discharge and charge) at the same current density ( $20 \text{ mA cm}^{-2}$ ). The galvanodynamic discharge and charge experiments and electrochemical impedance spectroscopy (EIS) tests were conducted before and after the certain number of galvanostatic cycles so as to evaluate the change in performance such as the activity and durability of the developed catalysts.

## **Section 4: Bi-functional Electrocatalysts for Rechargeable Air-Electrode**

### **4.1 Synergistic effect of hybridizing Spinel Cobalt Oxide with Nitrogen-doped Carbon Nanotubes**

Reproduced in adapted form from “Highly Active and Durable Nanocrystal-Decorated Bifunctional Electrocatalyst for Rechargeable Zinc-Air Batteries” Moon Gyu Park†, Dong Un Lee†, Hey Woong Park, Min Ho Seo, Xiaolei Wang, and Zhongwei Chen, published in *ChemSusChem*<sup>118</sup>

#### **4.1.1 Introduction and Motivation**

With ever-increasing concerns over depletion of fossil fuel, the development of next generation energy conversion and storage systems has become the main focus for improving global sustainability. Since natural sources of energy are non-renewable, systems that generate energy using these sources are likely to become obsolete, and will eventually be replaced by advanced rechargeable energy systems based on renewable energy sources. Among a variety of rechargeable energy systems, lithium ion batteries (LIBs) is one of the most widely used system due to its advantages such as high energy efficiency, power density and good cycle stability.<sup>18</sup> However, limitations of LIBs for further development are their relatively low specific energy density, high costs of active materials as well as safety concerns particularly for electric vehicle (EV) and hybrid electric vehicle (HEV) applications.<sup>13, 18, 77</sup> On the other hand, advanced battery systems such as metal-air batteries

(MABs), which utilize freely available oxygen in the atmospheric air, have recently gained much attention due to their extremely high energy density, environmental benignity, low cost and safe operation.<sup>18,77</sup> By utilizing oxygen from the atmosphere, MABs do not require fuel reservoirs allowing for lightweight and compact battery design and fabrication, which are highly desirable for extending the driving range of EVs and HEVs. Among MABs, lithium air batteries (LABs) and zinc air batteries (ZABs) are rigorously investigated which have very high theoretical energy densities (11,680 and 1,084 Wh kg<sup>-1</sup>, respectively).<sup>8, 18, 77</sup> However, ZABs in particular have attracted tremendous attentions owing to safe operations, easy handling and abundant zinc source. ZABs also are very attractive for EV applications, in which safe operation is important, thanks to their nonexplosive and non-flammable properties of components.<sup>13</sup> Despite the aforementioned advantages, a few technical challenges must be addressed before wide-spread commercialization of ZABs due to their limited practical energy density and insufficient cycle life as well as some technical challenges. Among many components of MABs, the development of air electrode is one of the most critical areas especially to make it efficiently rechargeable mainly due to the sluggish kinetics of oxygen electrochemical reactions involved during the battery operation.<sup>8, 10, 18, 79, 97, 119, 120</sup> To overcome the above challenges, oxygen catalysts which can improve the rate of the oxygen reactions as well as decrease overpotentials during battery operation are necessary, where they must have bi-functional activity for both ORR and OER. In addition to the high activities, electrochemical stability is also a highly critical requirement for realization of electrically rechargeable zinc-air battery. Thus, a development of a very

novel bi-functional catalyst with a facile and unique synthetic method has been significantly required.

In this work, accordingly, a simple synthetic strategy for effectively producing hybrid catalysts is introduced based on hydrophobic attraction between cobalt oxide nanocrystals ( $\text{Co}_3\text{O}_4$  NC) synthesized by surfactant-assisted interfacial self-assembly and graphitic walls of nitrogen-doped carbon nanotubes (N-CNT). This hybrid has been utilized in a practical rechargeable zinc-air single-cell battery prototype to show its efficient bi-functional catalytic property (**Figure 13**).<sup>121</sup> This novel hybrid electrode material design is particularly interesting due to its simple preparation procedure involving electrostatic interaction as the driving force without the use of high temperature or pressure. The hybrid catalyst is synthesized by a facile interfacial reaction where  $\text{Co}_3\text{O}_4$  NC are formed and become encapsulated by surfactant self-assembly, which are then attached to the hydrophobic surfaces of N-CNT. The final hybrid is therefore composed of  $\text{Co}_3\text{O}_4$  NC strongly bound by hydrophobic attraction and uniformly decorated on the surface of N-CNT, resulting in enhanced surface area with highly exposed catalytic active sites. To confirm excellent electrochemical activities of  $\text{Co}_3\text{O}_4$  NC/N-CNT hybrid as an effective bi-functional electrode material, both half-cell and single-cell tests using rechargeable zinc air battery prototype has been demonstrated.

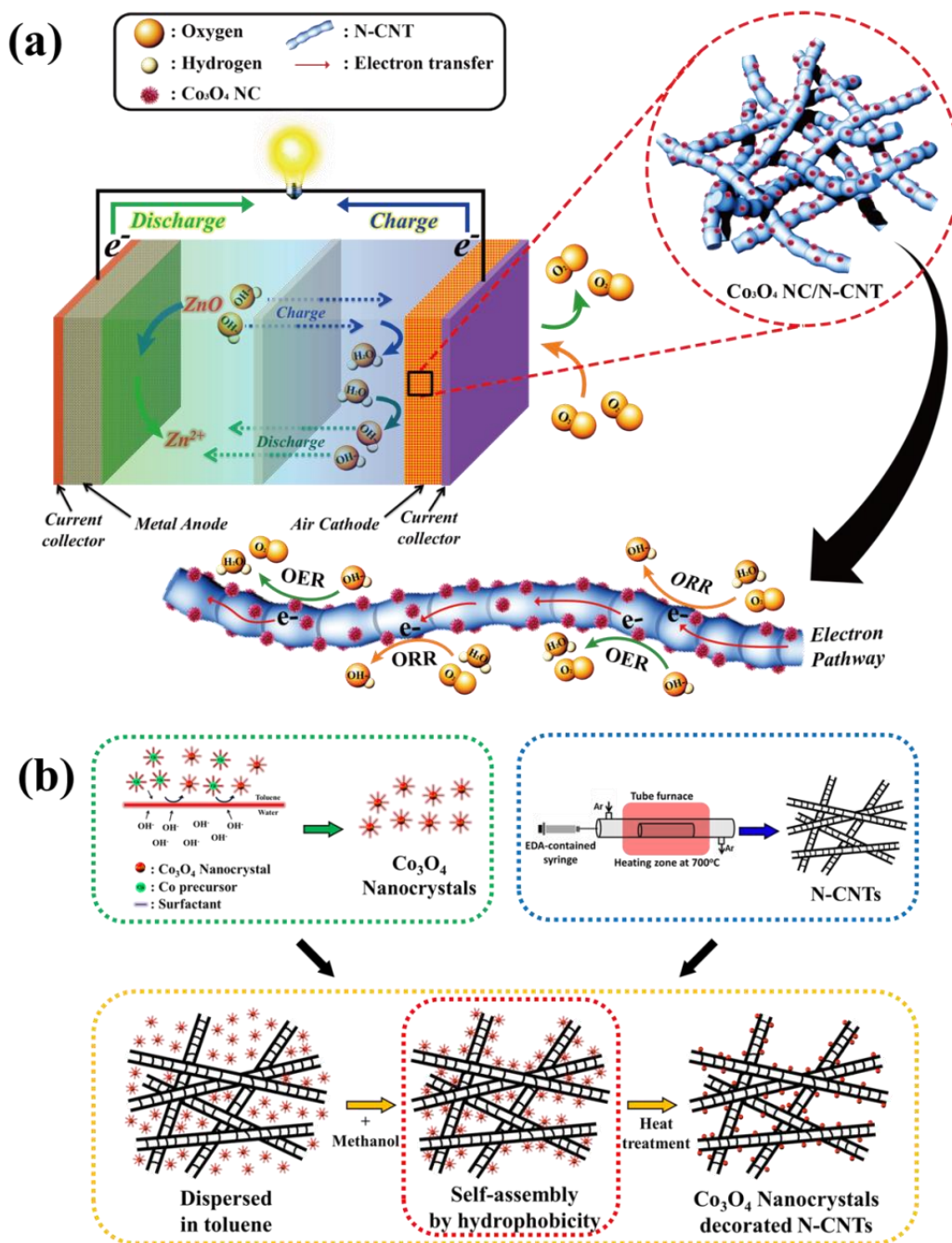


Figure 13. (a) Schematic illustration of the charge and discharge processes of zinc air battery at  $\text{Co}_3\text{O}_4$  NC/N-CNT coated GDL for bi-functional electrocatalysis for ORR and OER, (b) Diagram of processes of synthesis for cobalt oxide nanocrystals decorated nitrogen-doped CNT hybrid material by hydrophobic power.

## **4.1.2 Experimental Methods**

### **Chemicals and materials**

All of chemicals were purchased from Sigma-Aldrich and used without further processing. Cobalt nitrate hexahydrate, sodium stearate, methanol, toluene, dodecylamine and tert-butylamine were employed for synthesis of cobalt oxide nanocrystals and ethylenediamine and ferrocene were utilized for nitrogen-doped carbon nanotubes, and sulfuric acid was used for etching of nitrogen-doped carbon nanotubes.

### **Catalyst preparation**

**Synthesis of nitrogen-doped carbon nanotubes:** Nitrogen-doped carbon nanotubes (N-CNTs) was prepared by a simple injection chemical vapor deposition (CVD) method as described in our previous work.<sup>79</sup> Briefly, ethylenediamine (EDA) and ferrocene were employed as carbon source and catalyst, respectively. First, EDA and ferrocene were dissolved in ethanol by ultrasonication for 2 hours to obtain a homogeneous dispersion. Then, a tube furnace was set up with a large quartz tube, a syringe pump and a syringe, which was prepared with a 2 mL of EDA solution. The furnace was heated up to 700 °C at which point the syringe pump was turned on to begin injecting the precursor solution for 40 minutes with a flow rate of 0.05 mL min<sup>-1</sup>. Once the injection was finished, the pump was turned off and the furnace was cooled down to room temperature after heating at 700 °C for total of 2 hours. N-CNT was obtained by collecting black powder out of the quartz tube. N-

CNT was then acid-treated in 0.5 M sulfuric acid ( $\text{H}_2\text{SO}_4$ ) solution to remove impurities including iron particles. After acid etching, N-CNT were washed and filtered using DDI water and dried at 60 °C.

**Synthesis of cobalt oxide nanocrystals:** Cobalt oxide nanocrystals ( $\text{Co}_3\text{O}_4$  NCs) were made by a simple two-phase hydrothermal synthesis.<sup>122, 123</sup> Cobalt stearate ( $\text{Co}(\text{SA})_2$ ), which was used as a precursor, was first prepared for synthesis of  $\text{Co}_3\text{O}_4$  NC. In a typical synthesis, an oil phase mixture of toluene (15 mL), dodecylamine (1.0 g) and  $\text{Co}(\text{SA})_2$  (0.15 g) in a vial was heated at 90 °C until the solution become optically clear. Then the solution was cooled to room temperature and loaded into a 50 mL Teflon liner. De-ionized water (15 mL) and tert-butylamine (150  $\mu\text{L}$ ) were mixed to prepare a water phase solution, which was added in the 50 mL Teflon liner before addition of the oil phase solution. Next, two phase solution was heated in the autoclave without stirring at 180 °C for 5 hours. After the autoclave reaction was finished and cooled down to room temperature, the solution containing  $\text{Co}_3\text{O}_4$  NC was extracted from the Teflon liner into a test tube and mixed with methanol (30 mL) to induce precipitation of cobalt oxide nanocrystals. Finally, it was separated by the centrifugation and washing with methanol solution and stored in a toluene solution, which was utilized as a re-dispersion agent for  $\text{Co}_3\text{O}_4$  NCs due to its hydrophobic properties.

**Preparation of cobalt oxide nanocrystals-decorated on nitrogen-doped carbon nanotubes hybrid material (Co<sub>3</sub>O<sub>4</sub> NC/N-CNT):** Simple self-assembly induced synthesis was employed to obtain the hybrid catalyst.<sup>124</sup> As-prepared N-CNTs was first dispersed into the Co<sub>3</sub>O<sub>4</sub> NC solution under ultra-sonication for 2 hours. Then methanol was added into the mixture solution which created a strong hydrophobic interaction between the two components thereby self-assembling into Co<sub>3</sub>O<sub>4</sub> NC/N-CNT hybrid. The precipitated composite was separated by vacuum filtration and dried completely at 50 °C. Finally, the dried composite was heat treated at 450 °C for 2 hours using argon gas in order to obtain strong coupling between Co<sub>3</sub>O<sub>4</sub> NCs and N-CNTs with eliminating remaining surfactants between the two components. Co<sub>3</sub>O<sub>4</sub> NC/VC employed as a reference material was prepared using vulcan carbon (Vulcan XC-72) instead of the N-CNTs from the same synthesis. A schematic clearly illustrates the above overall synthesis of Co<sub>3</sub>O<sub>4</sub> NCs and N-CNTs as well as Co<sub>3</sub>O<sub>4</sub> NC/N-CNT (**Figure 13**).

### **Materials characterization**

For chemical and physical characterizations of the prepared materials a variety of techniques were employed. Scanning electron microscopy (SEM) (LEO FESEM 1530) and transmission electron microscopy (TEM) (JEOL 2010F) images were obtained for investigating the surface structure and the morphology of the prepared materials. Furthermore, high-resolution TEM (HR-TEM), selected area electron diffraction (SAED),

Scanning transmission electron microscopy (STEM) and color mapping based on energy-dispersive X-ray spectroscopy (EDX) results were employed to identify the nanocrystals as spinel cobalt oxide and to study their crystallinity in Co<sub>3</sub>O<sub>4</sub> NC/N-CNT. X-ray diffraction (XRD) (Bruker AXS D8 Advance) was utilized to confirm the spinel crystal structure of cobalt oxide nanocrystals in Co<sub>3</sub>O<sub>4</sub> NC/N-CNT, and X-ray photoelectron spectroscopy (XPS) (Thermal Scientific K-Alpha XPS spectrometer) was implemented not only to verify surface atomic composition of the developed material, but also to quantify different configurations of nitrogen species. Thermal gravimetric analysis (TGA) was carried out to elucidate the amount of Co<sub>3</sub>O<sub>4</sub> NC in the hybrid.

#### 4.1.3 Results and Discussion

**Figure 14** shows transmission electron microscopy (TEM) image and X-ray diffraction (XRD) pattern of cobalt oxide nanocrystals (Co<sub>3</sub>O<sub>4</sub> NC), and scanning electron microscopy (SEM) and TEM images of as-synthesized nitrogen-doped carbon nanotubes (N-CNT). The TEM image of Co<sub>3</sub>O<sub>4</sub> NC clearly shows cube-shaped nanocrystals with an average size of 5 nm with a good particle size uniformity (**Figure 14a**). The XRD pattern of Co<sub>3</sub>O<sub>4</sub> NC is indeed indicative of cubic spinel crystal structure consistent with that of typical cobalt oxide nanoparticles (JCPDS no. 43–1003) (**Figure 14b**).<sup>96, 97, 123</sup> The noise in the XRD pattern is due to very small dimensions of Co<sub>3</sub>O<sub>4</sub> NC, however, the main peaks of spinel Co<sub>3</sub>O<sub>4</sub> such as (220), (331) and (511) can be still observed. The SEM image of N-CNT reveals uniformly

grown tubular structure with smooth outer surface having average diameter of ~50 nm and length of several micrometers (**Figure 14c**). The TEM image of N-CNT supports the observations from the SEM image as bamboo-like structures are clearly visible which are attributed to defects at six-membered carbon rings in CNTs (**Figure 14d**), which is generated by the five- and seven-membered ring construction owing to the nitrogen dopants in CNT. <sup>125-128</sup>

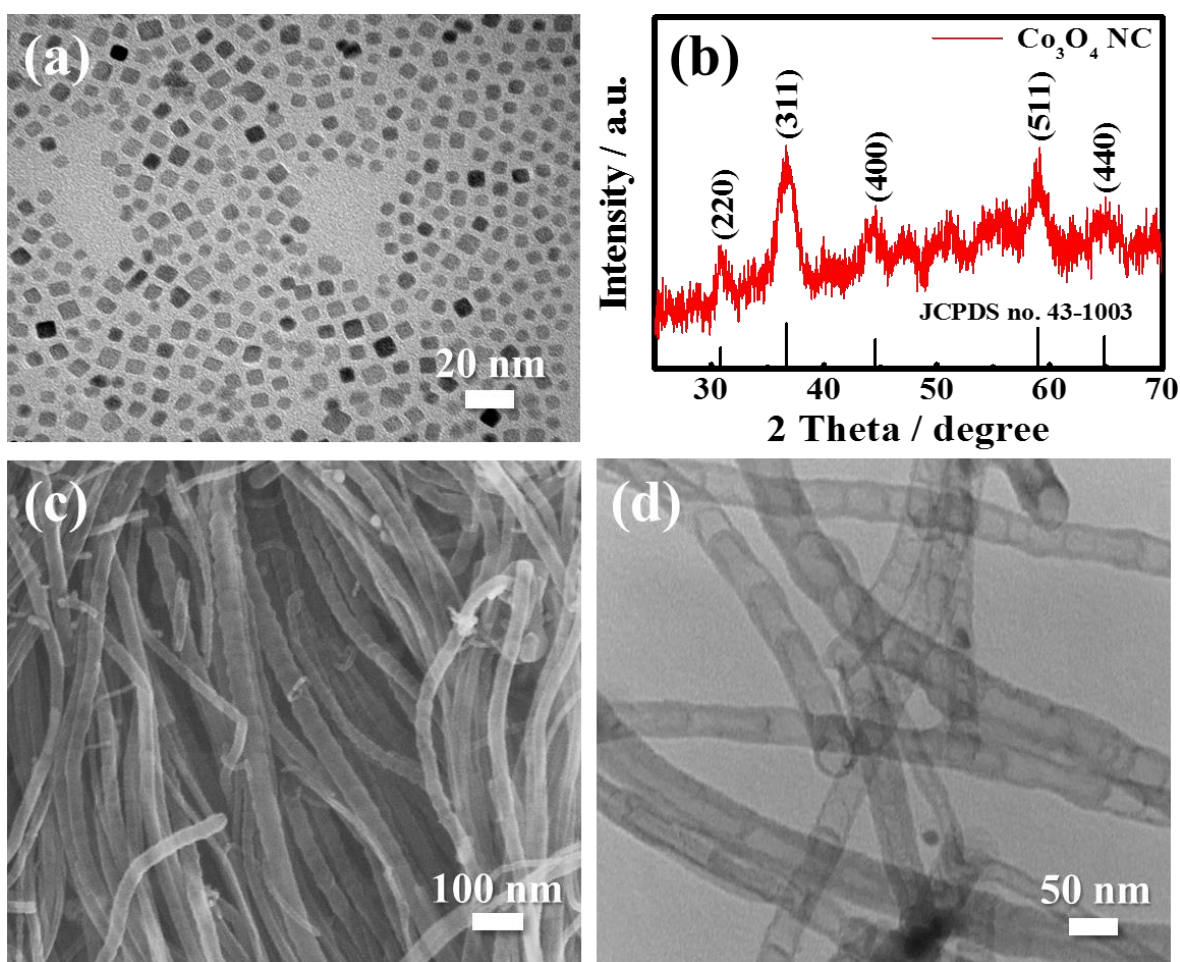


**Figure 14.** (a) TEM image and (b) XRD pattern of Co<sub>3</sub>O<sub>4</sub> NCs, and (c) SEM and (d) TEM images of N-CNTs.

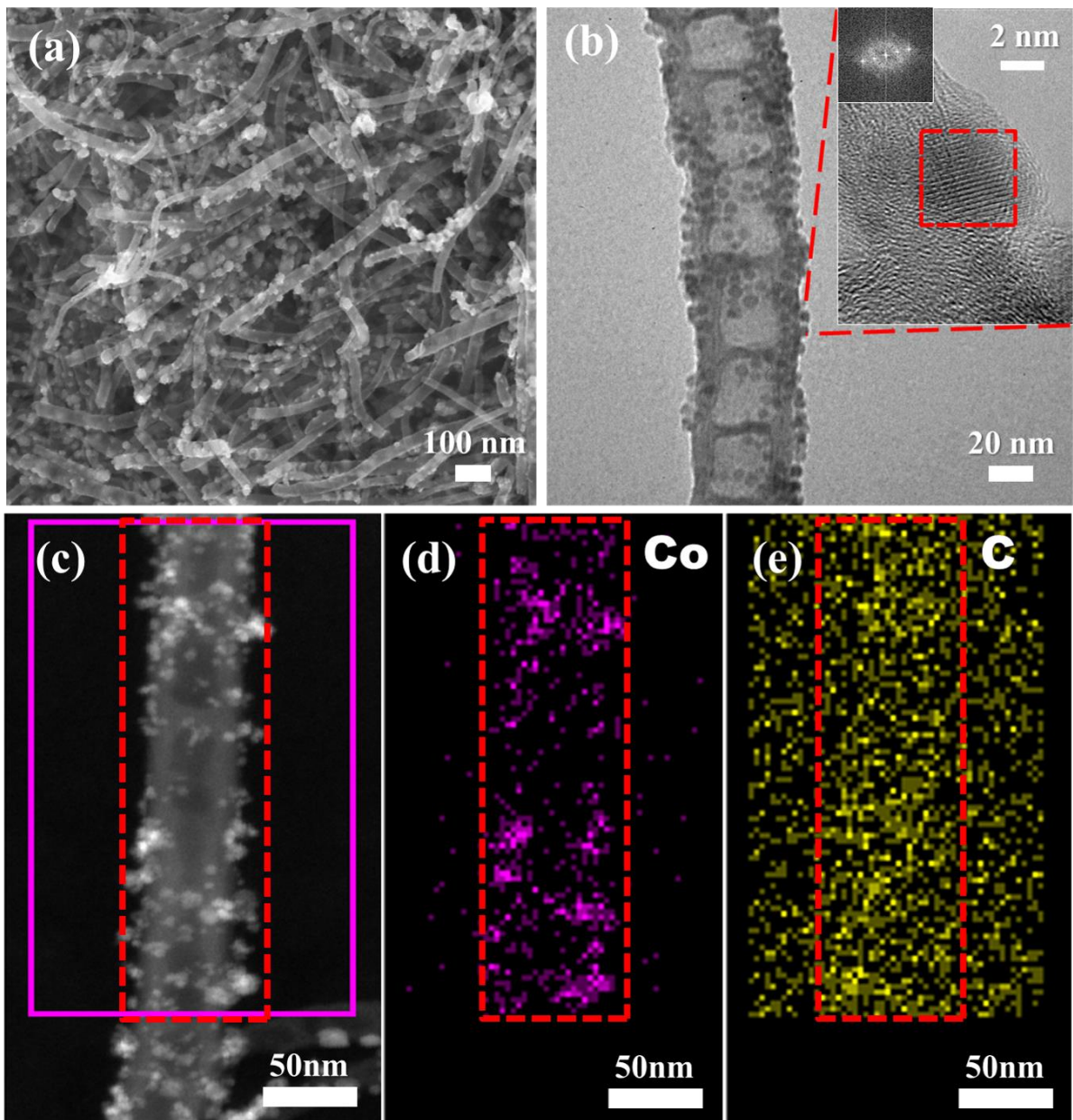


**Figure 15.** (a) SEM, (b) TEM, (c) STEM images of  $\text{Co}_3\text{O}_4$  NC/N-CNT and (d) cobalt and (e) carbon color mapping images obtained from EDX of  $\text{Co}_3\text{O}_4$  NC/N-CNT

**Figure 15** shows SEM and TEM images as well as STEM image with color mapping from EDX of  $\text{Co}_3\text{O}_4$  NC/N-CNT hybrid. In this present work, our strategy for creating a hybrid catalyst is based on the fast solvation-induced assembly of  $\text{Co}_3\text{O}_4$ /surfactant which is attracted via a strong hydrophobic interaction onto the surface of N-CNT. The resulting hybrid shows  $\text{Co}_3\text{O}_4$  NC still uniformly distributed onto the surfaces of N-CNT even after the removal of the surfactant (**Figure 15a**). A high magnification TEM image of a single N-CNT shows its surface uniformly decorated with  $\text{Co}_3\text{O}_4$  NCs, and its bamboo-like morphology is also observed (**Figure 15b**). This hybrid material improves the morphology of hydrothermally grown  $\text{Co}_3\text{O}_4$  particles from seed onto the surfaces of un-doped multi-walled CNT previously reported in our group.<sup>129</sup> The formation of unique morphology of  $\text{Co}_3\text{O}_4$  NC/N-CNT hybrid in this work is attributed to the two phase-induced  $\text{Co}_3\text{O}_4$  NC/surfactant system, which prevents aggregation and maintains the nanoscale particle size of  $\text{Co}_3\text{O}_4$  NCs. High resolution TEM (HR-TEM) image has been obtained in order to further examine the crystallinity of  $\text{Co}_3\text{O}_4$  NC with FFT pattern (**Figure 15b inset**),<sup>97</sup> which obviously demonstrates the high crystalline spinel structure of  $\text{Co}_3\text{O}_4$  NCs consistent with the XRD pattern. The adhesion of  $\text{Co}_3\text{O}_4$  NCs onto the surface of N-CNT is verified by scanning transmission electron microscopy (STEM) and the elemental distribution is obtained by EDX as shown in the color mapping (**Figure 15c, 15d and 15e**). In **Figure 15c**, a dashed rectangular area of N-CNT surface decorated with  $\text{Co}_3\text{O}_4$  NCs have resulted in purple-colored dots which are showing the spread of cobalt oxide nanoparticles which are corresponding with white small particles (**Figure 15d**) and the yellow-colored dots are

showing carbon species from N-CNTs (**Figure 15e**). The yellow spots observed outside the rectangle is due to the carbon-coated TEM copper grid.

TEM and SEM images of cobalt oxide nanocrystals decorated on Vulcan carbon ( $\text{Co}_3\text{O}_4$  NC/VC), which is synthesized by the same method as  $\text{Co}_3\text{O}_4$  NC/N-CNT hybrid.  $\text{Co}_3\text{O}_4$  NC/VC is employed as the control catalyst to elucidate the effect of the use of N-CNT as well as the synergistic effects between  $\text{Co}_3\text{O}_4$  NC and N-CNT, is also obtained comparing the morphological difference between two respective carbon supporting materials; N-CNT and VC (**Figure 16**). Similarly to  $\text{Co}_3\text{O}_4$  NC/N-CNT hybrid,  $\text{Co}_3\text{O}_4$  NCs are well distributed on the surface of VC particles. However, VC particles themselves are observed to be aggregated which reduces the overall active sites exposure of  $\text{Co}_3\text{O}_4$  NCs. This is indicative of the effectiveness of N-CNT for greatly enhancing the active site exposure of  $\text{Co}_3\text{O}_4$  NC by creating an intertwined network due to its 1-dimensional morphology. The intertwined network of N-CNT has also been proven to be effective in terms of transporting charges during electrochemical oxygen reaction.<sup>101</sup>

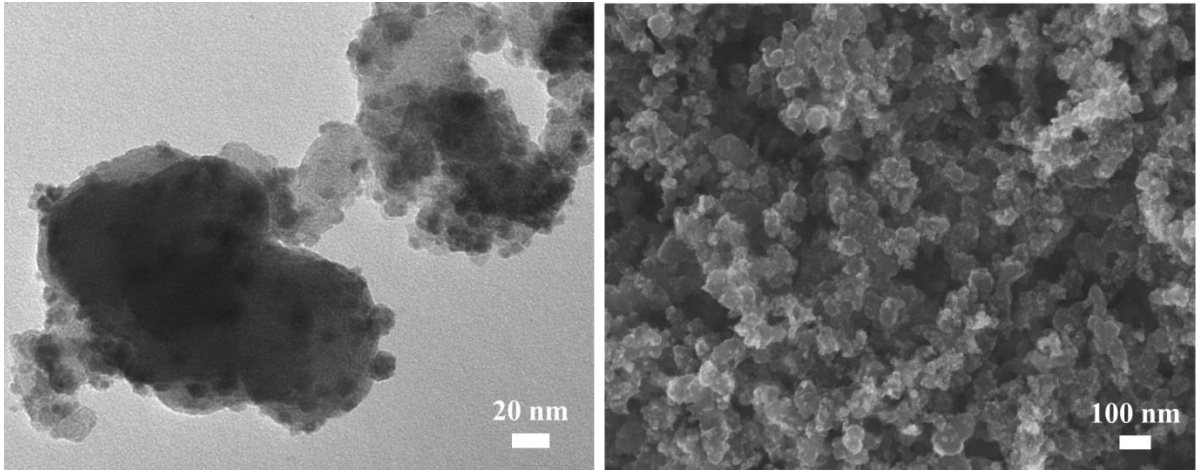


Figure 16. TEM and SEM images of  $\text{Co}_3\text{O}_4$  NC/VC composite

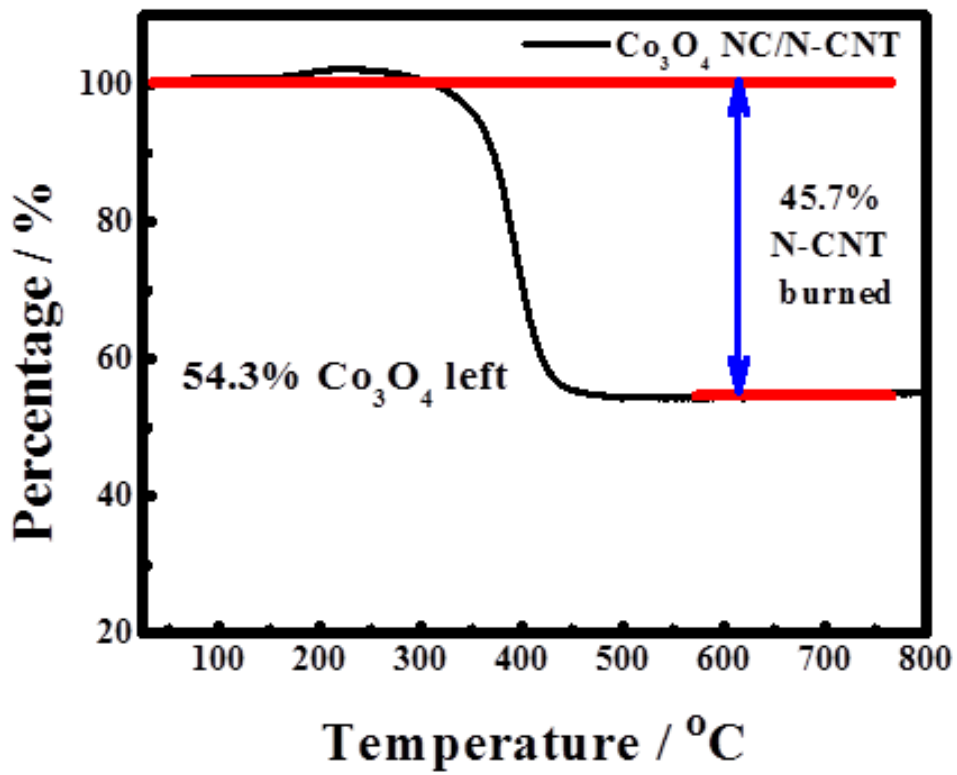
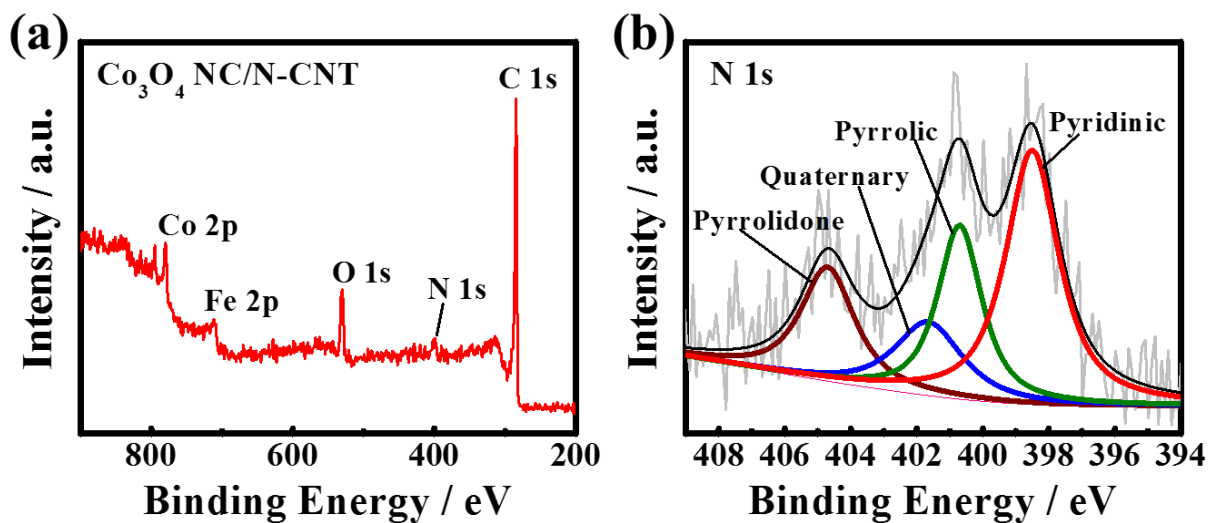


Figure 17. TGA data profiles of  $\text{Co}_3\text{O}_4$  NC/N-CNT

The TGA analysis of  $\text{Co}_3\text{O}_4$  NC/N-CNT has been conducted in air in order to measure the amount of  $\text{Co}_3\text{O}_4$  NC in the hybrid, where 45.7 % weight reduction has been observed over the temperature range of 300 to 450 oC due to the decomposition of N-CNT (**Figure 17**). Since N-CNT has been etched to remove the leftover iron from the injection CVD growth prior to hybridizing with  $\text{Co}_3\text{O}_4$  NC, the amount of  $\text{Co}_3\text{O}_4$  NC is determined to be 54.3 %.



**Figure 18.** (a) The XPS survey and (b) high-resolution N 1s spectrum of  $\text{Co}_3\text{O}_4$  NC/N-CNT composite: the grey and black lines are the raw and fitted spectra; the red, olive, blue and wine lines are pyridinic-N (398.5 eV, 42.21 %), pyrrolic-N (400.7 eV, 23.67 %), quaternary-N (401.65 eV, 15.37 %) and pyrrolidone-N (404.7 eV, 18.75 %), respectively.

To further elucidate the elemental composition and catalytically active sites of  $\text{Co}_3\text{O}_4$  NC/N-CNT hybrid catalyst, X-ray photoelectron spectroscopy (XPS) has been conducted. As

expected, the full XPS survey of Co<sub>3</sub>O<sub>4</sub> NC/N-CNT reveals peaks that correspond to Co 2p, Fe 2p, O 1s, N 1s, and C 1s (**Figure 18a**). The surface nitrogen content in N-CNT is confirmed to be 4.18 %, which is consistent with previously reported CVD grown nitrogen doped carbon nanotubes.<sup>48, 79, 101</sup> The high resolution N 1s spectrum of Co<sub>3</sub>O<sub>4</sub> NC/N-CNT hybrid has been de-convoluted into a series of four peaks, closely matching the binding energies of different nitrogen species such as pyridinic, pyrrolic, quaternary, and pyrrolidone (**Figure 18b**). The two species with the highest quantity, namely pyridinic and pyrrolic, are revealed to be 42.2 and 23.7 %, respectively. These ratio and binding energy of surface nitrogen groups are consistent with previously reported nitrogen-doped carbon nanotubes.<sup>48, 101</sup> Among the four different nitrogen atoms, pyridinic and quaternary nitrogen species have been noted to serve as the active site for ORR.<sup>107, 130-132</sup> This is appealing for combination with highly active OER electrocatalyst such as cobalt oxide in order to obtain highly efficient bi-functional air electrode catalyst. The high resolution Co 2p spectrum of the hybrid material has been de-convoluted into a series of 6 peaks, which are consistent with previously reported result (**Figure 19**).<sup>45</sup>

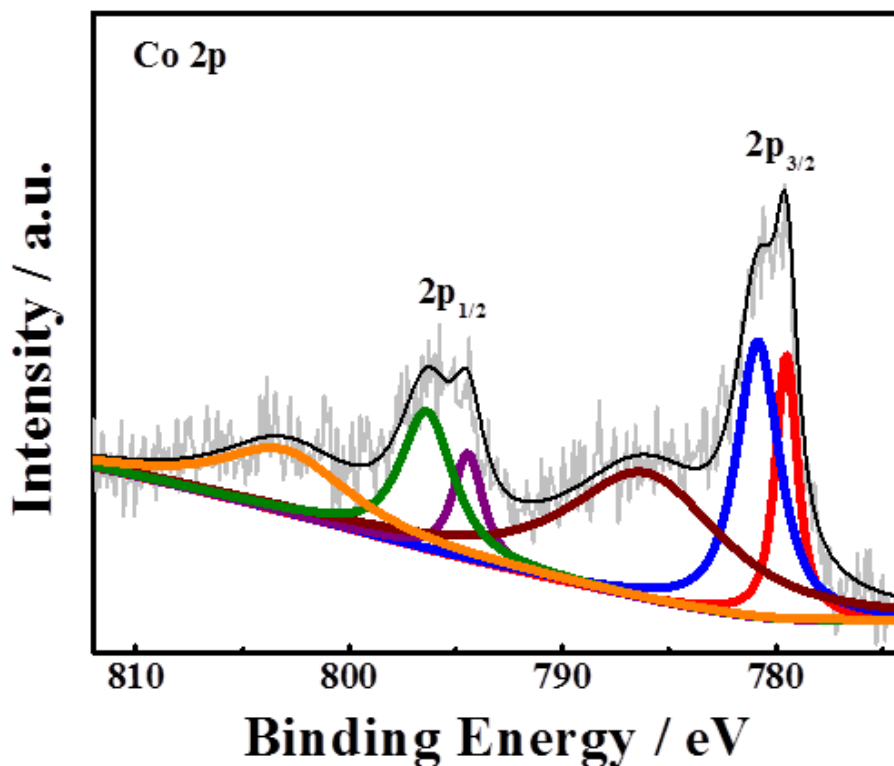


**Figure 19.** De-convoluted high-resolution Co 2p spectrum for  $Co_3O_4$  NC/N-CNT hybrid catalyst. It revealed two spin-orbit of  $2p_{1/2}$  and  $2p_{3/2}$  configurations each consisting of  $Co^{3+}$  and  $Co^{2+}$  cations doublet.<sup>133</sup> The bi-functional catalytic activity of  $Co_3O_4$  NC/N-CNT toward both ORR and OER are attributed to synergistic influences from combination between  $Co_3O_4$  NC and N-CNT: not only N-CNT provides high electrical conductivity and helps electron transfers, but also cobalt cations support the electron transfer by offering donor-acceptor chemisorption sites for the both reversible oxygen adsorption and desorption from the mixed-valencies of the Co cations coexisting in the same cubic spinel.<sup>133</sup> By this synergistic effect,  $Co_3O_4$  NC/N-CNT hybrid catalyst has better electrocatalytic activities and stability than those of N-CNT itself toward both oxygen reactions. Furthermore, the electron transfer occurs by hopping processes between the cations of different valencies which has relatively low activation energy, resulting in  $Co_3O_4$  having relatively high electrical conductivity. These excellent electronic properties of cubic spinel  $Co_3O_4$  help the hybrid catalyst to have synergistic effect and also make it an excellent candidate as a highly efficient catalyst for rechargeable zinc-air battery applications.

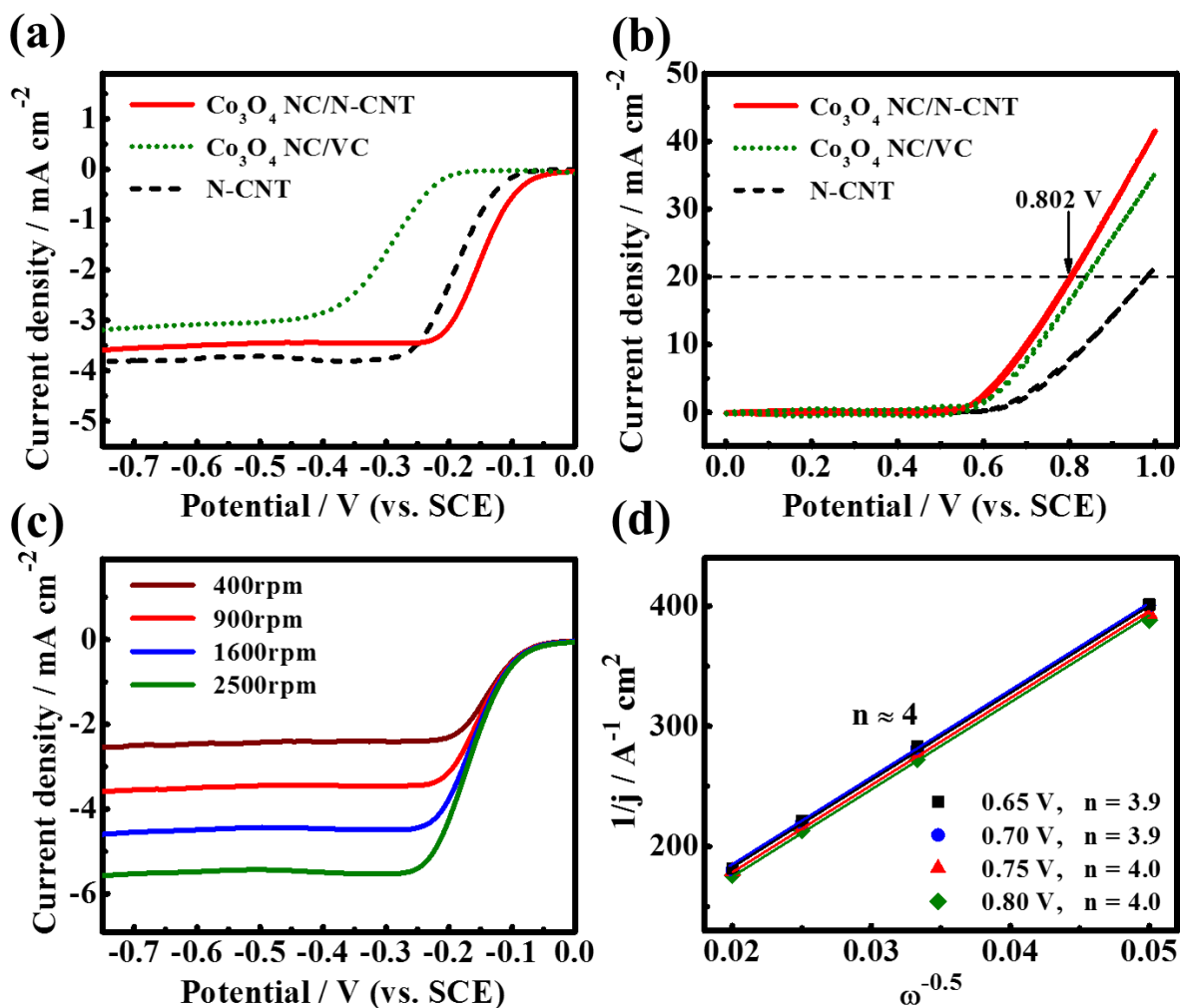


Figure 20. (a) ORR and (b) OER polarization curves of  $\text{Co}_3\text{O}_4$  NC/N-CNT compared to  $\text{Co}_3\text{O}_4$  NC/VC and N-CNT obtained at rotation speed of 900 rpm, (c) ORR polarization curves of  $\text{Co}_3\text{O}_4$  NC/N-CNT obtained at various rotating speeds (400, 900, 1600 and 2500 rpm), (d) K-L plot of  $\text{Co}_3\text{O}_4$  NC/N-CNT hybrid obtained at 0.65, 0.70, 0.75, and 0.80 V. ORR and OER experiments are conducted in  $\text{O}_2$ - and  $\text{N}_2$ -saturated 0.1M KOH, respectively.

**Figure 20a** shows ORR polarization curves of  $\text{Co}_3\text{O}_4$  NC/N-CNT hybrid compared to  $\text{Co}_3\text{O}_4$  NC/VC and N-CNT as reference materials. Among the three,  $\text{Co}_3\text{O}_4$  NC/N-CNT clearly shows the most positive half-wave potential as well as the lowest overpotential which are indicative of high electrochemical catalytic activity toward ORR. Although  $\text{Co}_3\text{O}_4$  NC/N-CNT has less N-CNT loading compared to that of N-CNT tested itself (because the total loading is kept the same),  $\text{Co}_3\text{O}_4$  NC/N-CNT shows significantly improved onset and half-wave potentials. Even though the ORR of  $\text{Co}_3\text{O}_4$  NC/N-CNT proceeds in the four electron pathway, as determined by Koutecky-Levich (K-L) analysis later, a slightly lower limiting current density obtained with  $\text{Co}_3\text{O}_4$  NC/N-CNT compared to that of N-CNT is likely due to non-ideal factors in the catalyst coated layer on the glassy carbon such as film thickness resistance and trapped hydrogen peroxide species formed by the ORR catalyzed on  $\text{Co}_3\text{O}_4$  NC within the electrode.<sup>134, 135</sup> The combination of  $\text{Co}_3\text{O}_4$  NC with N-CNT via hydrophobicity induced coupling resulting in superior ORR activity signifies a strong synergistic effect between the two.  $\text{Co}_3\text{O}_4$  NC/VC combined by the same method as  $\text{Co}_3\text{O}_4$  NC/N-CNT is observed to be significantly lacking the ORR activity based on considerably negative onset and half-wave potentials and reduced limiting current density. To investigate the bi-functionality of  $\text{Co}_3\text{O}_4$  NC/N-CNT, OER activity is investigated by conducting CV in the voltage range of 0 to 1 V vs. SCE. (**Figure 20b**) The hybrid catalyst clearly shows the best OER activity demonstrated by the highest OER current density of 42 mA cm<sup>-2</sup> obtained at 1.0 V. Furthermore,  $\text{Co}_3\text{O}_4$  NC/N-CNT shows the least overpotential of 0.802 V vs. SCE obtained at 20 mA cm<sup>-2</sup>. Even though  $\text{Co}_3\text{O}_4$  NC/VC demonstrates the same onset potential

( $\sim 0.57$  V vs. SCE), the OER current density at 1.0 V is only 35 mA cm<sup>-2</sup>. The ORR and OER activities of the three catalysts have been summarized (**Table 3**). The synergistic combination of Co<sub>3</sub>O<sub>4</sub> NC and N-CNT via hydrophobicity induced coupling is again demonstrated for OER compared to the poor onset potential and low current density obtained with N-CNT itself. With addition of Co<sub>3</sub>O<sub>4</sub> NC, OER onset potential and current density have been significantly improved. The two materials are synthesized by using the same Co<sub>3</sub>O<sub>4</sub> NCs, utilized as OER active electrocatalyst, but carbon supporting materials are only different where not only VC covered surface of Co<sub>3</sub>O<sub>4</sub> NCs with decreasing exposed active sites toward OER, but also N-CNT provides largely high electrical conductivity and bridge for transferring electrons as well as increasing exposed active sites for higher OER activity.

**Table 3. Summary of half-cell results: onset potential, half-wave potential, maximum current density from ORR polarization curves and cell potential at 20 mA cm<sup>-2</sup> and durability of the catalyst performance, respectively. Onset potential was measured at -0.01 mA cm<sup>-2</sup>**

Samples	ORR			OER	
	Onset potential / V	Half-wave potential / V (based on -0.5 V)	Limiting current Density / mA cm <sup>-2</sup>	Cell potential at 20 mA cm <sup>-2</sup> / V	Current retention at 1.0 V / %
Co <sub>3</sub> O <sub>4</sub> NC/N-CNT	-0.044	-0.148	-3.55	0.802	91.22
Co <sub>3</sub> O <sub>4</sub> NC/VC	-0.193	-0.293	-3.15	0.840	40.66
N-CNT	-0.089	-0.186	-3.79	0.980	4.49
Pt/C + Ir/C	-0.032	-0.134	-3.99	0.762	8.92

To further understand excellent ORR kinetics of  $\text{Co}_3\text{O}_4$  NC/N-CNT hybrid catalyst, K-L analysis has been conducted at various electrode potentials (0.65 V, 0.70 V, 0.75 V and 0.80 V) (**Figure 20d**) based on Koutecky-Levich equation using ORR measurements obtained by RDE at four different electrode rotation speeds of 400, 900, 1600 and 2500 rpm (**Figure 20c**). These parallel and linear shaped fitting lines indicate first-order reaction kinetics toward the saturated oxygen species. The number of electrons transferred,  $n$ , during ORR is confirmed to be 3.9, 3.9, 4.0 and 4.0 at potentials between 0.65, 0.70, 0.75, and 0.80 V (vs SCE), respectively. This indicates fast kinetics with predominant four-electron reduction reaction mechanism throughout the entire potential range inspected. This high activity toward ORR is attributed to the synergy between  $\text{Co}_3\text{O}_4$  NC and N-CNT and the coupling of the two by strong hydrophobic interaction for improved active surface area and charge transport properties. To emphasize potential use of  $\text{Co}_3\text{O}_4$  NC/N-CNT hybrid catalyst for practical applications, its ORR and OER activities are compared to those of commercial state of art catalysts, Pt/C and Ir/C (**Figure 21a** and **21b**, respectively). Since Pt/C and Ir/C are known to be mono-functionally active toward ORR and OER, respectively, the two have been physically mixed together in 1 to 1 ratio to create a bi-functionally active counterpart. The ORR measurements of the catalysts reveal that even though the mix of Pt/C and Ir/C slightly outperforms  $\text{Co}_3\text{O}_4$  NC/N-CNT in terms of onset and half-wave potentials, and limiting current density, the cost effectiveness of the hybrid catalyst compensates for the sacrificed performance. Similarly, the OER activity of the mix of Pt/C and Ir/C slightly outperforms that of  $\text{Co}_3\text{O}_4$  NC/N-CNT in terms of onset potential and OER current density.

The ORR and OER activities of the composite can be further enhanced by introducing second transition metal such as  $\text{NiCo}_2\text{O}_4$  and co-doping of carbon nanotubes such as sulfur-, nitrogen-doped carbon nanotubes, to outperform Pt/C and Ir/C, which will be investigated in our future work.

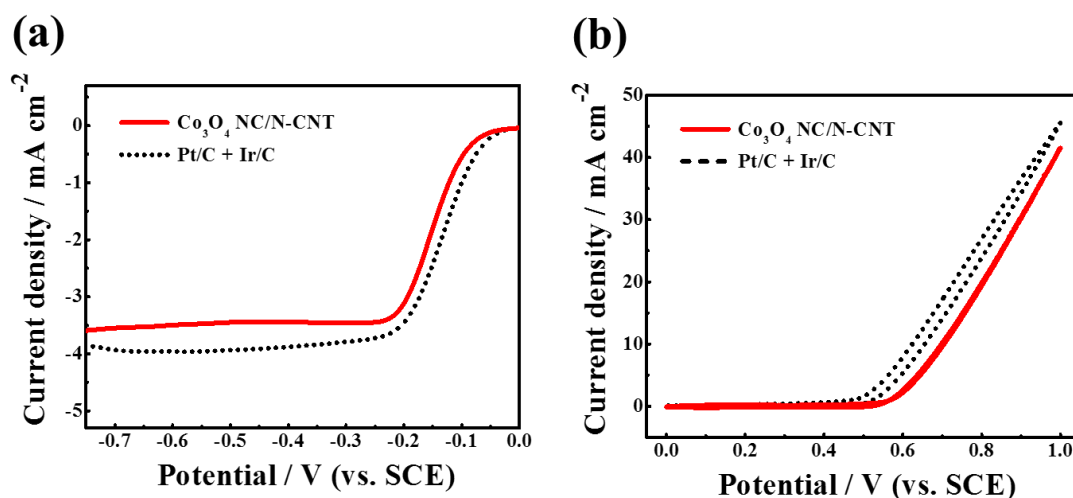


**Figure 21.** (a) ORR and (b) OER polarization curves for hybrid and Pt/C+Ir/C as the precious metal-based reference sample (900 rpm). ORR and OER experiments are conducted in O<sub>2</sub>- and N<sub>2</sub>-saturated 0.1 M KOH, respectively. Scan rate: 10mV s<sup>-1</sup> and electrolyte: 0.1 M KOH. Onset potential is measured at -0.01 mA and limiting current is measured at -0.8 V (vs. SCE).

In addition to the ORR and OER activities of Co<sub>3</sub>O<sub>4</sub> NC/N-CNT, the electrochemical durability of the hybrid catalyst has been investigated to further highlight its potential application in practical rechargeable metal-air batteries (**Figure 22**). The electrochemical durability is tested by conducting repeated CV in the range of 0 to 1 V vs SCE, to expose the

catalyst to severely oxidative conditions. Even after 1000 cycles,  $\text{Co}_3\text{O}_4$  NC/N-CNT hybrid catalyst shows relatively very low degradation in current density at 1 V (vs SEC) (**Figure 22a**), whereas  $\text{Co}_3\text{O}_4$  NCs/VC, N-CNT, and the mix of Pt/C and Ir/C demonstrate significant reduction in current density (N-CNT only after 300 cycles) (**Figure 22b, c, d** and **Table 3**). Even though  $\text{Co}_3\text{O}_4$  NC helps to reduce the overpotential associated with OER for both N-CNT and VC supported hybrids,  $\text{Co}_3\text{O}_4$  NC/N-CNT demonstrates much higher current density retention (91.2 %) than  $\text{Co}_3\text{O}_4$  NC/VC (40.7 %) due to the graphitized carbon in N-CNT which is known to be electrochemically very stable.<sup>136-138</sup> In addition, the improved durability is ascribed to the morphological advantage of highly intertwined network of 1-dimensional carbon nanotubes over granular morphology created by VC.<sup>48</sup> Although the mix of Pt/C and Ir/C has shown superior initial activity than  $\text{Co}_3\text{O}_4$  NC/N-CNT, it is clearly observed to demonstrate poor durability, which highlights the hybrid catalyst as a potential replacement for practical applications. The loss of current density of Pt/C and Ir/C is most likely attributed to the corrosion of carbon during exposure to high charging potentials, however,  $\text{Co}_3\text{O}_4$  NC/N-CNT is significantly less affected due to synergistically enhanced catalytic activity which prevents N-CNT from prolific corrosion.<sup>18, 48, 101</sup>

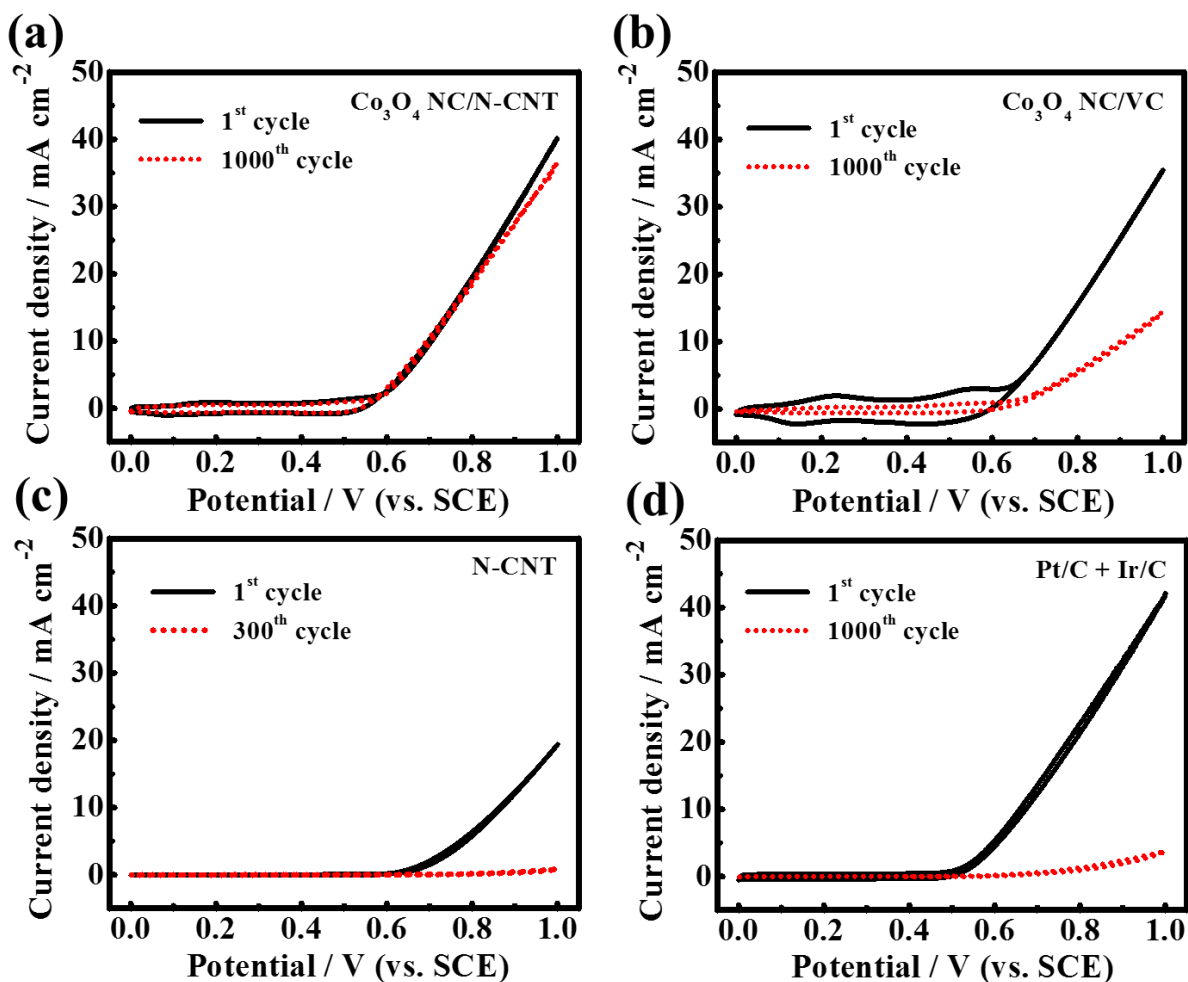


**Figure 22.** The 1<sup>st</sup> and 1000<sup>th</sup> CV cycle in the OER region obtained with (a) Co<sub>3</sub>O<sub>4</sub> NC/N-CNT, (b) Co<sub>3</sub>O<sub>4</sub> NC/VC, (c) N-CNT (300<sup>th</sup>) and (d) Pt/C+Ir/C.

To corroborate excellent bi-functional activities of Co<sub>3</sub>O<sub>4</sub> NC/N-CNT hybrid catalyst confirmed by half-cell testing, single-cell rechargeable zinc-air cell prototype has been fabricated and the hybrid material has been tested as air electrode catalyst to emphasize its electrocatalytic performance in a realistic environment. The zinc-air battery performance of the catalysts has been investigated by conducting galvanodynamic charge and discharge to

observe the behavior of battery operation in terms of voltage for a wide range of applied (or drawn) current density (**Figure 23a**). Open circuit voltages of  $\text{Co}_3\text{O}_4/\text{N-CNT}$  and N-CNT itself are observed to be comparable and higher than that of  $\text{Co}_3\text{O}_4$  NC/VC due to superior electrical conductivity of the carbon nanotubes. In terms of discharge,  $\text{Co}_3\text{O}_4$  NC/N-CNT demonstrates the best discharge performance as evident by the highest discharge voltages obtained at all tested range of current density. The differences in the discharge voltage become more obvious at high current densities, which is indicative of superior rate capability of  $\text{Co}_3\text{O}_4$  NC/N-CNT. The trend in observed discharge performance is consistent with that of the half-cell testing where N-CNT shows better performance than  $\text{Co}_3\text{O}_4$  NC/VC most likely due to fast charge transport facilitated by highly electrically conductive carbon nanotubes. During the battery charging,  $\text{Co}_3\text{O}_4$  NC/N-CNT demonstrates best overall OER performance with significantly lower charging potentials particularly at high current densities.

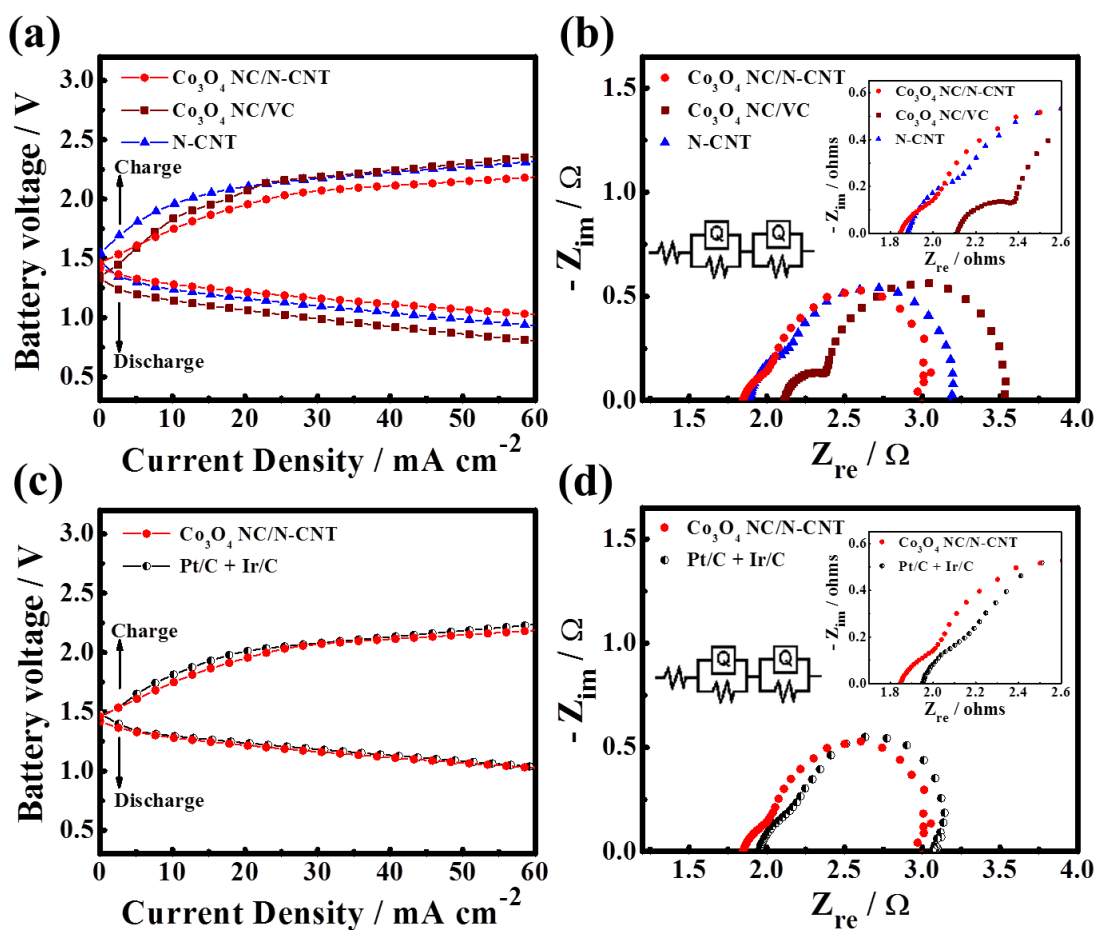


**Figure 23.** (a, and c) Galvanodynamic charge and discharge behaviors, and (b, and d) Nyquist plots obtained by EIS of Co<sub>3</sub>O<sub>4</sub> NC/N-CNT (red circle), Co<sub>3</sub>O<sub>4</sub> NC/VC (wine hexagon), N-CNT (blue triangle), and Pt/C+Ir/C (black half circle). (b, and d insets) High frequency range of the Nyquist plot, and the equivalent circuit.

In addition to the galvanodynamic charging and discharging behaviors of the catalysts, electrochemical impedance spectroscopy (EIS) have been conducted in the ORR region at 0.8 V for the catalysts to further investigate the resistances associated with rechargeable zinc-air battery operation (**Figure 23b, inset**). The EIS testing has resulted in Nyquist plots

composed of two different sized semi-circles, which are modelled by an equivalent circuit with five parameters,  $R_s$ ,  $R_{int}$ ,  $R_{ct}$ ,  $Q_{int}$  and  $Q_{dl}$ , consistent with our previously reported zinc-air battery results.<sup>45, 48, 101</sup> Each resistance has its own physical interpretation.  $R_s$  represents solution resistance in electrolyte and  $R_{int}$  represents solid-electrolyte interface resistance between solid and liquid of electrode.  $R_{ct}$  represents charge-transfer resistance from the air electrode, which is directly related with the degree of the catalytic activity of the catalyst. Based on the equivalent circuit, the impedance parameters of each catalysts are listed in **Table 4**, where  $Co_3O_4$  NC/N-CNT hybrid catalyst exhibits the least charge transfer resistance ( $R_{ct}$ ) as compared to those of  $Co_3O_4$  NC/VC and N-CNT, which is clearly consistent with the result obtained from galvanodynamic discharge. The hybrid also presents the lowest values of  $R_s$  and  $R_{int}$  which are due to the addition of highly electrically conductive N-CNT and excellent distribution of  $Co_3O_4$  NC on the surfaces of N-CNT, respectively. On the basis of the outstanding charge, discharge performance and impedance results of  $Co_3O_4$  NC/N-CNT, physically mixed Pt/C and Ir/C commercial catalysts has been tested to compare the viability of the hybrid catalyst as potential commercial electrode material (**Figure 23c and 23d, inset**). In fact, the galvanodynamic charge and discharge of  $Co_3O_4$  NC/N-CNT is very comparable to that of Pt/C and Ir/C mix clearly demonstrated by similar charge and discharge voltages throughout the tested current densities. The excellent performance of the hybrid is confirmed by EIS where all three resistances,  $R_s$ ,  $R_{int}$ , and  $R_{ct}$ , demonstrate smaller values than those of the precious metal-based catalyst (**Table 4**), which could potentially replace these catalyst for practical applications.

**Table 4.** The values of the equivalent circuit elements based on the EIS analysis of Co<sub>3</sub>O<sub>4</sub> NC/N-CNT, Co<sub>3</sub>O<sub>4</sub> NC/VC, N-CNT and mix of Pt/C and Ir/C.

cycle no.	Impedance parameters	Co <sub>3</sub> O <sub>4</sub> NC/N-CNT	Co <sub>3</sub> O <sub>4</sub> NC/VC	N-CNT	Pt/C+Ir/C
Initial	R <sub>s</sub> (Ω)	1.849	2.116	1.887	1.954
	R <sub>int</sub> (Ω)	0.199	0.284	0.264	0.236
	R <sub>ct</sub> (Ω)	1.026	1.139	1.061	1.046
	Q <sub>int</sub> (S·s <sup>n</sup> )	0.0105	0.002425	0.00565	0.01462
	Q <sub>dl</sub> (S·s <sup>n</sup> )	0.01349	0.01178	0.01366	0.0274
After cycling	R <sub>s</sub> (Ω)	2.443	3.28	2.677	3.189
	R <sub>int</sub> (Ω)	0.721	0.726	0.511	0.402
	R <sub>ct</sub> (Ω)	1.902	10.97	3.967	4.686
	Q <sub>int</sub> (S·s <sup>n</sup> )	2.41 × 10 <sup>-3</sup>	0.2879	6.44 × 10 <sup>-3</sup>	2.57 × 10 <sup>-3</sup>
	Q <sub>dl</sub> (S·s <sup>n</sup> )	5.71 × 10 <sup>-3</sup>	1.56 × 10 <sup>-3</sup>	7.91 × 10 <sup>-3</sup>	5.83 × 10 <sup>-3</sup>

To further support excellent charge and discharge capabilities of Co<sub>3</sub>O<sub>4</sub> NC/N-CNT hybrid as bi-functional air electrode catalyst for rechargeable zinc-air batteries, its cycle stability is investigated by galvanostatically charging and discharging the battery at 20 mA cm<sup>-2</sup> (**Figure 24**). As expected, the battery with Co<sub>3</sub>O<sub>4</sub> NC/N-CNT shows very stable charge and discharge voltages, 2.16 and 1.14 V respectively, demonstrating virtually negligible voltage fading for more than 200 cycles (2000 min) (**Figure 24a**). The cycle stability of other batteries with Co<sub>3</sub>O<sub>4</sub> NC/VC, N-CNT, and the mix of Pt/C and Ir/C, however, have demonstrated significant voltage losses only after ~40 cycles before the batteries were stopped due to very high overpotentials (**Figure 24b, 24c and 24d**). The voltage losses in these batteries are mainly attributed to the corrosion of carbon which occurs due to high charge voltages. This leads to the loss of catalytically active surface area and the poisoning of the electrolyte which results in the loss of discharge voltages as well. The rate of charge

voltage loss is more severe for  $\text{Co}_3\text{O}_4$  NC/VC than N-CNT itself due to the amorphous nature of VC, whereas graphitic carbon of N-CNT mitigates the rate of degradation. Similarly, the mix of Pt/C and Ir/C demonstrates severe degradation in terms of both charge and discharge voltages even though its initial performance is superior. Furthermore, the initial four cycles of charge/discharge profiles of  $\text{Co}_3\text{O}_4$  NC/VC, N-CNT and the mix of Pt/C and Ir/C demonstrate larger overpotentials, while  $\text{Co}_3\text{O}_4$  NC/N-CNT shows relatively narrower difference between charge/discharge voltages (**Inset in Figure 24b, 24c and 24d**, respectively). This galvanostatic cycling test is indicative of the importance of having both stable graphitic carbon and highly OER active  $\text{Co}_3\text{O}_4$  NC to minimize charge/discharge voltage degradations.

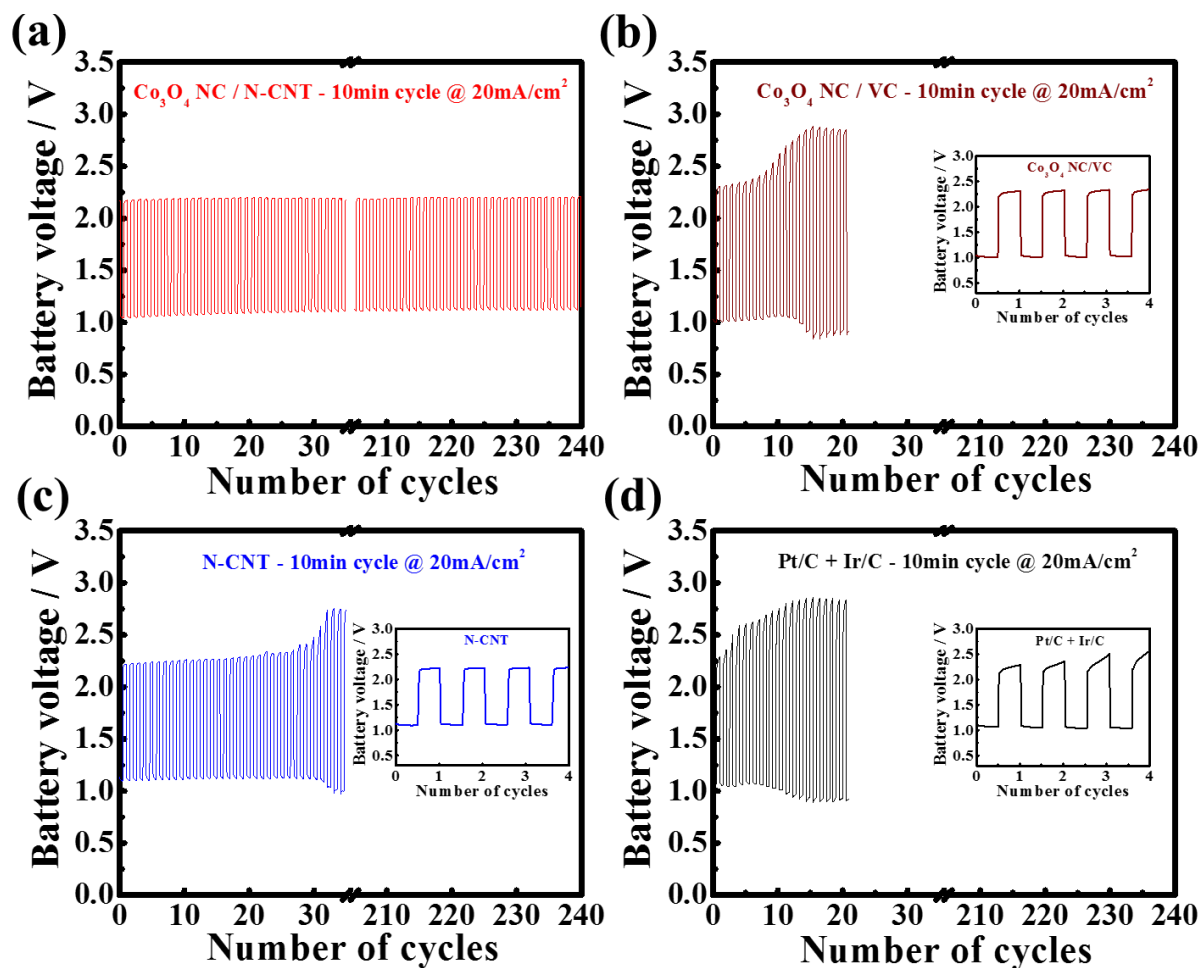
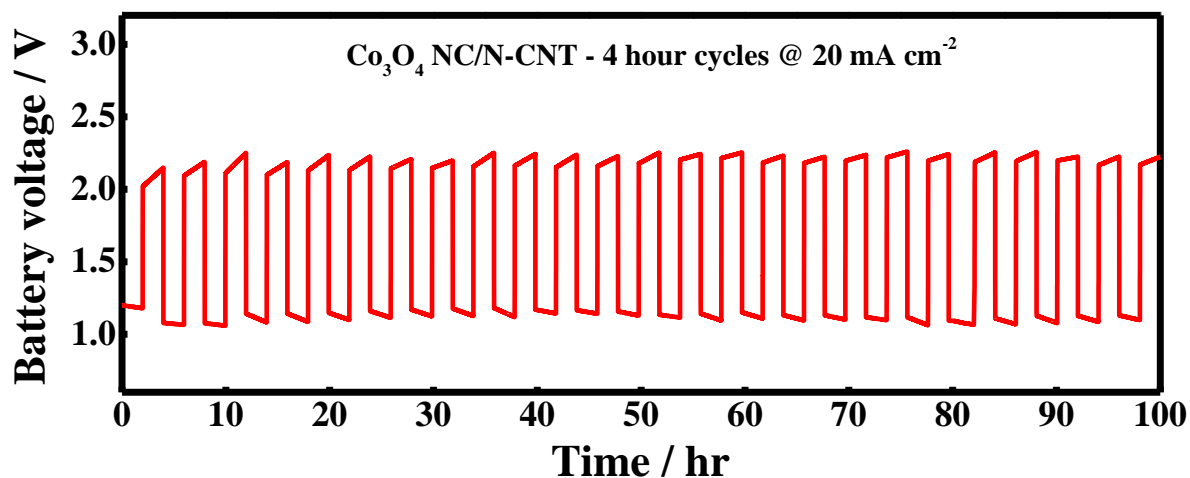
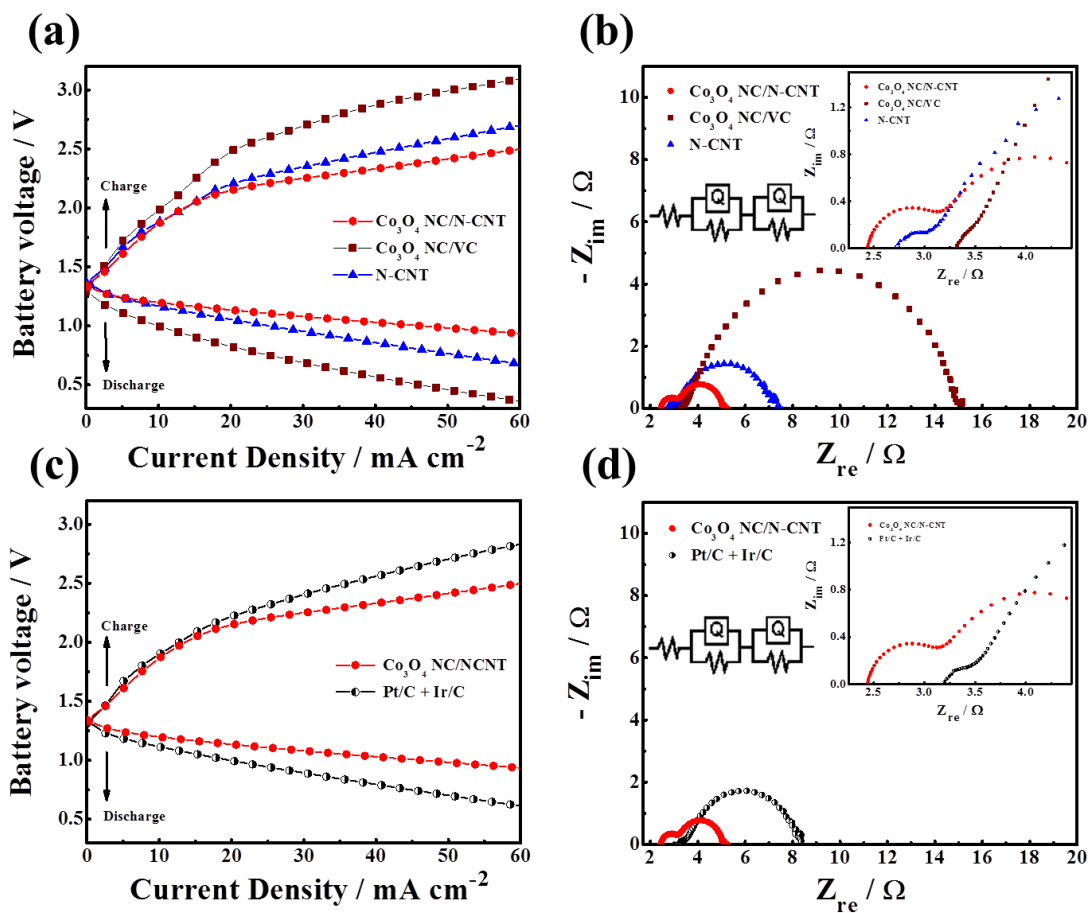


Figure 24. Galvanostatic charge and discharge (C-D) cycling obtained at 20 mA cm<sup>-2</sup> of (a) Co<sub>3</sub>O<sub>4</sub> NC/N-CNT, (b) Co<sub>3</sub>O<sub>4</sub> NC/VC, (c) N-CNT, and (d) Pt/C+Ir/C. Insets: The initial 4 cycles of each catalyst.



**Figure 25.** Long term galvanostatic charge and discharge (C-D) cycling obtained at 20mA cm<sup>-2</sup> of Co<sub>3</sub>O<sub>4</sub> NC/N-CNT. Each charge and discharge state was 2 hours (4 hours per cycle).

To further confirm the durability of the hybrid catalyst, a long term galvanostatic C-D cycling test is conducted using 4 hour cycling interval (2 hour discharge then 2 hour charge) at the same current density (**Figure 25**). Even though this leads to a harsh testing condition for the catalyst in terms of electrochemical durability, the battery exhibits very stable voltages over 100 hours (350000 seconds). This result obtained by longer charging and discharging regimes additionally demonstrates the potential use of highly active and durable Co<sub>3</sub>O<sub>4</sub> NC/N-CNT hybrid bi-functional catalyst as efficient air electrode material for real applications.



**Figure 26.** (a, and c) Galvanodynamic battery behaviors, and (b, and d) Nyquist plots obtained by EIS after durability cycling test of  $\text{Co}_3\text{O}_4$  NC/N-CNT (red circle),  $\text{Co}_3\text{O}_4$  NC/VC (wine hexagon), N-CNT (blue triangle), and Pt/C+Ir/C (black half circle). (b, and d insets: High frequency range of the Nyquist plot, and the equivalent circuit.)

After galvanostatic cycling tests, the same batteries have been tested for galvanodynamic charge and discharge to further verify the durability of the catalysts (**Figure 26a and 26c**).  $\text{Co}_3\text{O}_4$  NC/VC suffers from the largest charge and discharge performance losses compared to its initial performance observed by the greater increase in charge and discharge overpotentials.  $\text{Co}_3\text{O}_4$  NC/N-CNT hybrid catalyst shows the least drop and rise in discharge and charge voltage, respectively, which elucidates electrochemical stability with highly active bi-functional properties. The precious bi-functional mix of Pt/C and Ir/C catalyst also displays considerably enlarged charge/discharge voltage difference in contrast to that of the hybrid material. The order of the increased overpotential between charge and discharge profiles from that at the initial stage is  $\text{Co}_3\text{O}_4$  NC/N-CNT < N-CNT < Pt/C and Ir/C <  $\text{Co}_3\text{O}_4$  NC/VC, which are 0.297 V, 0.501 V, 0.883 V and 1.126V, respectively, at relatively high current density of 50 mA cm<sup>-2</sup> (**Table 5 and 6**). With respect to electrochemical resistances in the zinc air battery single cell, EIS is also conducted at the last stage after C-D cycling experiments as displayed by the Nyquist plots (**Figure 26b and 26d**). In agreement with the trend of increasing overpotentials before and after the galvanostatic charge and discharge cycling test, the increase in the electrochemical resistances is observed in order of  $\text{Co}_3\text{O}_4$  NC/N-CNT < pure N-CNT < Pt/C and Ir/C <  $\text{Co}_3\text{O}_4$  NC/VC. Conclusively, all of electrochemical characterizations such as half-cell testing, galvanodynamic and galvanostatic charge and discharge and EIS demonstrate consistent durability trend among the catalysts. In comparison with the other electrocatalysts,  $\text{Co}_3\text{O}_4$  NC/N-CNT hybrid catalyst definitely reveals strong electrochemical durability and excellent rechargeability as

well as highly active and bi-functional performance in both half-cell testing and zinc air battery cycling experiments.

**Table 5. Battery voltage obtained at  $50 \text{ mA cm}^{-2}$  during galvanodynamic discharge and charge before galvanostatic C-D cycling test**

Samples	Battery voltage at $50 \text{ mA cm}^{-2}$ during discharge / V	Battery voltage at $50 \text{ mA cm}^{-2}$ during charge / V
$\text{Co}_3\text{O}_4$ NC/N-CNT	1.049 V	2.158 V
$\text{Co}_3\text{O}_4$ NC/VC	0.876 V	2.282 V
N-CNT	0.957 V	2.277 V
Pt/C + Ir/C	1.062 V	2.183 V

**Table 6. Battery voltage obtained at  $50 \text{ mA cm}^{-2}$  during galvanodynamic discharge and charge after galvanostatic C-D cycling test**

Samples	Battery voltage at $50 \text{ mA cm}^{-2}$ during discharge / V	Battery voltage at $50 \text{ mA cm}^{-2}$ during charge / V
$\text{Co}_3\text{O}_4$ NC/N-CNT	0.985 V	2.391 V
$\text{Co}_3\text{O}_4$ NC/VC	0.460 V	2.992 V
N-CNT	0.768 V	2.589 V
Pt/C + Ir/C	0.702 V	2.706 V

#### 4.1.4 Conclusions and Remarks

In this study, a facile synthesis method to decorate cobalt oxide nanocrystals onto the surface of nitrogen-doped carbon nanotubes is introduced based on hydrophobicity-induced solvation to obtain highly active  $\text{Co}_3\text{O}_4$  NC/N-CNT hybrid electrocatalyst. The catalyst is formed by novel synthesis utilizing strong hydrophobicity via interactions between surfactants encapsulating  $\text{Co}_3\text{O}_4$  NCs and graphitic walls of N-CNTs. From RDE half-cell testing and practical rechargeable zinc air battery measurements, the synergistic effect of  $\text{Co}_3\text{O}_4$  NC/N-CNT hybrid catalyst is verified by comparing to  $\text{Co}_3\text{O}_4$  NC/VC and N-CNT itself, which demonstrate relatively lower bi-functional activities. The comparable ORR and OER activity of the hybrid catalyst to the precious metal-based catalyst such as Pt/C and Ir/C, respectively, highlights its potential for usage in practical applications. The synergistic effect is obtained from the hydrophobic combination between N-doped CNT, which mainly provides highly active ORR sites and exceptional electrical conductivity for rapid charge transfer, and  $\text{Co}_3\text{O}_4$  NC, which provides highly exposed OER active sites. In addition to the high bi-functional activity,  $\text{Co}_3\text{O}_4$  NC/N-CNT exhibits remarkably stable OER polarization curves at very high potential range between 0 V and 1 V (vs. SCE) while sustaining more than 90 % in OER current retention even after 1000 CV cycles. The practicality of the hybrid catalyst is further elucidated by excellent cycling durability as well as the lowest overpotential between charge and discharge performances in a realistic rechargeable zinc air battery in ambient condition. By utilizing simple and facile synthesis of the nanocrystals

with N-CNT,  $\text{Co}_3\text{O}_4$  NC/N-CNT hybrid catalyst is highly promising for the next generation rechargeable batteries such as metal-air batteries and alkaline full cells.

## Section 5: Directions for Future Researches

The future directions will be focused on the design, synthesis, and evaluation of nanostructured transition metal oxides such as cobalt oxides, nickel oxides, and their composite, which is due to the fact that the transition metal oxides have high OER activity and great electrochemical stability in the extremely high potential range of OER. In general, the most detrimental problem that must be overcome for the practical use of electrically rechargeable zinc-air battery is considerable overpotential during OER, which is corresponding to high charging potential during the battery cycling, where it typically makes the charge potential of zinc-air battery higher than 2 V and it is too high for the electrocatalysts to maintain their original status giving rise to severe problem on preserving long cycle life. This is why the transition metal oxides must be employed for the development of bi-functional electrocatalyst for electrically rechargeable zinc-air battery. Even though their electrical conductivity is relatively low, it can be optimized via modifications such as metal composition, crystalline structure, morphology, and use of conductive materials.

Therefore, the future directions are briefly classified into four categories in order to not only obtain highly active and durable bi-functional catalyst, but also systematically and efficiently carry out experiments and testing as outlined below.

(1) Morphological design of metal oxides including cobalt oxide and nickel oxide by modifying metal composition and crystal structure or using template material such as silica and polystyrene beads so as to maximize the exposed surface area of the metal oxides and prevent aggregation properties over cycling by making strong structures, which are for high activity and long durability, respectively.

(2) Hybridizing the metal oxides with functionalized carbon such as nitrogen-doped carbon nanotube (N-CNT) and nitrogen-doped graphene (N-GP) through innovative methods,

which provide high conductivity and ORR activity as well as high surface area serving as a substrate.

(3) Metal doping on the metal oxide surface in order to alleviate the low conductivity and low ORR activity of the metal oxides as well as long durability.

(4) Electrochemical evaluation of the developed catalysts by RDE half-cell testing and rechargeable zinc-air battery testing containing ORR/OER and discharge/charge profiles, respectively, and moreover, durability tests from the both electrochemical evaluation methods, and impedance spectroscopy, followed by physicochemical characterizations.

## References

1. S. Tombaz, A. Västberg and J. Zander, *Wireless Communications, IEEE*, 2011, **18**, 18-24.
2. B. Dunn, H. Kamath and J.-M. Tarascon, *Science*, 2011, **334**, 928-935.
3. M. Skyllas-Kazacos, M. Chakrabarti, S. Hajimolana, F. Mjalli and M. Saleem, *Journal of the Electrochemical Society*, 2011, **158**, R55-R79.
4. G. L. Soloveichik, *Annual review of chemical and biomolecular engineering*, 2011, **2**, 503-527.
5. M. Armand and J.-M. Tarascon, *Nature*, 2008, **451**, 652-657.
6. A. F. Burke, *Proceedings of the IEEE*, 2007, **95**, 806-820.
7. M. Winter and R. J. Brodd, *Chemical reviews*, 2004, **104**, 4245-4270.
8. F. Cheng and J. Chen, *Chemical Society reviews*, 2012, **41**, 2172-2192.
9. G. Girishkumar, B. McCloskey, A. Luntz, S. Swanson and W. Wilcke, *The Journal of Physical Chemistry Letters*, 2010, **1**, 2193-2203.
10. J.-S. Lee, S. Tai Kim, R. Cao, N.-S. Choi, M. Liu, K. T. Lee and J. Cho, *Advanced Energy Materials*, 2011, **1**, 34-50.
11. M. Broussely, J. Planchat, G. Rigobert, D. Virey and G. Sarre, *Journal of power sources*, 1997, **68**, 8-12.
12. B. Kennedy, D. Patterson and S. Camilleri, *Journal of Power Sources*, 2000, **90**, 156-162.
13. Y. Li and H. Dai, *Chemical Society reviews*, 2014, **43**, 5257-5275.
14. J. Vetter, P. Novák, M. Wagner, C. Veit, K.-C. Möller, J. Besenhard, M. Winter, M. Wohlfahrt-Mehrens, C. Vogler and A. Hammouche, *Journal of power sources*, 2005, **147**, 269-281.
15. L. Ji, Z. Lin, M. Alcoutlabi and X. Zhang, *Energy & Environmental Science*, 2011, **4**, 2682-2699.
16. J. W. Fergus, *Journal of Power Sources*, 2010, **195**, 939-954.

17. M. Wakihara, *Materials Science and Engineering: R: Reports*, 2001, **33**, 109-134.
18. Z.-L. Wang, D. Xu, J.-J. Xu and X.-B. Zhang, *Chemical Society reviews*, 2014, **43**, 7746-7786.
19. K. F. Blurton and A. F. Sammells, *Journal of Power Sources*, 1979, **4**, 263-279.
20. M. Jacoby, *Chemical & Engineering News*, 2010, **88**, 29-31.
21. N. Korovin, in *New Carbon Based Materials for Electrochemical Energy Storage Systems: Batteries, Supercapacitors and Fuel Cells*, Springer, 2006, pp. 137-149.
22. Y. Shimizu, H. Matsuda, N. Miura and N. Yamazoe, *Chemistry Letters*, 1992, 1033-1036.
23. D. Linden and T. B. Reddy, McGraw Hill, 2001.
24. X. Wang, P. Sebastian, M. A. Smit, H. Yang and S. Gamboa, *Journal of power sources*, 2003, **124**, 278-284.
25. A. Mohamad, *Journal of power sources*, 2006, **159**, 752-757.
26. R. Padbury and X. Zhang, *Journal of Power Sources*, 2011, **196**, 4436-4444.
27. T. Ogasawara, A. Débart, M. Holzapfel, P. Novák and P. G. Bruce, *Journal of the American Chemical Society*, 2006, **128**, 1390-1393.
28. I. Hadjipaschalis, A. Poullikkas and V. Efthimiou, *Renewable and sustainable energy reviews*, 2009, **13**, 1513-1522.
29. F. R. McLarnon and E. J. Cairns, *Journal of the Electrochemical Society*, 1991, **138**, 645-656.
30. W. Li, C. Li, C. Zhou, H. Ma and J. Chen, *Angewandte Chemie*, 2006, **118**, 6155-6158.
31. L. Jörissen, *Journal of Power Sources*, 2006, **155**, 23-32.
32. S. Narayanan, G. S. Prakash, A. Manohar, B. Yang, S. Malkhandi and A. Kindler, *Solid State Ionics*, 2012, **216**, 105-109.
33. D. Egan, C. P. De León, R. Wood, R. Jones, K. Stokes and F. Walsh, *Journal of Power Sources*, 2013, **236**, 293-310.
34. T. Zhang, Z. Tao and J. Chen, *Materials Horizons*, 2014, **1**, 196-206.

35. P. Hartmann, C. L. Bender, M. Vračar, A. K. Dürr, A. Garsuch, J. Janek and P. Adelhelm, *Nature materials*, 2013, **12**, 228-232.
36. E. Peled, D. Golodnitsky, R. Hadar, H. Mazor, M. Goor and L. Burstein, *Journal of Power Sources*, 2013, **244**, 771-776.
37. X. Ren and Y. Wu, *Journal of the American Chemical Society*, 2013, **135**, 2923-2926.
38. P. G. Bruce, S. A. Freunberger, L. J. Hardwick and J.-M. Tarascon, *Nature materials*, 2012, **11**, 19-29.
39. J. Christensen, P. Albertus, R. S. Sanchez-Carrera, T. Lohmann, B. Kozinsky, R. Liedtke, J. Ahmed and A. Kojic, *Journal of the Electrochemical Society*, 2011, **159**, R1-R30.
40. A. Kraysberg and Y. Ein-Eli, *Journal of Power Sources*, 2011, **196**, 886-893.
41. J. Goldstein, I. Brown and B. Koretz, *Journal of power sources*, 1999, **80**, 171-179.
42. Y. Li, M. Gong, Y. Liang, J. Feng, J. E. Kim, H. Wang, G. Hong, B. Zhang and H. Dai, *Nature communications*, 2013, **4**, 1805.
43. M. Prabu, P. Ramakrishnan, H. Nara, T. Momma, T. Osaka and S. Shanmugam, *ACS applied materials & interfaces*, 2014, **6**, 16545-16555.
44. D. U. Lee, H. W. Park, M. G. Park, V. Ismayilov and Z. Chen, *ACS applied materials & interfaces*, 2014, **7**, 902-910.
45. D. U. Lee, J.-Y. Choi, K. Feng, H. W. Park and Z. Chen, *Advanced Energy Materials*, 2014, **4**.
46. D. H. W. Park, D. U. Lee, M. G. Park, R. Ahmed, D. M. H. Seo, P. L. F. Nazar<sup>2</sup> and P. Z. Chen, *ChemSusChem*, 2015, **8**, 8.
47. H. W. Park, D. U. Lee, P. Zamani, M. H. Seo, L. F. Nazar and Z. Chen, *Nano Energy*, 2014, **10**, 192-200.
48. Z. Chen, A. Yu, D. Higgins, H. Li, H. Wang and Z. Chen, *Nano letters*, 2012, **12**, 1946-1952.

49. J. Masa, W. Xia, I. Sinev, A. Zhao, Z. Sun, S. Grutzke, P. Weide, M. Muhler and W. Schuhmann, *Angewandte Chemie*, 2014, **53**, 8508-8512.
50. H. Kim, G. Jeong, Y.-U. Kim, J.-H. Kim, C.-M. Park and H.-J. Sohn, *Chemical Society reviews*, 2013, **42**, 9011-9034.
51. C.-C. Yang and S.-J. Lin, *Journal of power sources*, 2002, **112**, 174-183.
52. X. G. Zhang, *Journal of power sources*, 2006, **163**, 591-597.
53. X. G. Zhang, Google Patents, 2007.
54. N. C. Tang, Google Patents, 2001.
55. L. F. Urry, Google Patents, 2000.
56. L. Vorkapić, D. Dražić and A. Despić, *Journal of the Electrochemical Society*, 1974, **121**, 1385-1392.
57. L. Baugh, F. Tye and N. White, *Journal of Applied Electrochemistry*, 1983, **13**, 623-635.
58. D. Bhatt and R. Udhayan, *Journal of power sources*, 1994, **47**, 177-184.
59. A. S. Kannan, S. Muralidharan, K. Sarangapani, V. Balaramachandran and V. Kapali, *Journal of power sources*, 1995, **57**, 93-98.
60. C. W. Lee, K. Sathiyarayanan, S. W. Eom and M. S. Yun, *Journal of power sources*, 2006, **160**, 1436-1441.
61. C. Zhang, J. Wang, L. Zhang, J. Zhang and C. Cao, *Journal of applied electrochemistry*, 2001, **31**, 1049-1054.
62. X. Zhu, H. Yang, X. Ai, J. Yu and Y. Cao, *Journal of applied electrochemistry*, 2003, **33**, 607-612.
63. C.-C. Yang, W.-C. Chien, P.-W. Chen and C.-Y. Wu, *Journal of Applied Electrochemistry*, 2009, **39**, 39-44.
64. Y.-D. Cho and G. T.-K. Fey, *Journal of Power Sources*, 2008, **184**, 610-616.
65. S.-M. Lee, Y.-J. Kim, S.-W. Eom, N.-S. Choi, K.-W. Kim and S.-B. Cho, *Journal of Power Sources*, 2013, **227**, 177-184.

66. D. M. See and R. E. White, *Journal of Chemical & Engineering Data*, 1997, **42**, 1266-1268.
67. R. Othman, W. J. Basirun, A. H. Yahaya and A. Arof, *Journal of power sources*, 2001, **103**, 34-41.
68. C.-C. Yang and S.-J. Lin, *Journal of Power Sources*, 2002, **112**, 497-503.
69. X. Zhu, H. Yang, Y. Cao and X. Ai, *Electrochimica acta*, 2004, **49**, 2533-2539.
70. P. Arora and Z. Zhang, *Chemical reviews*, 2004, **104**, 4419-4462.
71. P. Kritzer and J. A. Cook, *Journal of The Electrochemical Society*, 2007, **154**, A481-A494.
72. G. Wu, S. Lin, J. You and C. Yang, *Materials Chemistry and Physics*, 2008, **112**, 798-804.
73. G. Wu, S. Lin and C. Yang, *Journal of membrane science*, 2006, **284**, 120-127.
74. E. L. Dewi, K. Oyaizu, H. Nishide and E. Tsuchida, *Journal of power sources*, 2003, **115**, 149-152.
75. Y.-J. Wang, J. Qiao, R. Baker and J. Zhang, *Chemical Society reviews*, 2013, **42**, 5768-5787.
76. Y. Zhao, S. Chen, B. Sun, D. Su, X. Huang, H. Liu, Y. Yan, K. Sun and G. Wang, *Scientific reports*, 2015, **5**, 7629.
77. R. Cao, J.-S. Lee, M. Liu and J. Cho, *Advanced Energy Materials*, 2012, **2**, 816-829.
78. J. Wang, H. Wu, D. Gao, S. Miao, G. Wang and X. Bao, *Nano Energy*, 2015, **13**, 10.
79. H. W. Park, D. U. Lee, Y. Liu, J. Wu, L. F. Nazar and Z. Chen, *Journal of the Electrochemical Society*, 2013, **160**, A2244-A2250.
80. J. S. Spendelow and A. Wieckowski, *Physical Chemistry Chemical Physics*, 2007, **9**, 2654-2675.
81. J. Greeley, I. Stephens, A. Bondarenko, T. P. Johansson, H. A. Hansen, T. Jaramillo, J. Rossmeisl, I. Chorkendorff and J. K. Nørskov, *Nature chemistry*, 2009, **1**, 552-556.
82. B. Cui, H. Lin, J. B. Li, X. Li, J. Yang and J. Tao, *Advanced Functional Materials*, 2008, **18**, 1440-1447.

83. Y. Li, P. Hasin and Y. Wu, *Advanced materials*, 2010, **22**, 1926-1929.
84. F. Cheng, J. Shen, B. Peng, Y. Pan, Z. Tao and J. Chen, *Nature chemistry*, 2011, **3**, 79-84.
85. J. Landon, E. Demeter, N. İnoğlu, C. Keturakis, I. E. Wachs, R. Vasić, A. I. Frenkel and J. R. Kitchin, *Acs Catalysis*, 2012, **2**, 1793-1801.
86. D. U. Lee, B. J. Kim and Z. Chen, *Journal of Materials Chemistry A*, 2013, **1**, 4754.
87. A. J. Esswein, M. J. McMurdo, P. N. Ross, A. T. Bell and T. D. Tilley, *The Journal of Physical Chemistry C*, 2009, **113**, 15068-15072.
88. D. U. Lee, J. Scott, H. W. Park, S. Abureden, J.-Y. Choi and Z. Chen, *Electrochemistry Communications*, 2014, **43**, 109-112.
89. H. Zhang, Y. Shimizu, Y. Teraoka, N. Miura and N. Yamazoe, *Journal of Catalysis*, 1990, **121**, 432-440.
90. H. Tanaka and M. Misono, *Current Opinion in Solid State and Materials Science*, 2001, **5**, 381-387.
91. L. Swette, N. Kackley and S. McCatty, *Journal of power sources*, 1991, **36**, 323-339.
92. A. Kannan, A. Shukla and S. Sathyanarayana, *Journal of Power Sources*, 1989, **25**, 141-150.
93. L. Swette and N. Kackley, *Journal of power sources*, 1990, **29**, 423-436.
94. M. Yuasa, M. Nishida, T. Kida, N. Yamazoe and K. Shimano, *Journal of the Electrochemical Society*, 2011, **158**, A605-A610.
95. X. Ge, Y. Liu, F. T. Goh, T. A. Hor, Y. Zong, P. Xiao, Z. Zhang, S. H. Lim, B. Li and X. Wang, *ACS applied materials & interfaces*, 2014, **6**, 12684-12691.
96. Y. Liang, H. Wang, P. Diao, W. Chang, G. Hong, Y. Li, M. Gong, L. Xie, J. Zhou, J. Wang, T. Z. Regier, F. Wei and H. Dai, *Journal of the American Chemical Society*, 2012, **134**, 15849-15857.
97. Y. Liang, Y. Li, H. Wang, J. Zhou, J. Wang, T. Regier and H. Dai, *Nature materials*, 2011, **10**, 780-786.

98. M. Prabu, P. Ramakrishnan and S. Shanmugam, *Electrochemistry Communications*, 2014, **41**, 59-63.
99. Z. Chen, A. Yu, R. Ahmed, H. Wang, H. Li and Z. Chen, *Electrochimica Acta*, 2012, **69**, 295-300.
100. Y. Liang, Y. Li, H. Wang and H. Dai, *Journal of the American Chemical Society*, 2013, **135**, 2013-2036.
101. D. U. Lee, H. W. Park, M. G. Park, V. Ismayilov and Z. Chen, *ACS applied materials & interfaces*, 2015, **7**, 902-910.
102. C.-F. Chen, G. King, R. M. Dickerson, P. A. Papin, S. Gupta, W. R. Kellogg and G. Wu, *Nano Energy*, 2015, **13**, 10.
103. S. Wang, E. Iyyamperumal, A. Roy, Y. Xue, D. Yu and L. Dai, *Angewandte Chemie International Edition*, 2011, **50**, 11756-11760.
104. S. Wang, L. Zhang, Z. Xia, A. Roy, D. W. Chang, J. B. Baek and L. Dai, *Angewandte Chemie International Edition*, 2012, **51**, 4209-4212.
105. E. Iyyamperumal, S. Wang and L. Dai, *ACS nano*, 2012, **6**, 5259-5265.
106. D. Yu, Y. Xue and L. Dai, *The Journal of Physical Chemistry Letters*, 2012, **3**, 2863-2870.
107. D. Higgins, Z. Chen, D. U. Lee and Z. Chen, *Journal of Materials Chemistry A*, 2013, **1**, 2639.
108. J. Masa, W. Xia, I. Sinev, A. Zhao, Z. Sun, S. Grützke, P. Weide, M. Muhler and W. Schuhmann, *Angewandte Chemie International Edition*, 2014, **53**, 8508-8512.
109. L. Reimer, Springer.
110. L. Reimer and H. Kohl, *Transmission Electron Microscopy: Physics If Image Formation*, Springer, 2008.
111. E. Crain, *Spectrum*, 2000.
112. P. Van der Heide, *X-ray photoelectron spectroscopy: an introduction to principles and practices*, John Wiley & Sons, 2011.

113. V. I. Nefedov, *X-ray photoelectron spectroscopy of solid surfaces*, Springer Science & Business, 1988.
114. S. Brunauer, P. H. Emmett and E. Teller, *Journal of the American Chemical Society*, 1938, **60**, 309-319.
115. E. Gileadi, *Cell*, 2011, **3**, 4.
116. J. B. Allen and R. F. Larry, *Department of Chemistry and Biochemistry University of Texas at Austin, John Wiley & Sons, Inc*, 2001, 156-176.
117. W. Xiao, D. Wang and X. W. Lou, *The Journal of Physical Chemistry C*, 2009, **114**, 1694-1700.
118. D. U. Lee, M. G. Park, H. W. Park, M. H. Seo, X. Wang and Z. Chen, *ChemSusChem*, 2015.
119. C. Jin, F. Lu, X. Cao, Z. Yang and R. Yang, *Journal of Materials Chemistry A*, 2013, **1**, 12170-12177.
120. F. Cheng, J. Liang, Z. Tao and J. Chen, *Advanced materials*, 2011, **23**, 1695-1715.
121. D. Eder, *Chemical Reviews*, 2010, **110**, 1348-1385.
122. X. Wang, J. Zhuang, Q. Peng and Y. Li, *Nature*, 2005, **437**, 121-124.
123. N. Zhao, W. Nie, J. Mao, M. Yang, D. Wang, Y. Lin, Y. Fan, Z. Zhao, H. Wei and X. Ji, *Small*, 2010, **6**, 2558-2565.
124. Z. Chen, Y. Yuan, H. Zhou, X. Wang, Z. Gan, F. Wang and Y. Lu, *Advanced materials*, 2014, **26**, 339-345.
125. M. Glerup, M. Castignolles, M. Holzinger, G. Hug, A. Loiseau and P. Bernier, *Chemical Communications*, 2003, 2.
126. J. H. Lin, C. S. Chen, Z. Y. Zeng, C. W. Chang and H. W. Chen, *Nanoscale*, 2012, **4**, 4757-4764.
127. C. Xiong, Z. Wei, B. Hu, S. Chen, L. Li, L. Guo, W. Ding, X. Liu, W. Ji and X. Wang, *Journal of Power Sources*, 2012, **215**, 216-220.
128. P. Ayala, R. Arenal, M. Rummeli, A. Rubio and T. Pichler, *Carbon*, 2010, **48**, 575-586.

129. Y. Liu, D. C. Higgins, J. Wu, M. Fowler and Z. Chen, *Electrochemistry Communications*, 2013, **34**, 125-129.
130. L. Lai, J. R. Potts, D. Zhan, L. Wang, C. K. Poh, C. Tang, H. Gong, Z. Shen, J. Lin and R. S. Ruoff, *Energy & Environmental Science*, 2012, **5**, 7936.
131. H. Kim, K. Lee, S. I. Woo and Y. Jung, *Physical chemistry chemical physics : PCCP*, 2011, **13**, 17505-17510.
132. T. Sharifi, G. Hu, X. Jia and T. Wagberg, *ACS NANO*, 2012, **6**, 8904-8912.
133. M. Hamdani, R. N. Singh and P. Chartier, *International Journal of Electrochemical science*, 2010, **5**, 556-577.
134. D. R. Lawson, L. D. Whiteley, C. R. Martin, M. N. Szentirmay and J. I. Song, *Journal of the Electrochemical Society*, 1988, **135**, 7.
135. S. K. Zecevic, J. S. Wainright, M. H. Litt, S. L. Gojkovic and R. F. Savinell, *Journal of the Electrochemical Society*, 1997, **144**, 10.
136. W. Yuan, Y. Zhou, Y. Li, C. Li, H. Peng, J. Zhang, Z. Liu, L. Dai and G. Shi, *Scientific reports*, 2013, **3**.
137. A. K. Geim, *Science*, 2009, **324**, 5.
138. H. Dai, *Acc. Chem. Res.*, 2002, **35**, 10.